The Thesis Committee for Izaak Ruiz
Certifies that this is the approved version of the following Thesis:

Characterization of the High Island 24L Field for Modeling and Estimating CO_2 Storage Capacity in the Offshore Texas State Waters, Gulf of Mexico

APPROVED BY
SUPERVISING COMMITTEE:

_____
Timothy A. Meckel, Supervisor

_____
William L. Fisher

_____
Mariana I. Olariu

Characterization of the High Island Field 24L Field for Modeling and Estimating CO_2 Storage Capacity in the Offshore Texas State Waters, Gulf of Mexico

by

Izaak Ruiz

Thesis

Presented to the Faculty of the Graduate School of

The University of Texas at Austin

in Partial Fulfillment

of the Requirements

for the Degree of

Master of Science in Geological Sciences

The University of Texas at Austin

August 2019

Dedication

This thesis is dedicated to my parents, Federico Ruiz III and Josefina Ruiz, for all their love and support. Also to those underprivileged kids who have dreams of becoming someone BIG one day, never give up.

Acknowledgements

To start, I would first like to thank God for blessing me with this incredible journey. I then want to say thank you to my adviser, Tip Meckel, for trusting and believing in me from the moment I started as a graduate student. His mentorship has greatly inspired me to always think outside the box and execute geologically sound results. Without a doubt he is the reason why you are seeing this document. To my committee members, thank you for your selfless guidance and input. Thank you to Iulia for sharing your knowledge in well-log correlations that has tremendously helped my research and for your great mentorship. Thank you for supervising me from when I first started working as an Undergraduate Research Assistant to now graduating with my Master's. To Bill Fisher, the legend, thank you for instructing my favorite graduate-level courses. Your expertise and experience in academia and the industry are something I truly admire. But most importantly, thank you for your assistance in starting the GeoFORCE program.

To the Gulf Coast Carbon Center (GCCC), thank you all for making the research environment very friendly and comfortable and for having me as a Graduate Research Assistant. Thank you, Ramon Treviño, for your advice and help with any problem I had and for first bringing me in as an Undergraduate Research Assistant to be part of the GCCC. Thank you, Michael DeAngelo, for our talks about careers and life. Thank you, Sue Hovorka, for your encouragement throughout these two years. Thank you, Seyyed Hosseini, for showing me how to use EASiTool. Thank you, Dallas Dunlap, Chuck Garza, and Joseph Yeh, for all your technical support.

Thank you to the Jackson School of Geosciences and the Bureau of Economic Geology for providing me with the foundation that I use take throughout my career. To all the professors and researchers I had a chance to interact with, thank you all for sharing your knowledge and being very personable. Specifically, Peter Flemings, thank you for introducing me to seismic in your Energy Exploration class as an undergrad and for all your career advice. You pushed me to pursue graduate school, and without your help, I would not be receiving this degree.

Many thanks to the GeoFORCE program and its sponsors for providing me with a scholarship during my undergraduate years and a fellowship for my Master's. This program is the sole reason that I first started pursuing an education at a public university. Thank you to Eleanor Snow and Dana Thomas for your love and support all these years. Many thanks to all the staff of GeoFORCE (John, Edgar, Lindsay, Sam) for impacting the lives of many students with this program, just like you did with me. To all the new staff, I hope you continue to make a difference in the students' lives by showing them that education is very important and it is not impossible.

Thank you to all my friends during my years of studying geology. Many thanks to Reynaldy Fifariz for his mentorship, friendship, and patience during my two years as a graduate student. Thank you Emily, Pooneh, Ye, and Omar for sharing ideas and being there for whenever we needed anything. Thank you to all my friends for encouraging me and allowing myself to not always think about my thesis.

Also, thank you to Woody Pace for giving me the opportunity to intern with Repsol. This has been by far my favorite experience working in the industry in which I hope to have a long career. Thank you for making sure I felt comfortable at all times and for your inspiration to become someone BIG in this world. You are a true role model.

Last but most importantly, thank you to my parents and siblings. Your encouragement throughout these years has enabled me to never give up. Mom and Dad, your desire to want the best for me has been so incredible that I cannot say thank you enough. Susel and Fred, thank you for leading the way in pursuing excellence and teaching me right from wrong. Thank you again for all your unconditional love. I hope I continue to make each of you proud in wherever life takes me. I love you guys so much.

Abstract

Characterization of the High Island 24L Field for Modeling and Estimating CO_2 Storage Capacity in the Offshore Texas State Waters, Gulf of Mexico

Izaak Ruiz, M.S. Geo. Sci.

The University of Texas at Austin, 2019

Supervisor: Timothy A. Meckel

Carbon, Capture, and Storage (CCS) is considered an essential technology that can contribute to reaching the IPCC's target to limit global average temperature rise to no more than 2.0°C. The fundamental purpose of CCS is to reduce anthropogenic CO_2 emissions by capturing gas from large point sources and injecting it into deep geologic formations. In the offshore Texas State Waters (10.3 miles; 16.6 kilometers), the potential to develop CO_2 storage projects is viable, but the size of storage opportunity at the project level is poorly constrained. This research characterizes the High Island 24L Field, a relatively large historic hydrocarbon field, that has produced mainly natural gas (0.5 Tcf). The primary motivation for this study is to demonstrate that depleted gas fields can serve as volumetrically significant CO_2 storage sites.

The stratigraphy of the inner continental shelf in the Gulf of Mexico has been extensively explored for hydrocarbon for over 50 years, and this area is well suited for CCS. Lower Miocene sandstones beneath the regional transgressive *Amphistegina* B shale

have appropriate geologic properties (porosity, thickness, extent) and can be characterized utilizing 3D seismic and well logs in this study. Identifying key stratigraphic surfaces, faults, and mapping structural closure footprints illustrates the field's geologic structure. The interpreted stratigraphic framework can then be used to model three different lithologic facies and effective porosity to calculate CO_2 storage capacity for both the ~200-ft (60-m) thick HC Sand (most productive gas reservoir) and the overlying thicker 1700 ft (520 m), but non-productive, Storage Interval of Interest.

Four different methodologies are utilized to achieve confidence in the CO_2 storage capacity estimates. A storage capacity of 15 – 23 MT is calculated for the HC Sand and 108 – 179 MT for the Storage Interval of Interest by applying interpreted efficiency factors. This study evaluates the accuracy of these storage capacity methodologies to better understand the key geologic factors that influence CO_2 storage in a depleted hydrocarbon field for CCS.

Table of Contents

List of Tables

List of Figures

Chapter 1: Introduction

1.1: Carbon Capture and Storage Background

Carbon capture and storage (CCS) is the process of capturing, transporting, and storing carbon dioxide (CO_2) in large quantities for the sole purpose of not releasing it into the atmosphere and thus ultimately reducing greenhouse gas emissions (Figure 1.1). CCS is considered to be one of the primary methods needed for reaching the 2.0°C target that the Intergovernmental Panel on Climate Change (IPCC) set in 2018 (Global CCS Institute Report, 2018). The general acceptance that necessary actions have to take place concurrently to mitigate anthropogenic CO_2 emissions is playing a key role in the research and implementation of CCS (Bachu, 2003).

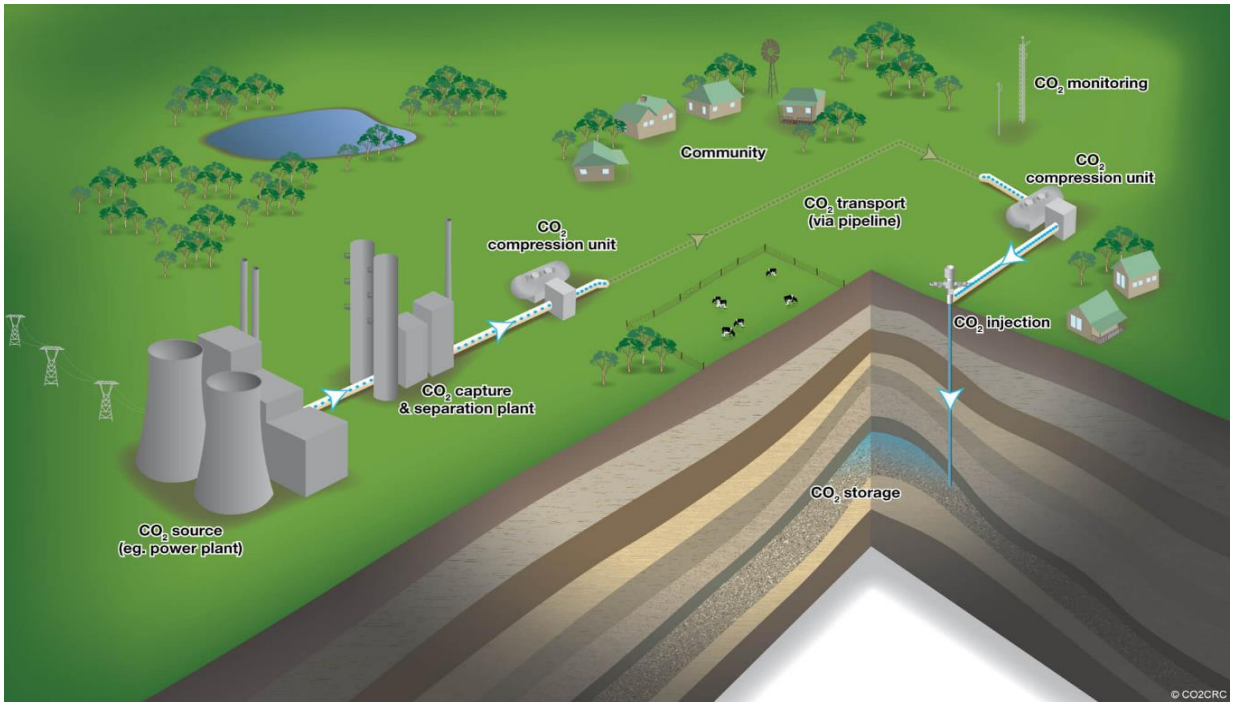

Figure 1.1: What is Carbon Capture and Storage? CO_2 is first captured from a point source (e.g., power plant) and then transported via a pipeline (in most cases) and finally injected into a deep geologic reservoir for storage (CO_2CRC).

Many large-scale storage projects have demonstrated the successful subsurface injection and permanent storage of CO_2 in geologic media (carbon sequestration/geologic storage), such as Sleipner and Snøhvit in Norway and In Salah in Algeria (CCS Facilities Database). In order to achieve high subsurface storage efficiency, CO_2 is commonly injected in its supercritical state. The conditions for achieving supercritical state include (Bachu, 2000): depths greater than about 2600 ft (800 m), pressures exceeding 1000 psi (7.4 Mpa), and temperatures exceeding 88°F (32°C). This supercritical state of CO_2 allows it to behave like a fluid and a gas at the same time with properties such as low density and viscosity, water solubility, and high mobility. A primary benefit of injecting it in supercritical state is that the dense liquid CO_2 occupies less pore volume than if it were in a gas phase, allowing more CO_2 to be stored per unit of subsurface pore volume.

Three main reservoir types serve as best candidates for carbon storage: depleted oil and gas fields, saline aquifers, and unminable coal seams (Benson and Cole, 2008). This study focuses on depleted hydrocarbon fields as analogues while applying the saline aquifer capacity methodology (Goodman et al., 2011). The study does not address the effects of residual oil and/or gas in CO_2 storage. Depleted oil and gas fields are attractive for carbon storage because of the amount of existing data, infrastructure, and experience (Li et al., 2006). Important geologic parameters for reservoirs include high porosity and permeability, which allows the fluid to migrate with ease and fill the pore space, but also a tight overlying seal that prevents the CO_2 from migrating vertically (leaking). There are many depleted hydrocarbon fields in the offshore Texas State Waters (TSW) that may be suitable for storage. There are many more ‘dry’ (non-productive) structures with similar geologic settings that are also attractive for storage.

However with any project in any industry, risk has to be accounted for. Depleted hydrocarbon fields such as the one in this study have many wells that were previously

drilled decades ago that can present risk if they have not been properly plugged or abandoned. Another major concern are faults or fracture zones that are not sealing during the injection process, as pressure is added to the system. Thus, it is important to understand what the natural gas systems (natural gas accumulations) can tell us about leakage (Lewicki et al., 2007). The goal of research is to mitigate these risks and learn as much as possible from the ongoing projects.

In the end, CCS is a technology that can greatly reduce industrial emissions and can complement expansion of renewables by providing emission-free back up and redundancy. With political confidence and the implementation of carbon taxes and credits, CCS can significantly affect the current emissions trajectory.

1.2: GEOLOGIC SETTING

The Gulf of Mexico (GOM) is a well-documented and researched Late Mesozoic and Cenozoic passive margin basin (Deussen and Owen, 1939; Fisher, 1964; Galloway, 1989b). Rifting of Pangea began during the Late Triassic and the Early Jurassic as the extensive landmass was broken by tensional grabens while being filled with volcanics and red beds. After the formation of the Louann Salt of Late Jurassic age due to alternating periods of flooding and evaporation, the Yucatan platform reached its present position during the Late Jurassic and the GOM was created (Salvador, 1987). The subsequent interaction of sediment supply, tectonic events, and eustasy controlled the general evolutionary history of the GOM's shelf margin (Morton and Galloway, 1991). During the Cretaceous, clastic sediment supply rates were fairly low partly because of high global sea levels, creating a sediment-starved basin. Then in the late Paleocene, large volumes of terrigenous clastic sediment were being supplied to the GOM from fluvial systems established across continental North America (Figure 1.2), prograding the shelf margin

tens of kilometers basinward (Galloway et al., 2011). As this basin margin expansion pattern continued throughout the Cenozoic, it provided a well-preserved sedimentary rock record that helped characterize the present-day GOM.

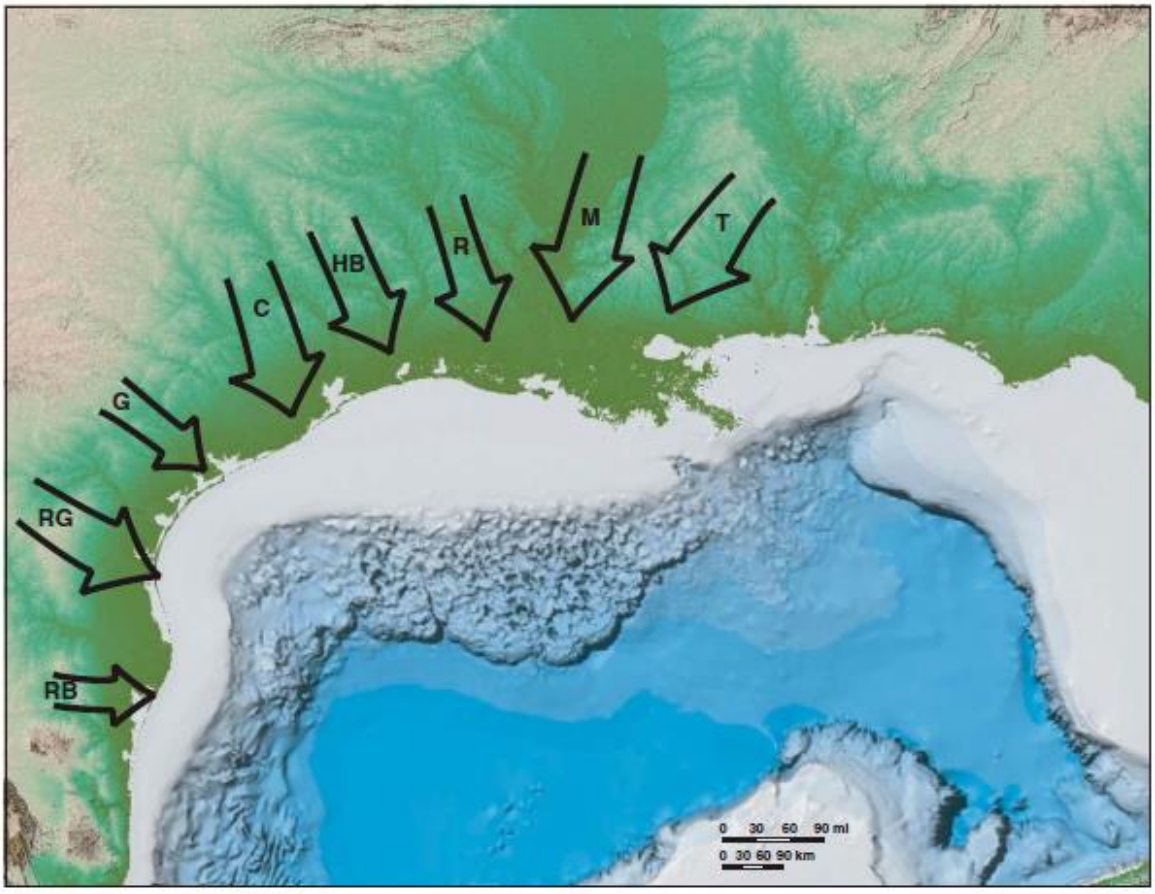

Figure 1.2: Map of the Cenozoic fluvial axes in the Gulf of Mexico. Topographic basemap is for the present day. T=Tennessee; M=Mississippi; R=Red; HB=Houston-Brazos; C=Colorado; G=Guadalupe; RG=Rio Grande; RB=Rio Bravo (from Galloway et al., 2011).

Progradation of thick clastic wedges of sediment from the Oligocene to the Miocene became the main reservoir systems for regional hydrocarbon production in the TSW. The generalized Cenozoic succession is shown in Figure 1.3, illustrating a prograding shelf edge with associated basin flooding events as the shelf edge retrogrades. This study focuses on Miocene stratigraphy due to the thickness, documented marine regressions and transgressions, vast production of hydrocarbons (Rainwater, 1964), and suitable depths for CO_2 storage in a supercritical state.

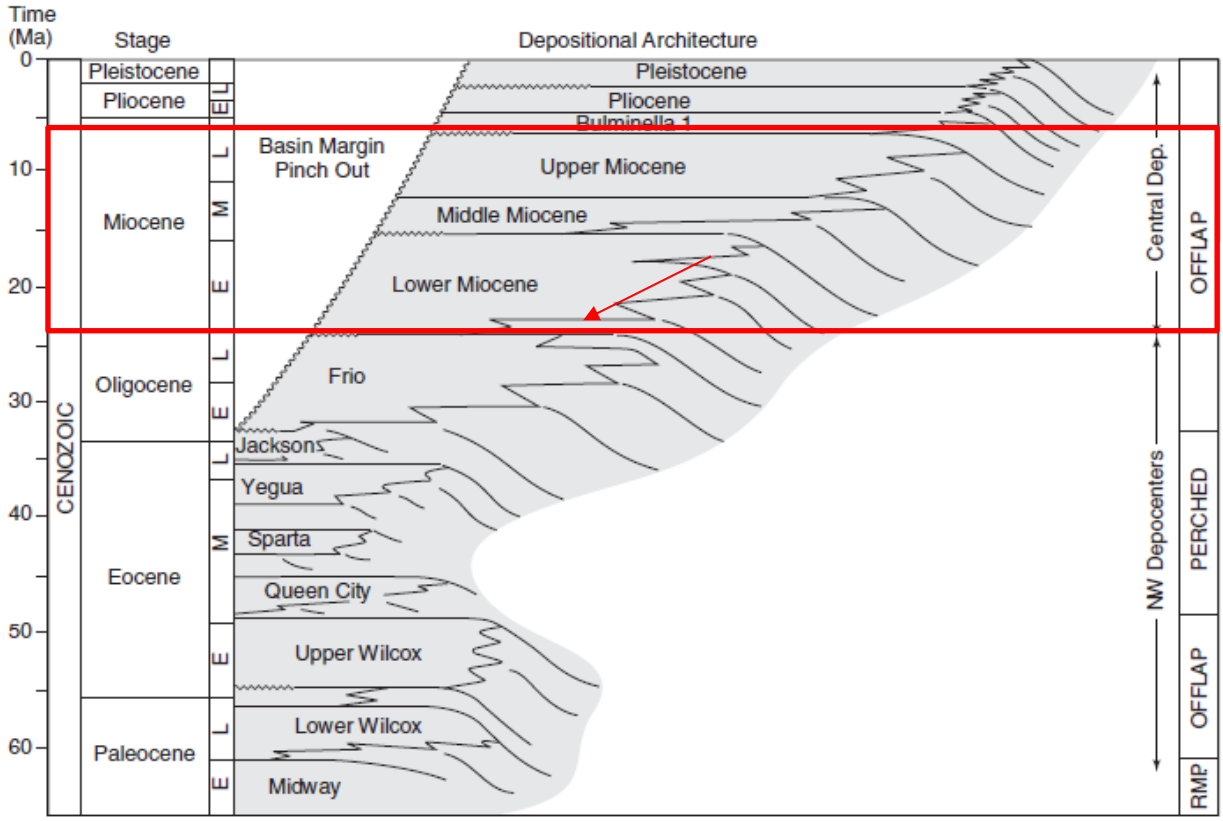

Figure 1.3: Cenozoic stratigraphic succession in the Northern Gulf of Mexico. The red outline highlights the stratigraphy for this study. Note the prograding periods with significant transgressions (e.g., Anahuac Shale represented by red arrow) separating them (modified from Galloway, 2008).

The Miocene basin fill has been characterized and correlated with maximum flooding surfaces, an approach that Galloway (1989a, 1989b) established and utilized. Galloway separated the Miocene strata into four depositional episodes (depisodes): Lower Miocene 1 (LM1), Lower Miocene 2 (LM2), Middle Miocene (MM), and Upper Miocene (UM) (Figure 1.4). The 8 m.y. early Miocene deposits (Fleming Group) follow a regional transgression that deposited the Anahuac Shale and are characterized by two (LM1 and LM2), thick, prograding, clastic packages that are separated by a prominent transgressive marine shale tongue containing the *Marginulina ascensionensis* (*Marg.* A) fauna (Galloway et al., 2000). Initially, early Miocene progradation created the LM1 depisode (Oakville Formation) and built onto the submerged shelf platform that was constructed during the earlier Frio depisode as large-scale growth faulting shaped the paleocontinental margin. The stratigraphy of the LM2 depisode (Lagarto Formation) is characterized by aggradational to retrogradational deposition due to a stable to retreating shoreline. The entire Lower Miocene is then capped by another extensive transgressive shale that contains the *Amphistegina* B (*Amph* B*)* fauna (Galloway, 1989). The 4 Ma middle Miocene depisode (MM) records a brief period of prograding deposition as it is capped by another regional transgressive shale layer marked by the *Textularia stapperi* or *Text* W fauna. The 6 Ma upper Miocene deposits (UM) follow this flooding event with thick shelf-margin delta and slope apron successions prograding the shelf edge. This depisode is then capped by another flooding event that contains the *Robulus* E/*Bigenerina* A biostratigraphic marker, marking the end of the Miocene (Galloway et al., 2000). Flooding events deposited highly potential, tight, top seals as the regressive periods reflect the relative amount of good-quality sands being deposited into the GOM. With these two ideas in mind, the approach of narrowing down a zone for CO_2 storage becomes simpler.

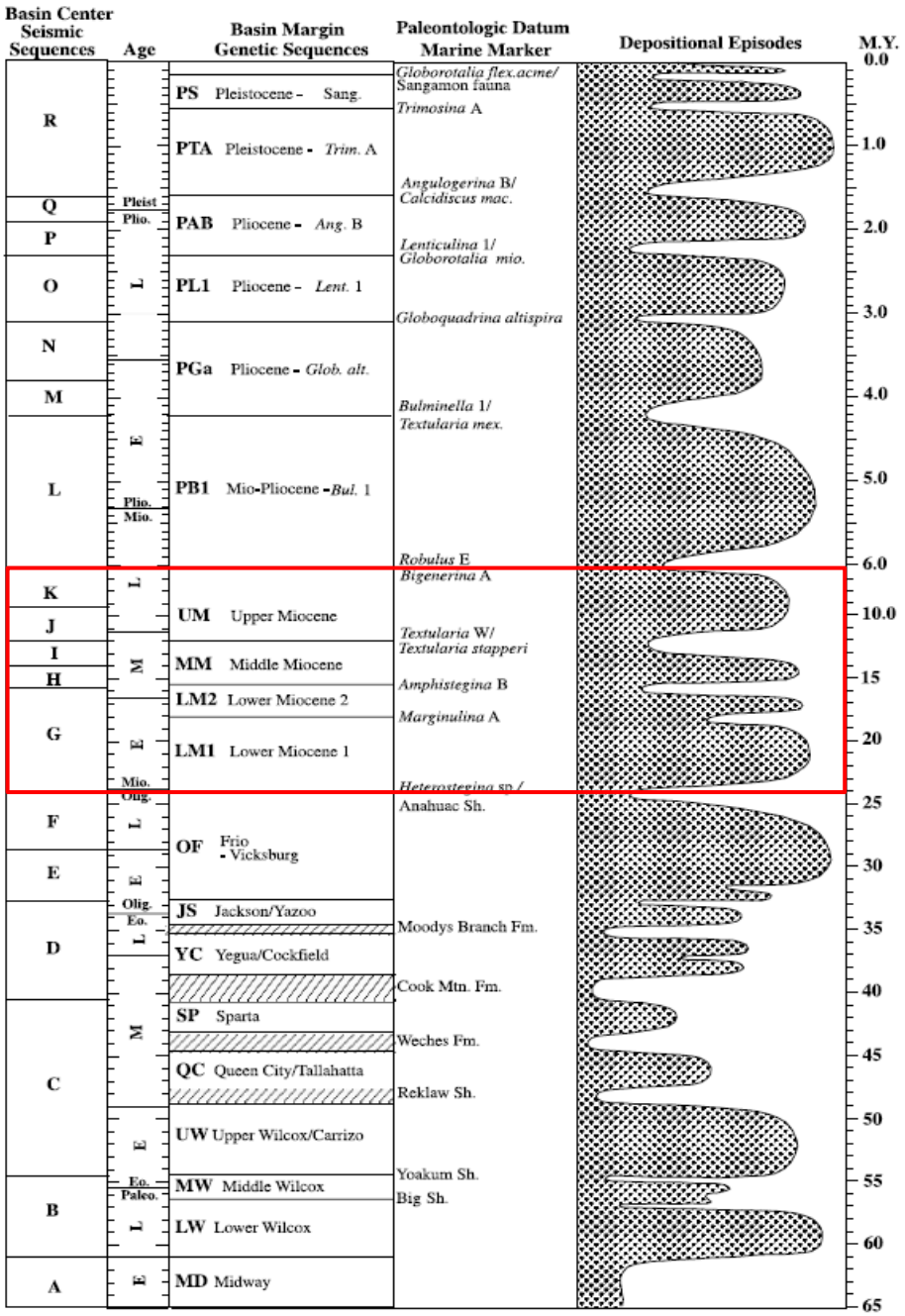

Figure 1.4: Gulf of Mexico Cenozoic genetic sequences and depositional episodes (modified from Galloway et al., 2000). The red outline represents Miocene strata. See text for detailed descriptions.

For this study, the LM1 and LM2 depisodes are the zones of interest because of their thick, successive unit of mostly mixed deltaic and marine shelf blanket sand bodies and the overlying *Amph* B shale. During the early Miocene, fluvial systems draining northwest continental North America supplied significant amounts of terrigenous sediment into the northern GOM via the Red and Mississippi Rivers (Figure 1.5). The sedimentation rate increases during the LM2 depisode at a rate that had not been recorded since the Late Eocene (Figure 1.6). This combined knowledge of understanding the geologic context in the TSW illustrates how these depositional systems have great potential not only for natural hydrocarbon accumulations but also for engineered carbon storage.

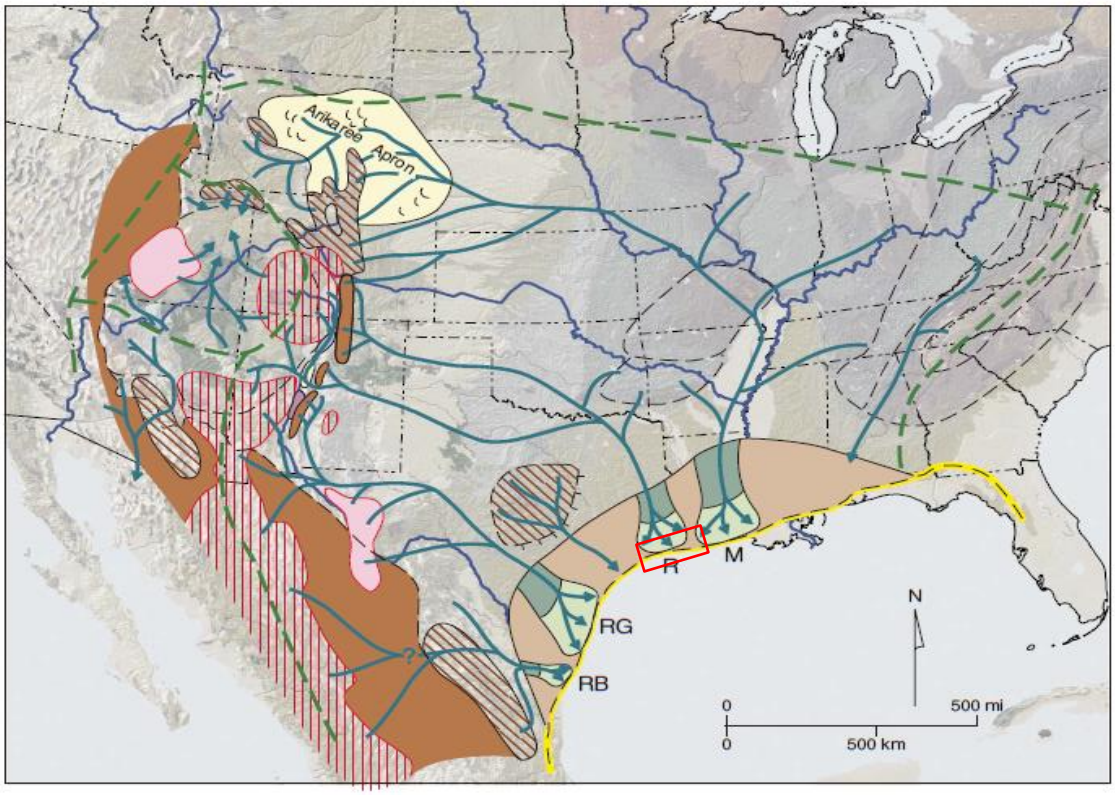

Paleogeographic Map Explanation

Drainage Basin Elements

- Mountain glaciers
- Relict or moderate relief upland
- High-relief upland
- Subsiding alluvial basin
- Bypass alluvial basin
- Lacustrine basin
- Eolian basin fill or aggradational erg
- Aggradational fluvial fan/apron
- Drainage divide
- Fluvial channel systems
- Bedrock canyons

Igneous Features and Provinces

- Active volcanic center
- Caldera complex
- Relict volcanic complex
- Airborne volcanic ash

Receiving Basin Elements

- Depositional coastal plain
- Fluvial axes
- Deltaic depocenters
- Max. progradational shoreline

Figure 1.5: Paleogeographic map of the Early Miocene (~16-23 Ma). The red polygon represents the study area. Note the deltaic depocenters along the Texas-Louisiana Gulf coast, specifically the Red River (modified from Galloway et al., 2011).

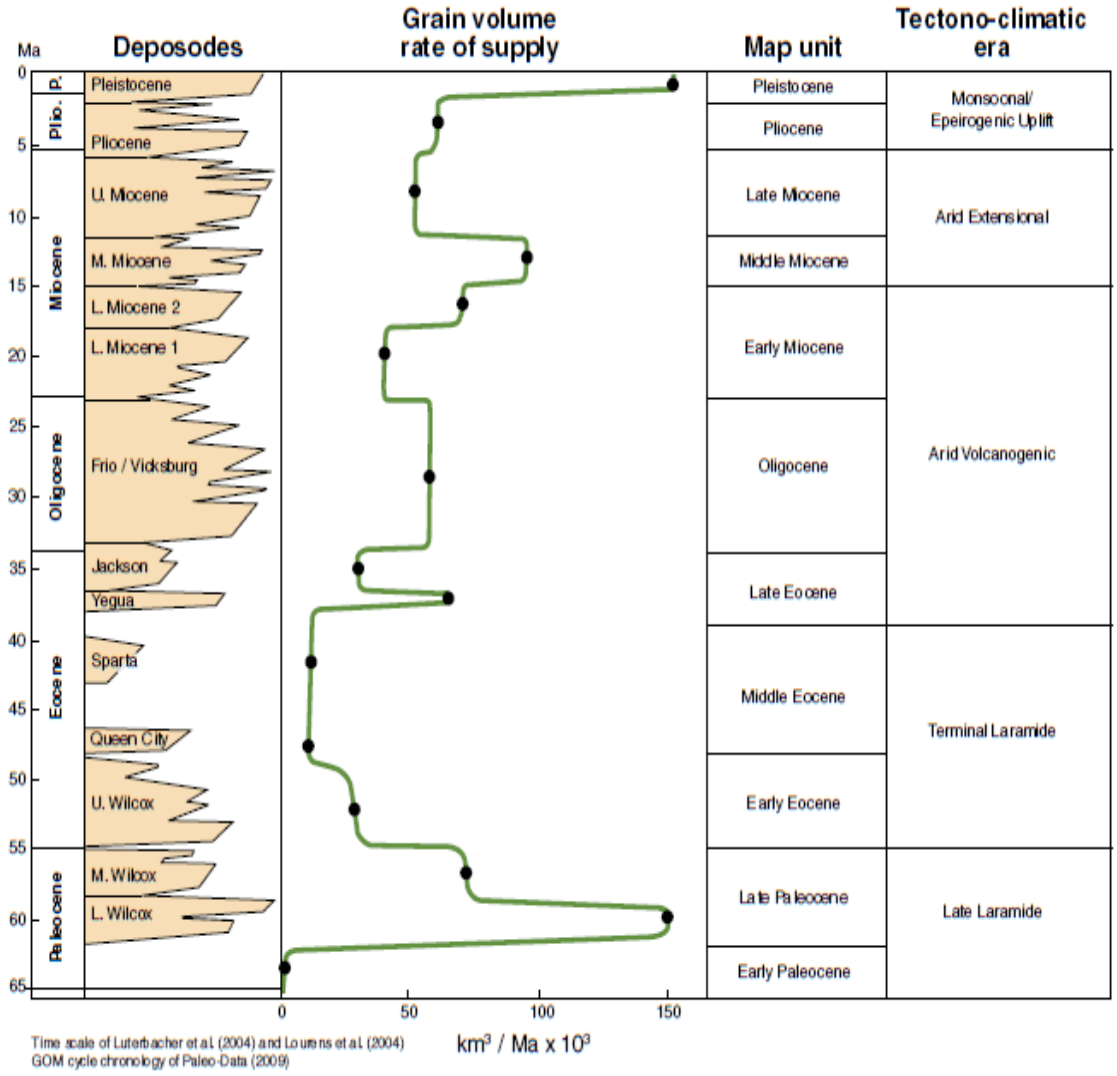

Figure 1.6: Sediment (grain volume) supply rate of Cenozoic depisodes. Note the relatively high sedimentation rate in the LM2 depisode (deposode is the same as depisode) (from Galloway et al., 2011).

1.3: HIGH ISLAND 24L PRODUCTION HISTORY

The High Island 24-L (HI 24L) Field was first discovered in 1967 by Atlantic Richfield Company (ARCO), and by 1986 the field had produced 320 billion cubic feet (Bcf) of gas and 3 million barrels (MMbbl) of oil from 30 Lower Miocene sands (Bulling and Olsen, 1990). The field was first reported to be a significant gas field by Kiatta (1971), noting the basal Miocene interval contained several prospective sands. Three main hydrocarbon plays have been documented below the *Amph* B shale: LM2 P.1B (Middle Lower Miocene), LM4 P.4 (Upper Lower Miocene), and MM4 R.1. (Lower Middle Miocene) (Seni et al., 1997). The LM2 P.1B and the LM4 P.4 reservoirs have a progradational stacking pattern and the MM4 R.1 a retrogradational one (Figure 1.7). This vertical succession illustrates the expected typical log signature of deltaic lobes prograding out into the GOM and retrograding landward, signifying different flooding events. Several characteristics of each of the three plays are outlined in Table 1.1, but the most significant observation is that the porosities of these reservoirs are in the 30% range and the main trap style is anticlinal fault traps. There was also a reported permeability of 50-2500 millidarcys (MD) (Fowler et al., 1987) and 483 MD (Seni et al., 1997) for the HC Sand.

The TSW are divided into three main districts, according to the Railroad Commission (RRC) of Texas, which regulates the exploration, production, and transportation of all oil and natural gas in Texas (Figure 1.8). Utilizing the January 2019 reports that the RRC generates, today the HI 24L Field has produced about 11% of total state water gas and 10% of total state water oil, making it one of the largest gas fields in the TSW. This equates to about 470 Bcf of natural gas and 4.5 MMbbl of oil. The most significant single reservoir in the HI 24L Field, the Miocene age “HC Sand” reservoir at approximately 8500 ft (2590 m), produced about 45% of the total natural gas in the field (Table 1.2). The field still produces from the LJ sand, with about 2 Bcf of cumulative

natural gas in 2018 and 100 MMcf in the most recently reported month (January 2019) (RRC, 2019). Although there is only one well producing in the field, the field is still assumed to be depleted. With all of this background information, a main focal point of this study was to look at the HC Sand in the LM2 P.1B play to understand how it compares to a much thicker interval (SIOI) that has no hydrocarbon production.

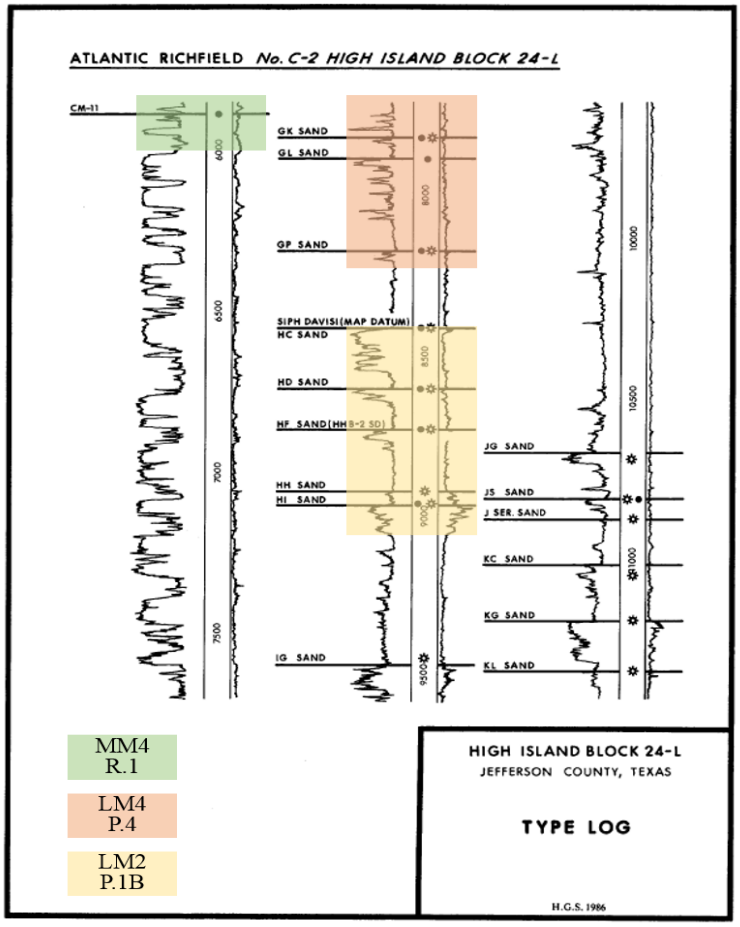

Figure 1.7: Type log with three identified plays. The three different plays (Seni et al., 1997) are outlined in their respective colors. Depth is in feet (modified from Fowler et al., 1987).

Play	Age	Play Name	Year Disc.	Reservoir Depth (ft)	Area (acres)	HC Type	Pay (ft)	Trap	Porosity (%)	Water Sat (%)	Cum Oil (Mbbl)	Cum Gas (MMcf)	Notes
MM4 R.1.	Lower Middle Miocene	Retrogradational Deltaic Sandstone	1969	5743	125	Oil	3	rollover anticline, growth fault	33	58	397	85	Upward fining delta lobe, right below *Amph* B
LM4 P.4.	Upper Lower Miocene	Progradational Deltaic (*Discorbis* B) Sandstone	1969	7962	2299	Oil, Gas	18	rollover anticline, growth fault	31	42	1490	13958	Upward coarsening thin delta lobes, variable reservoir quality
LM 2 P.1B	Middle Lower Miocene	Eastern Progradational Delatic Sandstone	1969	9045	7020	Oil, Gas	26	rollover anticline, growth fault	32	19	2497	301196	Upward coarsening thin delta

Table 1.1: Miocene play characteristics beneath *Amph* B Shale (Seni et al., 1997).

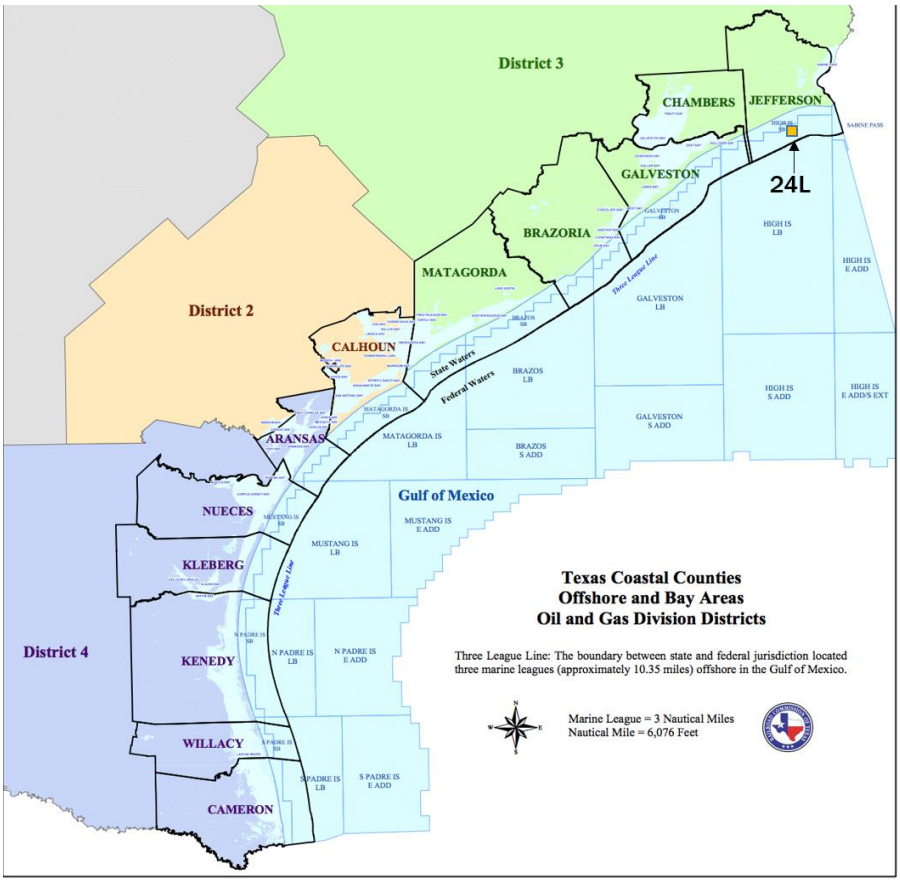

Figure 1.8: Map of Texas coast depicting the different districts according to the Railroad Commission of Texas. Location of the HI 24L Field is shown in orange (modified from RRC).

	Cum Gas Production (Bcf)	Cum Oil Production (Mbbl)
Offshore TX State Waters	4207	42538
District 3	3017	25318
HI 24L	469	4360
HC Sand	206	1222

Table 1.2: Cumulative natural gas and oil production from offshore Texas State Waters; RRC District 3; the HI 24L Field; and the field's HC Sand reservoir.

1.4: PREVIOUS WORK

One of the missions of the Gulf Coast Carbon Center (GCCC) at the Bureau of Economic Geology (BEG) is to perform CO_2 sequestration studies focusing on the Gulf Coast. Many studies have been conducted throughout the years, and several of the relevant ones involve regional CO_2 capacity estimations and interpretation of Miocene strata in the TSW (Treviño and Meckel, 2017). The estimated CO_2 net regional capacity of the Miocene interval in TSW is approximately 129 gigatonnes (Gt) (Wallace et al., 2014). The methodology used adequately constrains to a first order, the maximum CO_2 capacity, but it does not consider the detailed geologic structures of the system. On a smaller scale of CO_2 estimations, Carr et al. (2016) determined the Houston sector, including the HI 24L Field, as "very favorable" for CO_2 sequestration because its capacity is about 8 Gt with about 99 megatonnes (Mt) of CO_2 emissions in 2014 from 131 different point source. These two studies are reasonable estimates for assessing how the Texas Gulf coast can provide significant storage resources.

This study takes the first step in trying to determine if local assessments will prove large regional static capacity estimates or constrain them much further. The schematic cross section in Figure 1.9 represents the general geology in the TSW (Wallace et al., 2014). With this fundamental offlapping progradational geology in mind, regional seismic interpretations (DeAngelo et al., 2019) and well log correlations (Olariu et al., in review) can be used to screen and rank potential CCS prospects, highlighting the HI 24L and HI 10L (Ramirez Garcia, 2019) Fields. Both studies quantify how much capacity there may be at the project scale and overall describe a workflow in characterizing and modeling depleted hydrocarbon fields for the sole purpose of carbon storage.

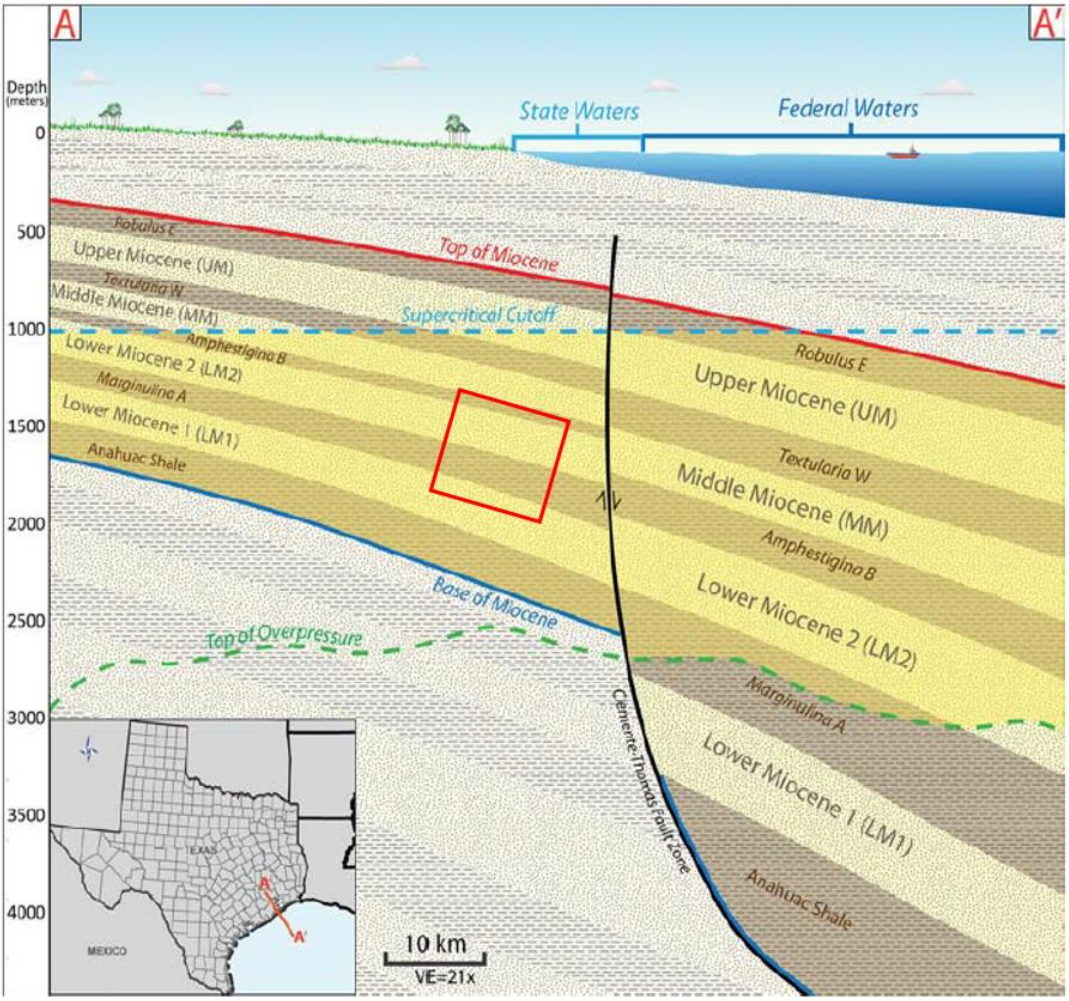

Figure 1.9: Schematic cross section of Miocene strata in offshore Texas. The red polygon represents the interval researched for this study (modified from Wallace et al., 2014).

1.5: PROJECT GOALS

The HI 24L Field is a remarkable field based on its natural hydrocarbon accumulations. More specifically, the HC Sand has produced 206 Bcf of natural gas, being the highest in the TSW of all individual sand reservoirs (Figure 1.10). The field's hydrocarbon production is the primary motivation for this study. This study tries to determine if the storage capacity for the HC Sand is feasible for a CCS project and if not, how many "HC Sands" are needed to achieve this. A direct conversion of original gas in place (OGIP) to CO_2 tonnes helps in answering this question, assuming that CO_2 can directly replace methane in human-like time scales. However, in order to confidently deem the storage capacity estimates to be accurate, other methodologies have to be utilized and compared for the HI 24L Field.

The main goals of this project are to (1) characterize the stratigraphic and structural geology at the HI 24L Field utilizing existing seismic and well log data and previous work conducted by researchers within the GCCC; (2) generate a geocellular model for future research purposes; (3) compare different storage capacity methodologies and estimates of the field; and (4) provide a workflow for screening CCS prospects in the offshore TSW.

.

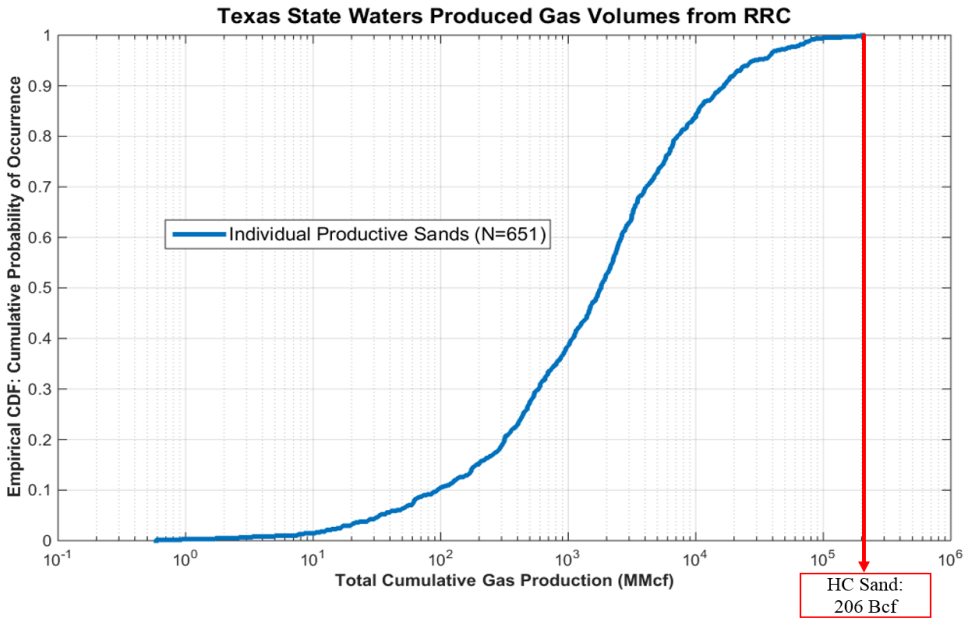

Figure 1.10: Cumulative distribution plot showing the cumulative produced gas volumes from individual sands in the TSW. Note the red arrow that indicates the total gas produced from the HC Sand in the HI 24L Field (from RRC).

1.6: STUDY AREA AND DATASET

For this study, the dataset consists of one three-dimensional (3D) seismic volume with 45 well logs. The TexLa Transition Zone Merge (TexLa Merge) 3D survey is leased to the GCCC from Seismic Exchange Inc. The 3D survey is about 1200 mi^2 (3100 km^2) and is a combination of nine different seismic volumes (Figure 1.11). It contains inlines (N-S direction) ranging from 5000-8645 and crosslines (W-E direction) 5000-7193 with about 110 ft (33.5 m) spacing. The two-way travel time (TWTT) ranges from 0-9966 milliseconds (ms) with a 4 ms sample rate, which translates to approximately 0-30000 ft. However, the interval utilized in this study is between 1400 and 2500 msec two-way travel time (TWTT). The survey lies in the northwestern part of the Gulf of Mexico and extends from the western Bolivar Peninsula at the Houston Ship Channel to the inner part of the West Cameron area in Louisiana. Most of the survey covers the state waters, some of it also reaching onshore and into the federal waters.

The study area (Figure 1.12) that includes the HI 24L Field is about 68 mi^2 (175 km^2) and covers offshore blocks 7, 8, 23, 24, 25, 31, 32, and 33. This area of interest (AOI) lies roughly in between inlines 6425-6785 and crosslines 5905-6335 in the TexLa Merge 3D seismic dataset. A velocity model using synthetic seismograms from six wells with appropriate sonic logs (DeAngelo et al., 2019) aided in converting time-domain interpretations to depth-domain.

Thirty-seven well logs were used for this study. All 37 wells have a digitized spontaneous potential (SP) curve, used to differentiate lithology. Only six of them have neutron/density porosity curves. Both curves were utilized to perform well correlations and generate the facies and effective porosity models.

Regional seismic surfaces and faults were previously mapped (DeAngelo et al., 2019) as well as key log correlations (Olariu et al., in review) throughout the entire 3D

seismic survey. Work undertaken in this research refined those surfaces on a more localized field scale.

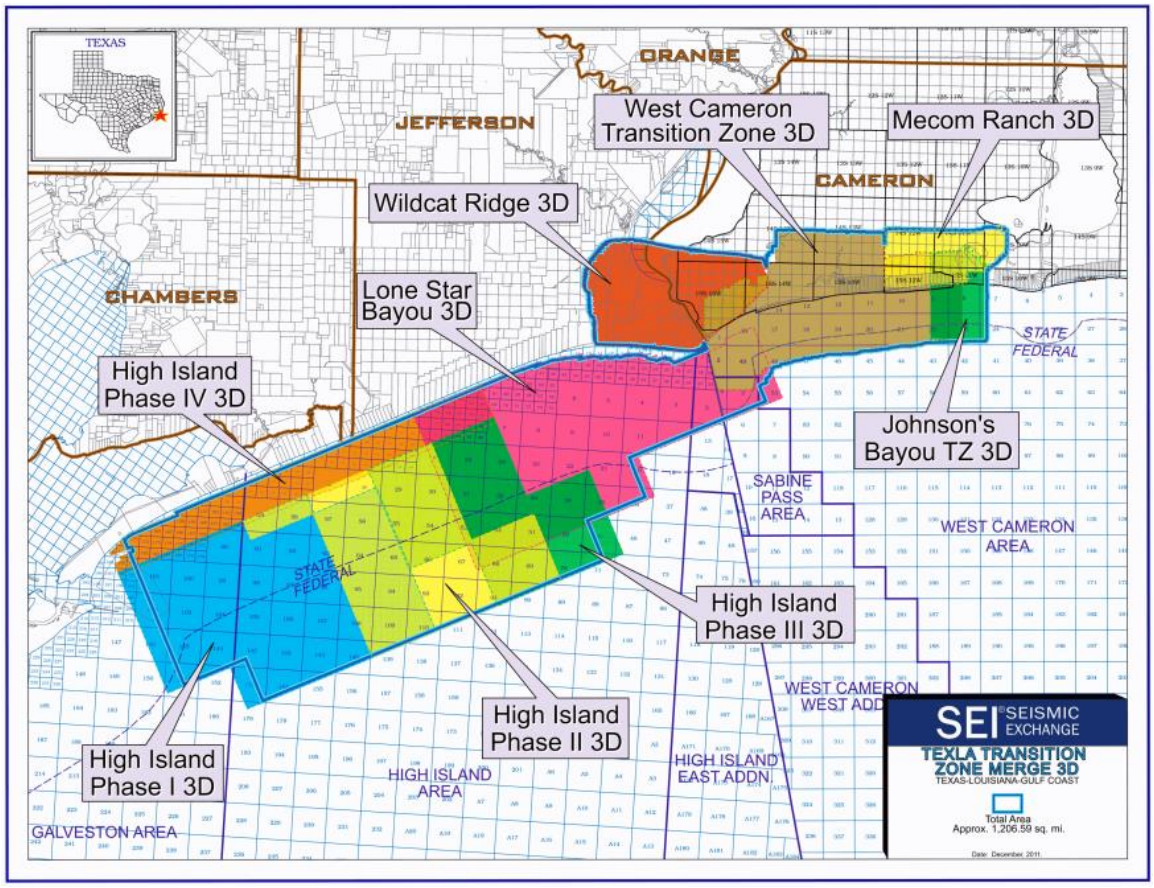

Figure 1.11: TexLa Transition Zone Merge 3D volume. This volume is a combination of 9 different 3D volumes (Seismic Exchange Inc., 2018).

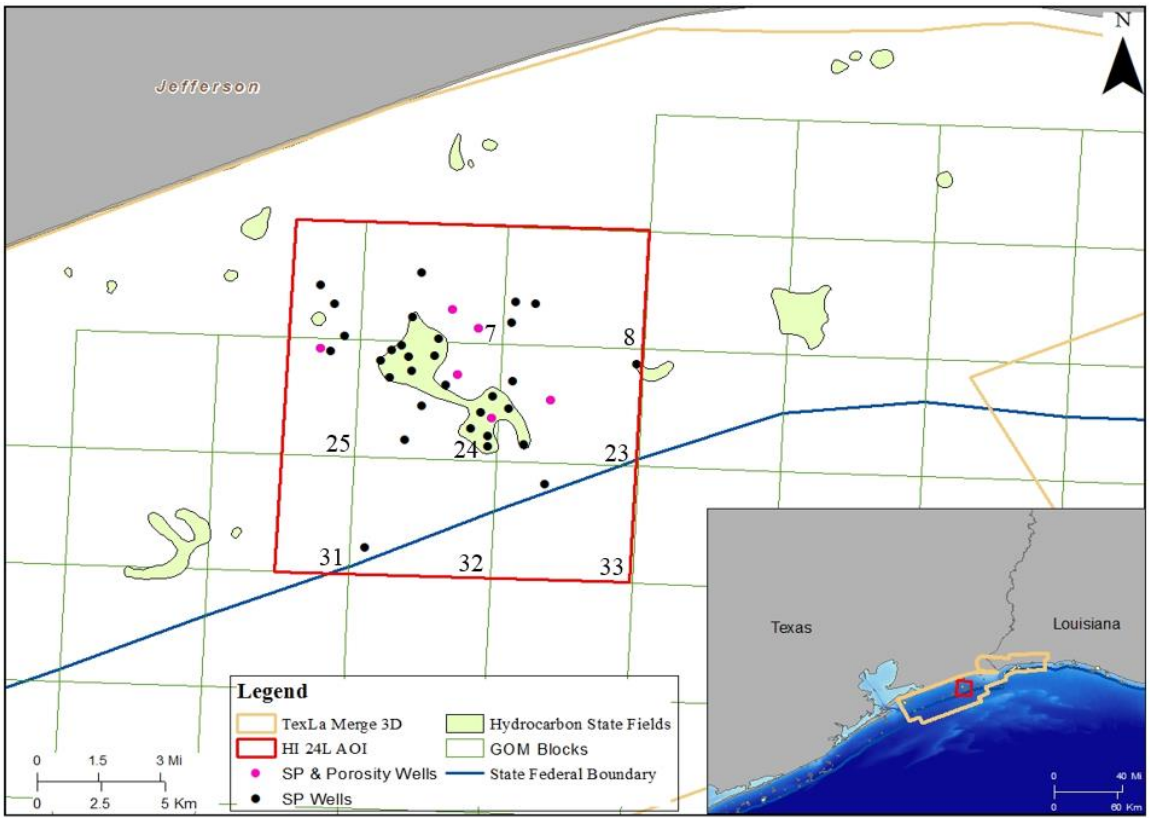

Figure 1.12: Study area and well log data points.

1.7: PROJECT WORKFLOW

The majority of the research comprises the characterization of the HI 24L Field site. Halliburton's Landmark DecisionSpace (DSG10epp.4.03) was used for the bulk of the database management and interpretation. Well log correlations were constructed using Petra™ software. The project workflow (Figure 1.13) is a standard workflow that can be accomplished with any similar software packages. It begins with first characterizing the field by using 3D seismic and well logs, building an understanding of the geologic structure of the field. The characterization then becomes the foundation of the framework by utilizing all interpretations (faults, horizons, well picks, wells, etc.). A 3D geocellular grid can then be created and properties (lithology, effective porosity, and seismic volumes) can be upscaled/attached to the grid according to where the wells intersect it. Variograms can then assist in creating facies and effective porosity models to be simulated stochastically, with multiple realizations. Once the models are finalized, different storage capacity assessments can be estimated and assessed using various methodologies.

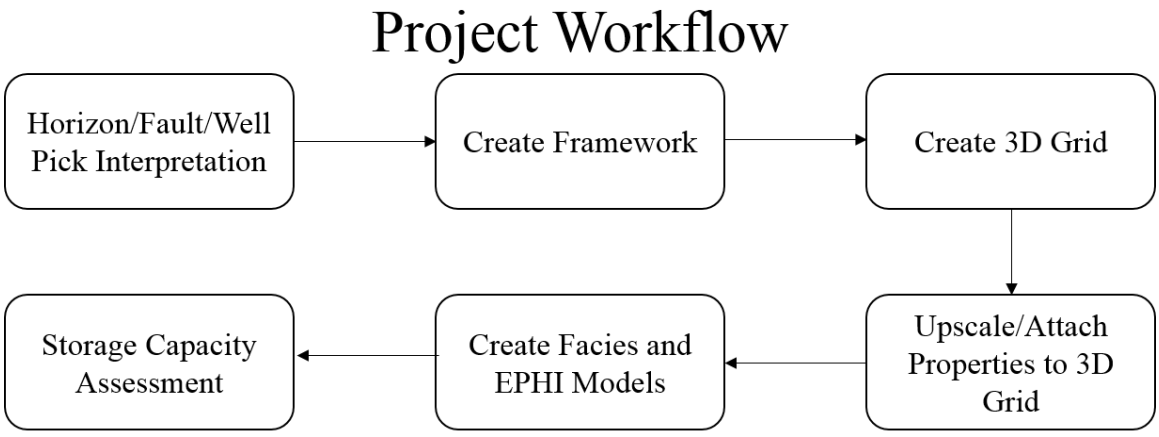

Figure 1.13: Project Workflow

Chapter 2: Characterization of High Island 24L Field

2.1: INTRODUCTION

This chapter covers the first two steps in the project workflow: horizon/fault/well pick interpretation and framework creation (Figure 1.13). The TexLa Merge 3D seismic survey has been recently regionally interpreted by researchers at the Gulf Coast Carbon Center of the Bureau of Economic Geology. Work undertaken for this research refines those interpretation in the region around the HI 24L Field. Several earlier researchers (Galloway, 1989b; Lawless et al., 1997; Hunt and Burgess, 1995; Seni et al., 1994; Kiatta, 1971) have recognized key depisodes, stratigraphic surfaces, and biostratigraphic markers in the Gulf of Mexico that serve as the foundation for well log interpretation within the TexLa Merge 3D area. Using a well log database of about 1700 wells in the TexLa Merge 3D area (Figure 1.11), Wallace (2013) and Olariu et al. (in review) correlated key surfaces within the Lower Miocene section. The main surfaces are maximum flooding surfaces that represent regional marine transgressive episodes and relative sea level rise, interpreted using log character and biostratigraphic markers. Due to their age (1960's), most of the wells have only a spontaneous potential (SP) curve to help differentiate lithology (sand vs. shale), and lack gamma-ray logs that are more traditionally used. Picking key surfaces on well logs allows correlation to seismic using an appropriate time/depth conversion to better understand the geologic structure of the HI 24L Field.

In the TexLa 3D seismic survey, previous work from DeAngelo et al. (2019) regionally mapped and interpreted approximately 300 faults. Figure 2.1 provides an example with multiple faults shown in various colors intersecting a time slice. This fault interpretation used a methodology (Bahorich and Farmer, 1995) that utilizes semblance-based coherency time slices to guide interpretation of stratigraphic discontinuities such as

faults. After the faults were interpreted on a regional scale, seismic horizons tied to surfaces picked in well logs were mapped. The point of maximum retrogradation is considered (Galloway, 1989a) to be a maximum flooding surface (MFS) and the *Amph B* Shale is associated with MFS09. Therefore, a total of six different maximum flooding surfaces (MFS04, MFS05, MFS08, MFS09, MFS10, and MFS12) were regionally interpreted by DeAngelo et al. (2019) on vertical seismic sections separated by 2200 ft (660 m). An example of data interpretation used to map MFS05 throughout the TexLa Merge 3D survey is provided in Figure 2.2. Using the wells (depth) and the seismic data (time) in conjunction, a velocity model was created using a total of six wells, converting time-domain interpretations into depth-domain (DeAngelo et al., 2019).

These regional seismic and well log interpretations served as the initial dataset for this project, providing guidelines for the characterization of the HI 24L Field. Further refinement of this initial dataset in the HI 24L study area was undertaken as part of the research presented here. The next two sections in this chapter provide details of this refinement effort and the overall workflow of interpreting well logs and seismic to create the stratigraphic framework for 3D geocellular modeling, as presented in Chapter 3.

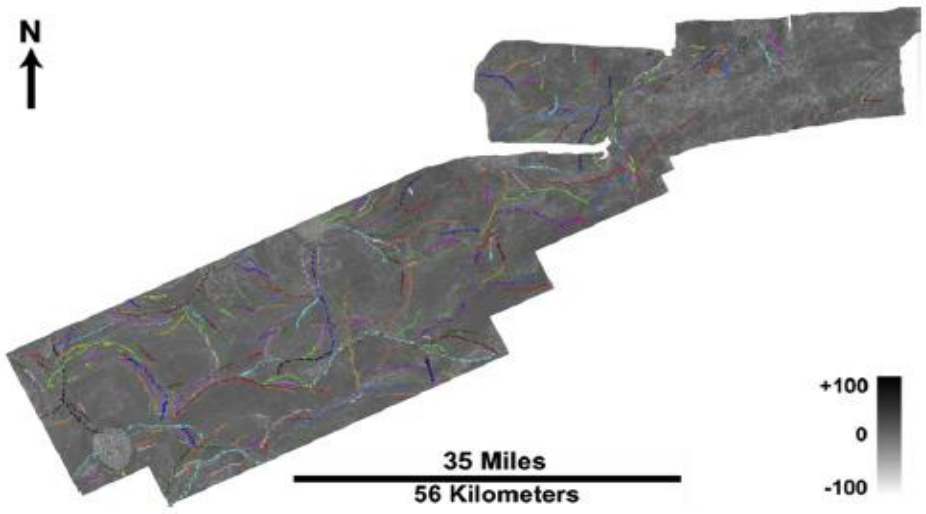

Figure 2.1: Interpreted faults (in color) for a semblance attribute time slice in TexLa Merge 3D survey (DeAngelo et al., 2019)

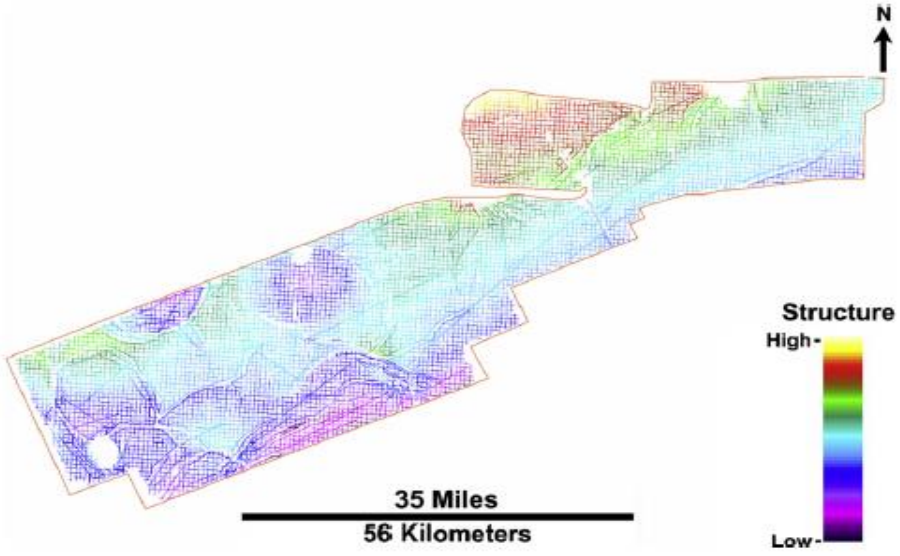

Figure 2.2: Horizon interpretation for MFS05 in TexLa Merge 3D survey (DeAngelo et al., 2019)

2.2: WELL LOG INTERPRETATION AND CORRELATION

All 37 wells used in this project have an SP curve that served to identify porous and permeable zones in the formation by recording the electrical potential difference between the borehole and surface. Typically sandstones have higher permeability and porosity than shales, which helps in differentiating lithology and estimating effective porosity (EPHI) using the SP curve. SP data were standard for wells of the vintage in the study area (1960's). After normalizing the SP curves for all the wells from 1 to 0 (minimum, maximum), restricted to the Lower Miocene section, a cutoff value (0.33) was set to differentiate sand vs. shale in the well log. Values greater than 0.33 were considered clean sands.

The deposition of thick shales above sandy sections can often be attributed to a major transgressive event. For the study area, this is the standard interpretation for the *Amph* B Shale (350 ft; 107 m). Two other MFS's were also utilized for this study (MFS10 and MFS11). The stratigraphic chart and type log for the HI 24L Field (Figure 2.3) illustrates key stratigraphic packages and regionally interpreted surfaces. Episodes of progradation occur below MFS10, resulting in the deposition of the HC Sand (200 ft thick; 60 m), interpreted as deltaic sand deposits (Seni et al., 1997). These sandstones are overlain by thick shales, acting as a great top seal. Moving higher in the stratigraphic column, a thick unit of aggradational sands (1700 ft; 520 m) was deposited, referred to here as the Storage Interval of Interest (SIOI). The blocky log character of the sands in this unit was mostly characteristic of shallow marine and delta front environments, typically composed of a mix of delta fringe and marine shelf blanket sands (Seni et al., 1997). An interpretation of the sands as stacked channels is difficult because the seismic resolution (70 ft; 21 m vertically) does not allow incisions to be seen. Interlayered among these stacked sands, small to medium thick shale layers (<100 ft, ~30 m) can act as potential flow barriers for

fluid migration as the primary seal is the *Amph* B Shale (Beckham, 2018). The *Amph* B Shale is a muddy package that can be as much as 525 ft (~160 m) thick in the down dip (more offshore) areas and averages about 350 ft (~107 m) within the AOI. The HC Sand and the SIOI are considered the primary units for estimating CO_2 storage capacity because of their high sand content (60-65% NTG) and favorable effective porosity (28-33%).

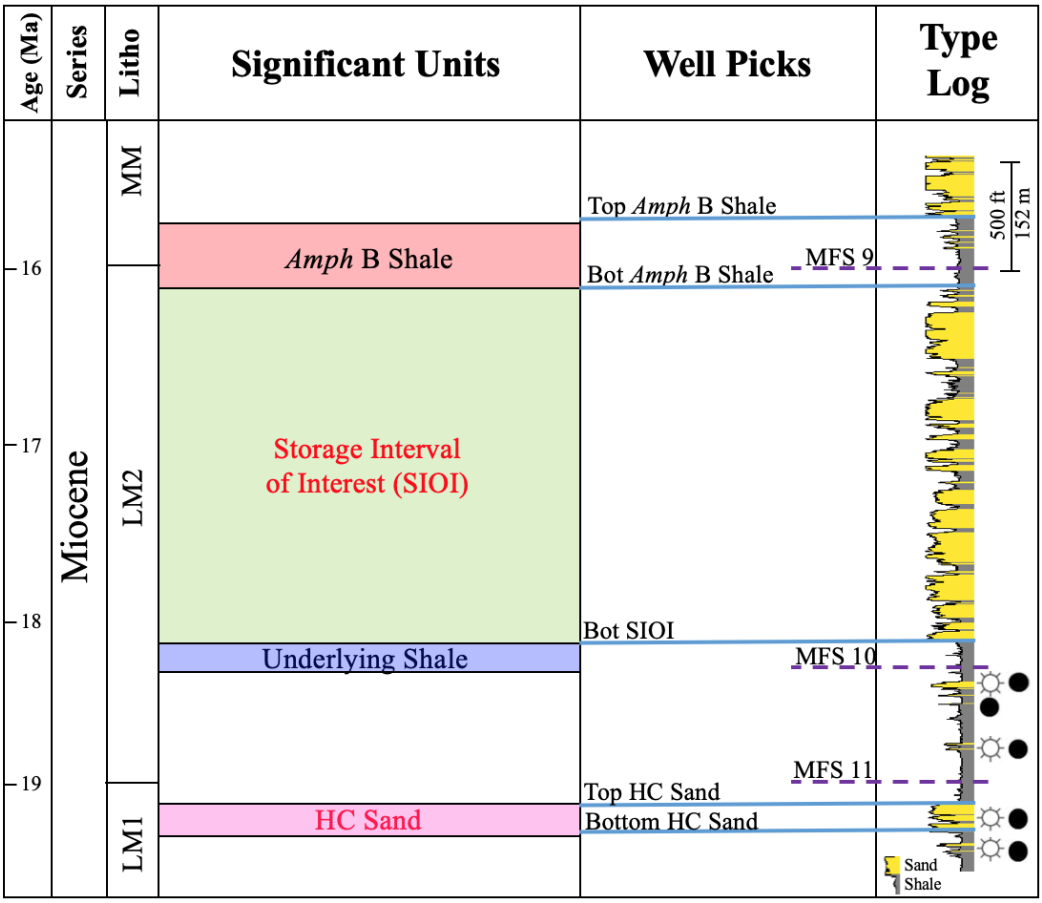

Figure 2.3: Stratigraphic chart and type log for High Island 24L. The Storage Interval of Interest (SIOI) is characterized by thick sands and capped by the *Amph* B Shale. The HC Sand is a single sand reservoir capped by a thick shale. These zones are modeled to estimate CO_2 storage capacity within the field.

A structure map of the HC Sand reservoir is shown in Figure 2.4 to illustrate the two subsequent well log cross sections and two seismic cross sections. The well log correlations helped to accurately define the stratigraphy for the HI 24L Field. The *Amph* B Shale was the package that was easily identifiable in the well log cross sections because a thick muddy unit was recognized in all of the well logs. The four defined intervals are highlighted in each of the well log cross sections (Figure 2.5 and Figure 2.6) with three maximum flooding surfaces correlated across (MFS09, MFS10, MFS11), all correlating to Figure 2.3. The SIOI seems to be sandy throughout the entire HI 24L Field. Further refinement, while possible, within the SIOI does not contribute to the goals of this study to calculate storage capacity because the whole section was considered as only one interval. However, an example of interpreting individual stratigraphic features within the SIOI is presented in Ramirez Garcia's (2019) thesis, focused on a nearby field (High Island 10L). The *Amph* B Shale, SIOI, and Underlying Shale packages were modeled for estimating CO^2 storage capacity in the SIOI with a total of three different intervals. The same was done for the HC Sand, but only for two intervals: the top seal between MFS10 and Top HC Sand surfaces and the HC Sand.

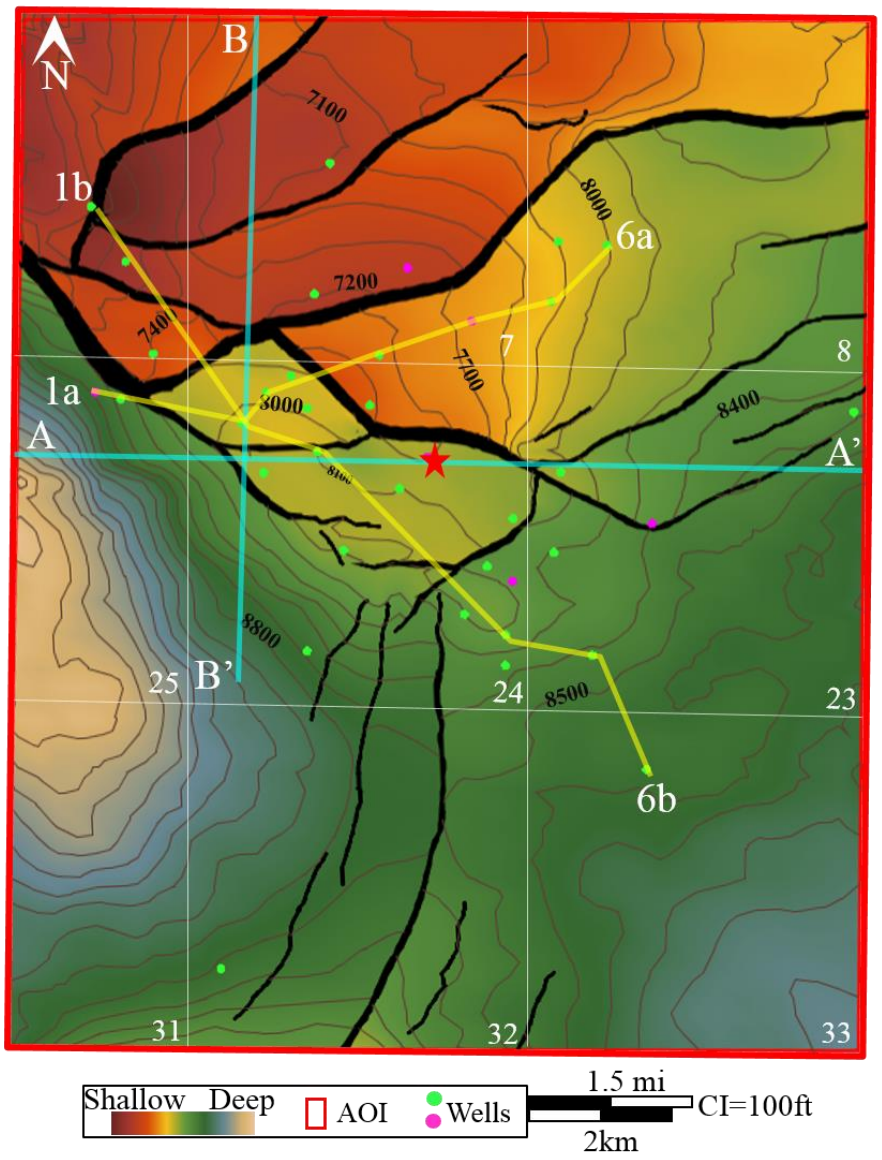

Figure 2.4: Structure map of the HC Sand reservoir. Two seismic cross sections (cyan) and two well log cross sections (yellow) are outlined. Green circle symbols indicate wells with only SP curves and magenta well symbols with both SP and porosity curves. This well color scheme is adopted in subsequent figures. Red star represents the well used to perform the well-tie.

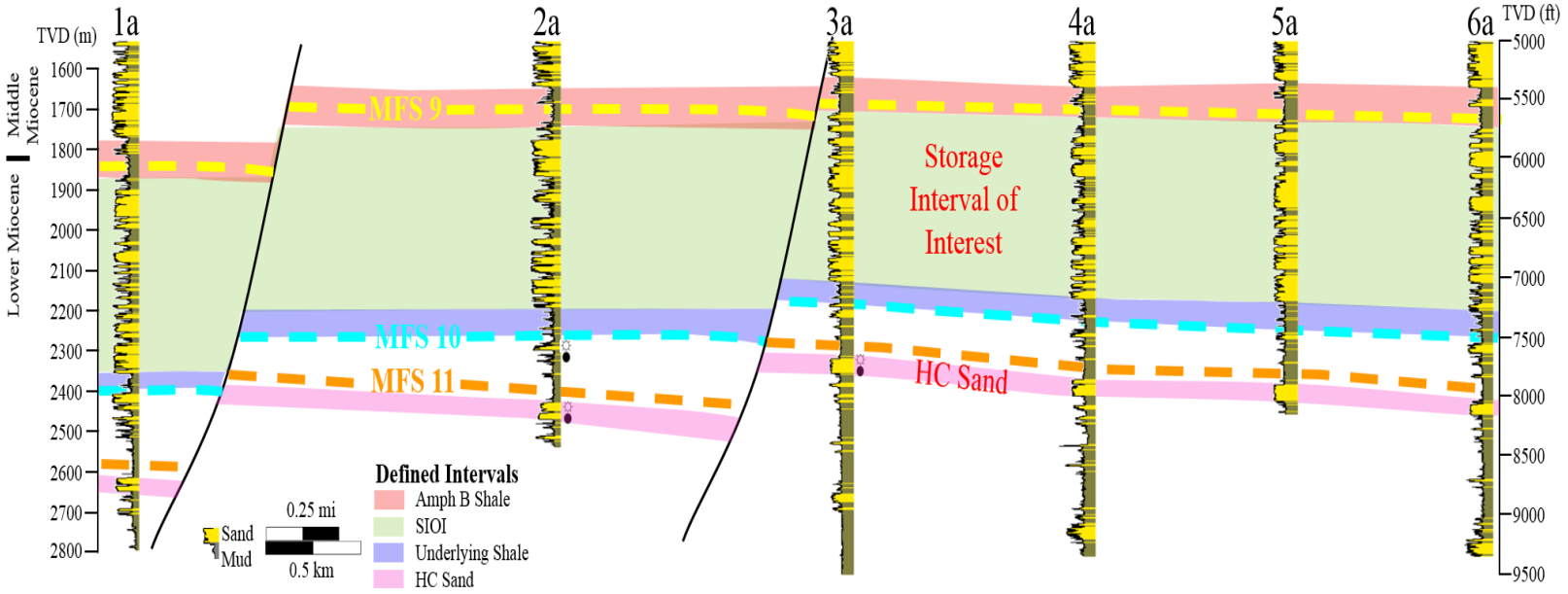

Figure 2.5: Strike well-log cross section (1a-6a). Section line indicated in Figure 2.6. See Figure 2.3 for stratigraphic column.

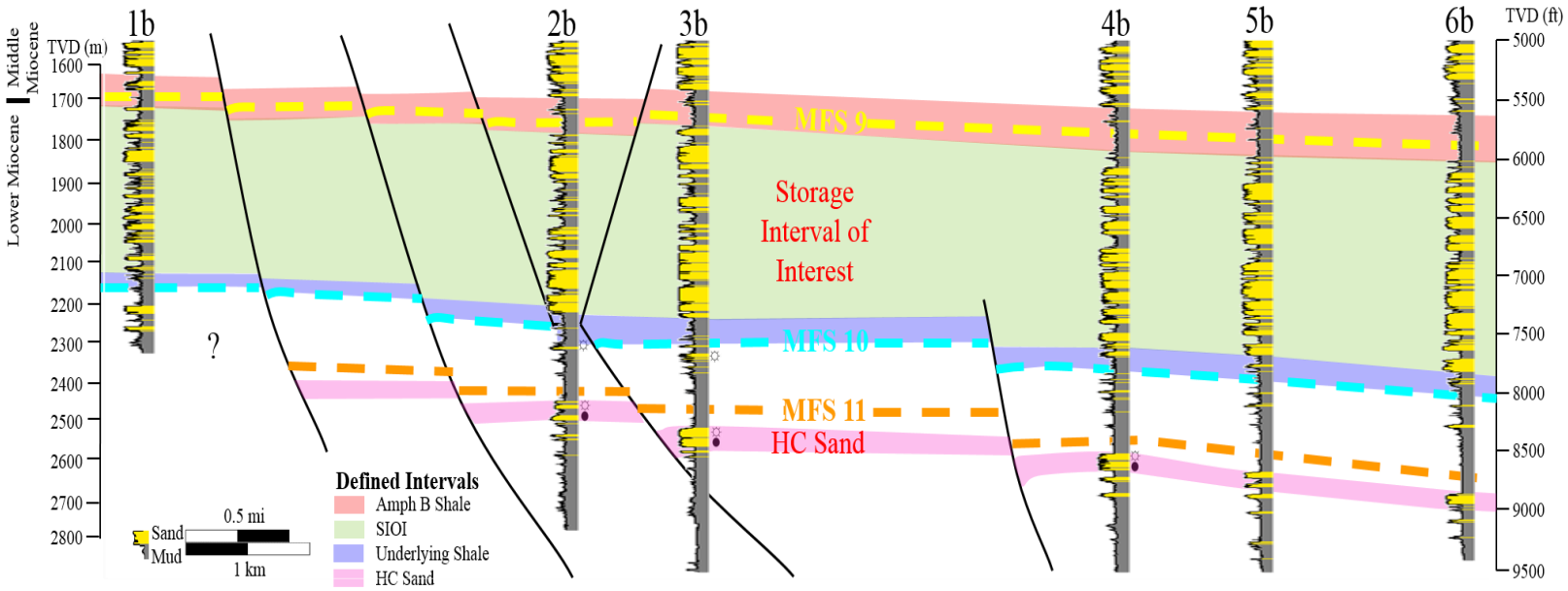

Figure 2.6: Dip well-log cross section (1b-6b). Section line indicated in Figure 2.6. See Figure 2.3 for stratigraphic column.

2.3: FAULT INTERPRETATION

The goal of interpreting faults in this field was to recognize the important structural features to construct structure maps that resembled the complexed geology of the field. Growth faults at the HI 24L Field play an important role in why this field has produced a regionally significant amount of hydrocarbons. In seismic, the rollover anticlines on the hanging walls of the growth faults were the main hydrocarbon play for the HI 24L Field (Figure 2.7, red arrows). Many of them have significant offsets (500 ft; 152 m) that aid in the juxtaposition of sand and shale across faults. For example, the HC Sand has 400-900 ft (120-275 m) of offset in the main fault blocks of the HI 24L Field. Also, smaller listric or antithetic faults were recognized and interpreted because they might potentially act as lateral traps for fluids.

Since most of the larger-offset faults were interpreted regionally by DeAngelo et al. (2019), 24 previously interpreted faults were used for this study within the AOI. With these 24 faults, editing was done to enhance this field-scale characterization. Editing either involved deleting some fault picks or extending specific faults (Figure 2.8). This was an important step because many of these faults connected with other smaller faults or branched out and therefore had to be acknowledged within the framework workflow. Also, 29 new faults were interpreted using every 5^{th} inline and crossline in the 3D seismic volume, focusing on observed offset among the seismic reflectors. The total number of faults in the AOI thus increased from 24 previously interpreted faults to 53 faults (Figure 2.9). Several of the faults were not used in the framework building to simplify the overall framework because they were located just outside the AOI or were not important when calculating the storage capacity in the footprint areas (more on this in Chapter 4).

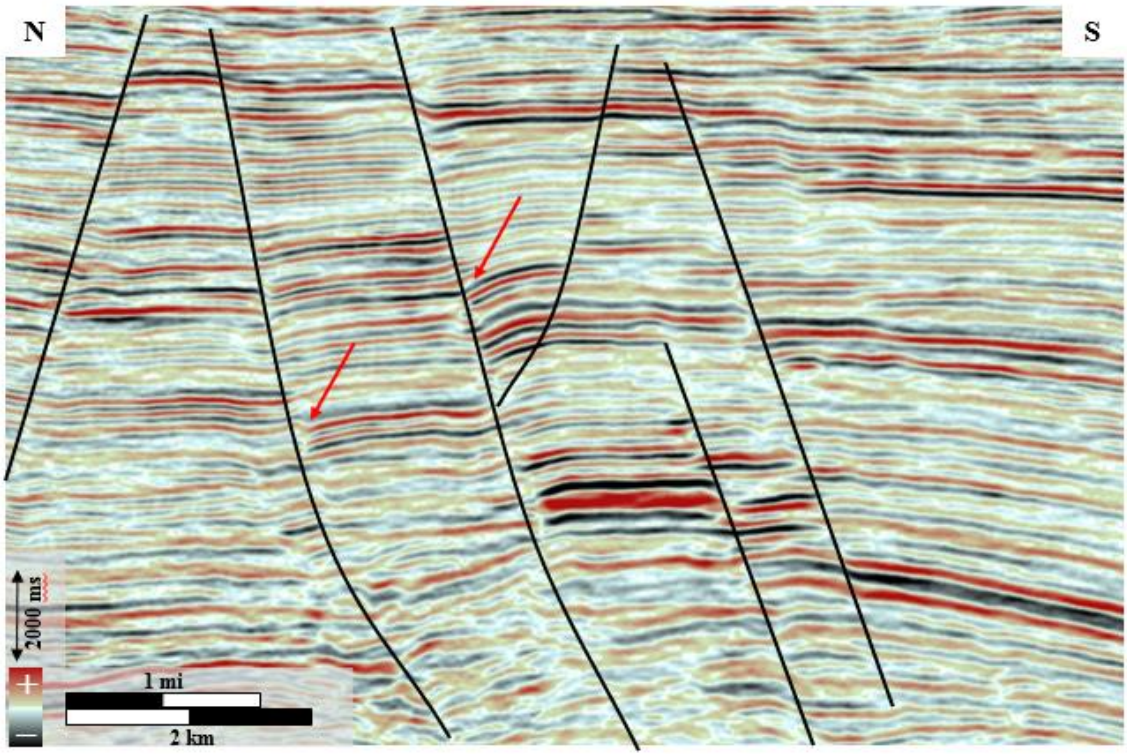

Figure 2.7: Evidence of growth faults within the HI 24L Field. Red arrows indicate curvature and thickening of downthrown stratigraphy, likely contemporaneous with fault development. Section line runs from north (left) to south (right), just east of B-B' line (Figure 2.4).

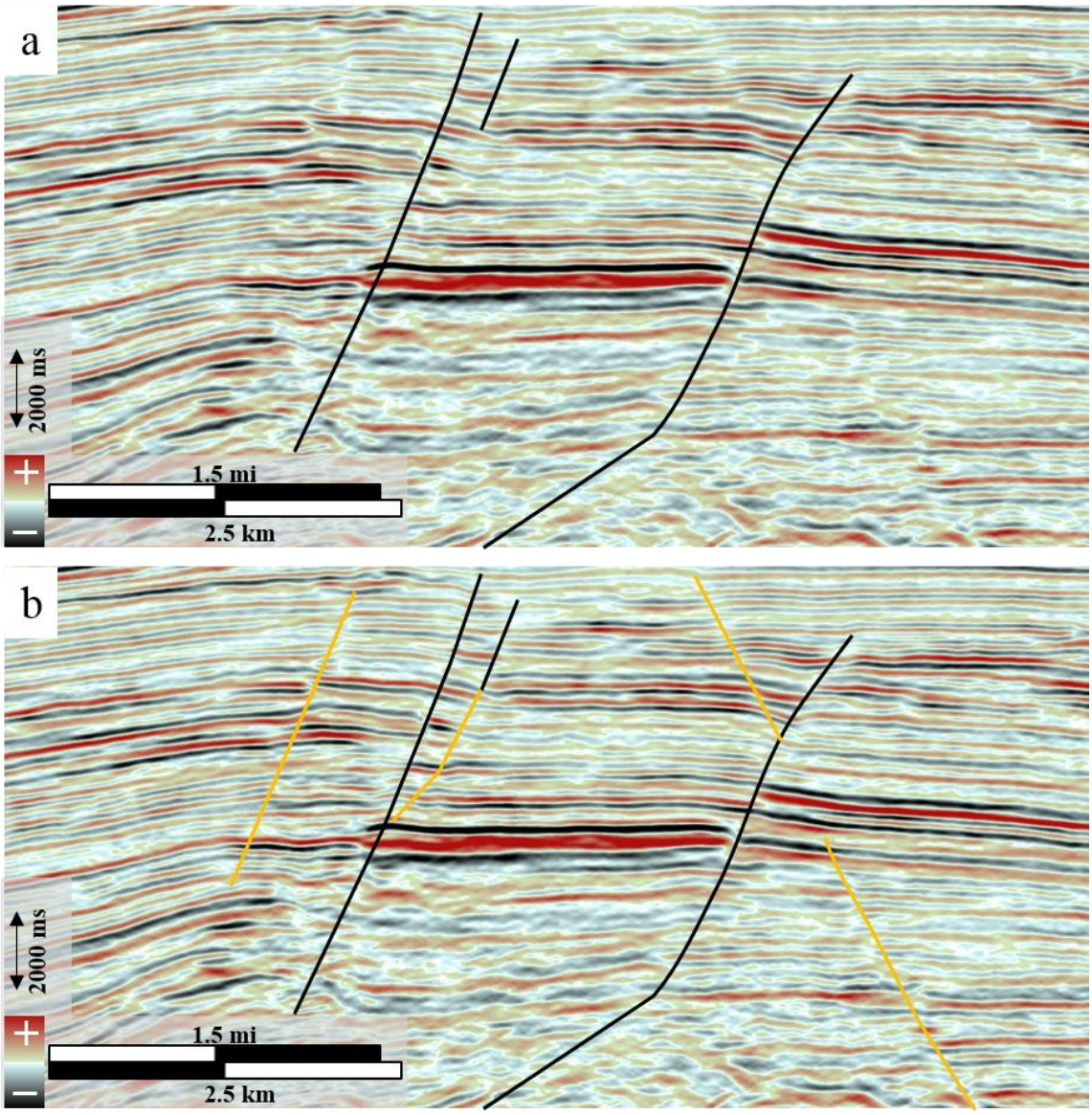

Figure 2.8: Additional interpretation of faults in this study. (a) Faults previously interpreted by DeAngelo et al. (2019) (b) Refined fault interpretation by adding and/or extending faults (shown in orange).

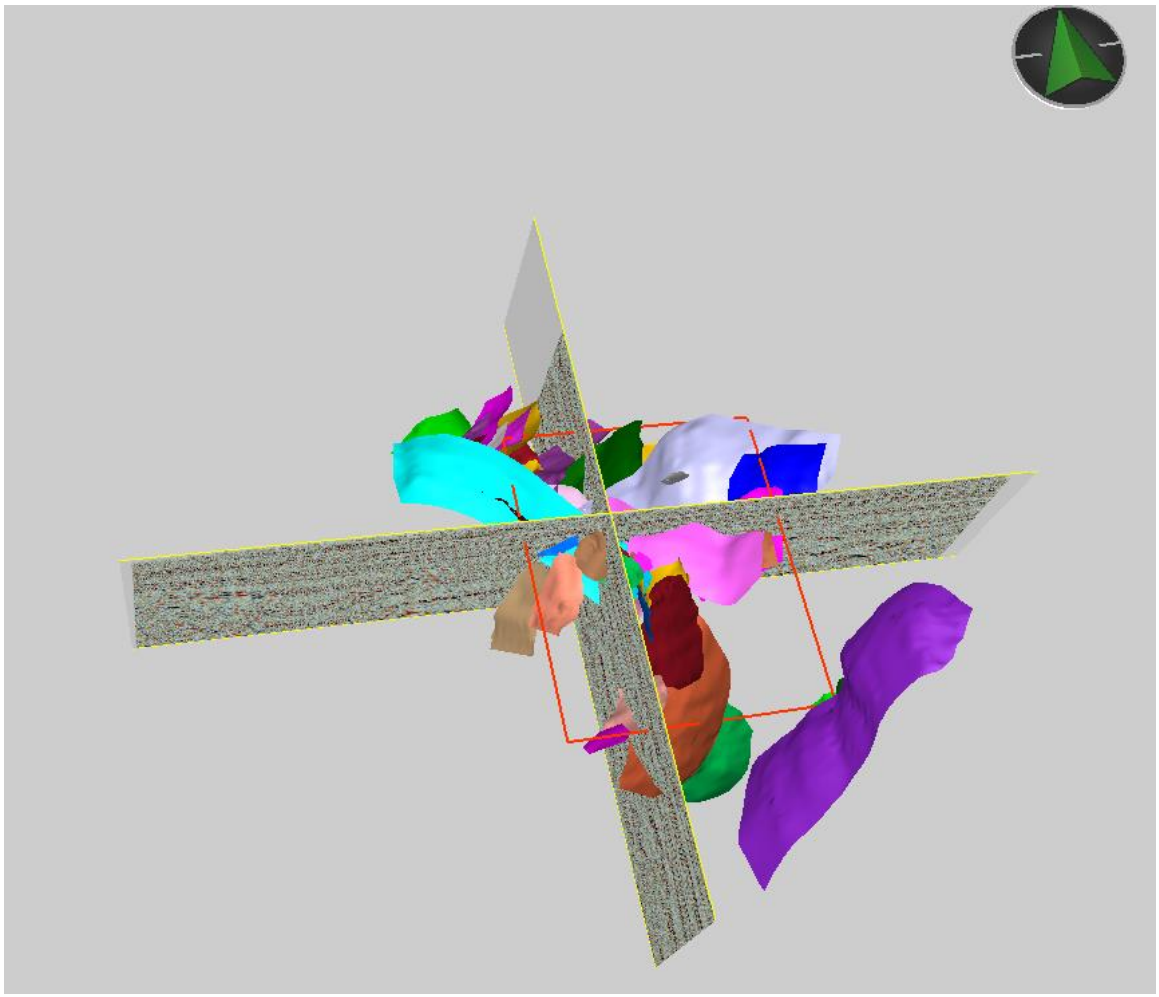

Figure 2.9: Perspective view illustrating the 53 interpreted faults in the HI 24L Field. Inline and crossline sections shown with faults in various colors and AOI in red polygon.

Missing Fault Section

To elaborate on how heavily faulted the HI 24L Field is, several wells show evidence of a missing section that is expected in normal fault settings. A well that drills through a normal fault has the potential for stratigraphy to be missing due to the offset and angle of the fault. The schematic (Figure 2.10) represents a well intersecting a normal fault, only capturing what is in bright red of a certain section, which is far thinner than the full thickness of the pink layer. An example of this within the HI 24L Field can be seen in Figures 2.11 and 2.12. The seismic shows that across these four wells, there are several faults that cut the stratigraphy. In the second well from the left, the well intersects a large growth fault as the location of this intersection is outlined in the red polygon. This same polygon is delineated on the well log section for reference, and it is apparent that most of the section, the *Amph* B Shale in this case, was missing in the well. The top and bottom of the package were picked in each of the four wells to estimate how much section was missing, roughly about 250 ft (~76 m). It does not mean that the *Amph* B Shale disappeared or abruptly thinned stratigraphically, just that the well merely intersected a subset of the stratigraphy because of a fault offset of at least 250 ft (~76 m).

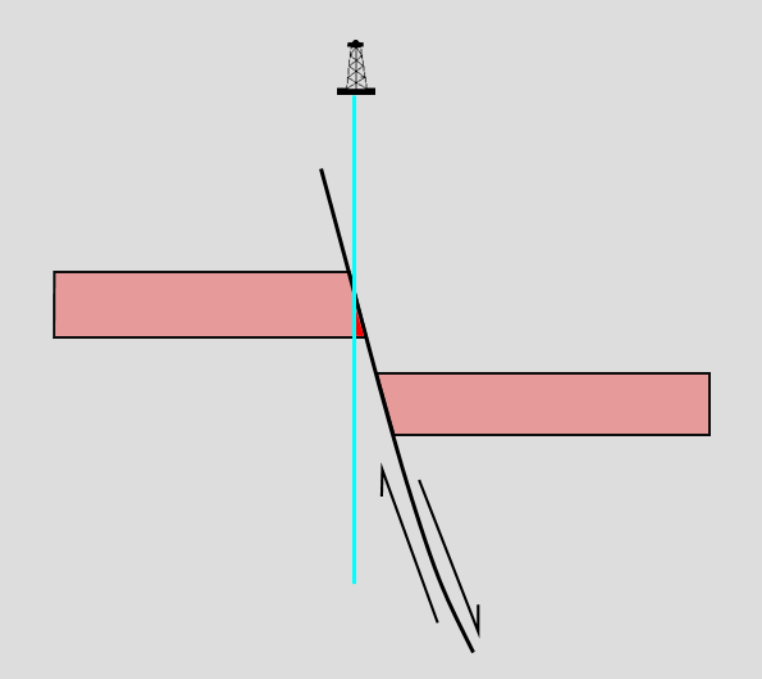

Figure 2.10: Schematic diagram illustrating the concept of missing section caused by normal faulting. Bright red section is the area intersected by the well.

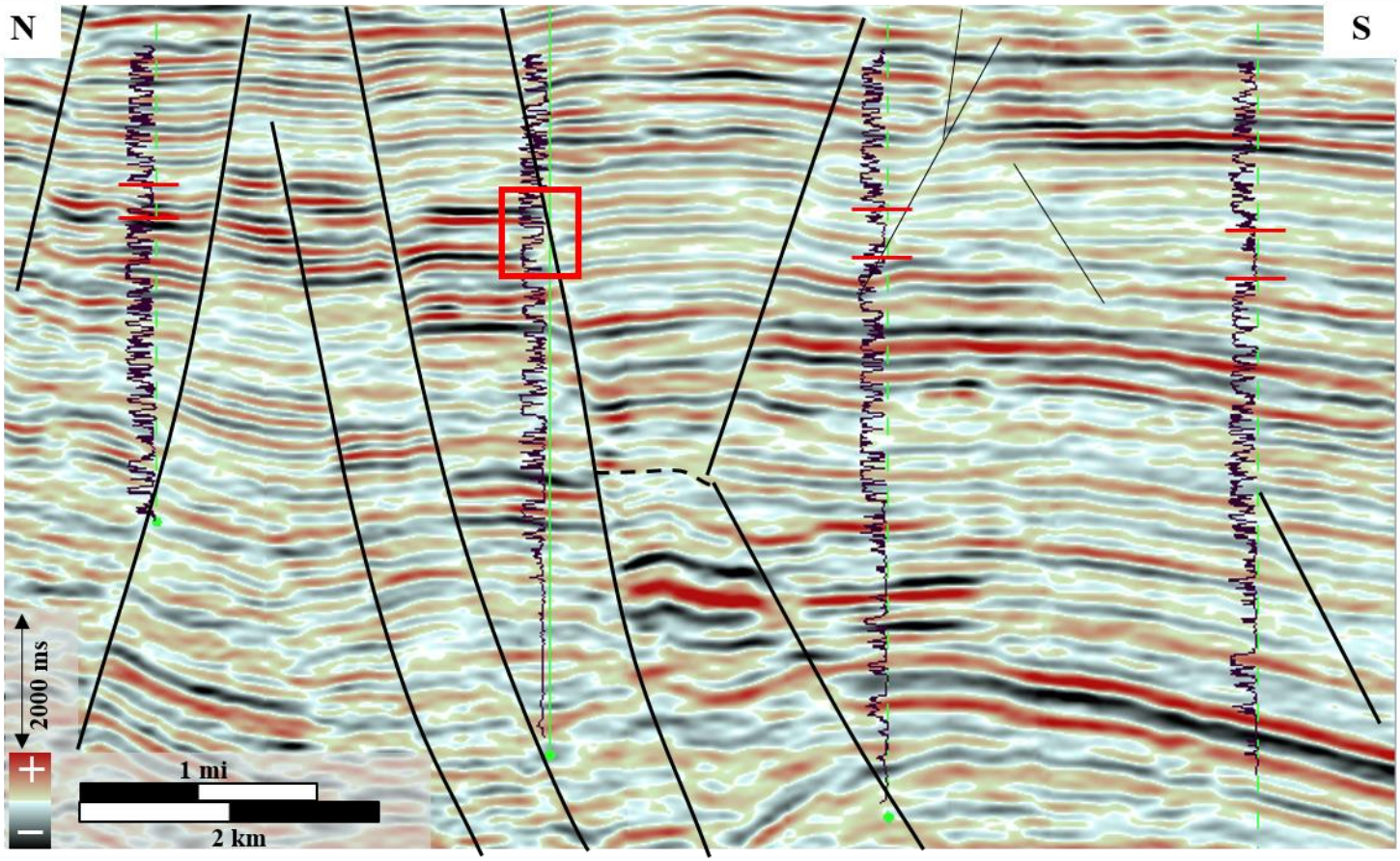

Figure 2.11: Seismic section showing evidence of missing section (seen in red rectangle) due to normal fault. The top and bottom of the *Amph* B Shale are delineated in red for each well. Note where fault intersects well in red polygon. SP curves are in black along green well path. Additional well log detail provided in Figure 2.12.

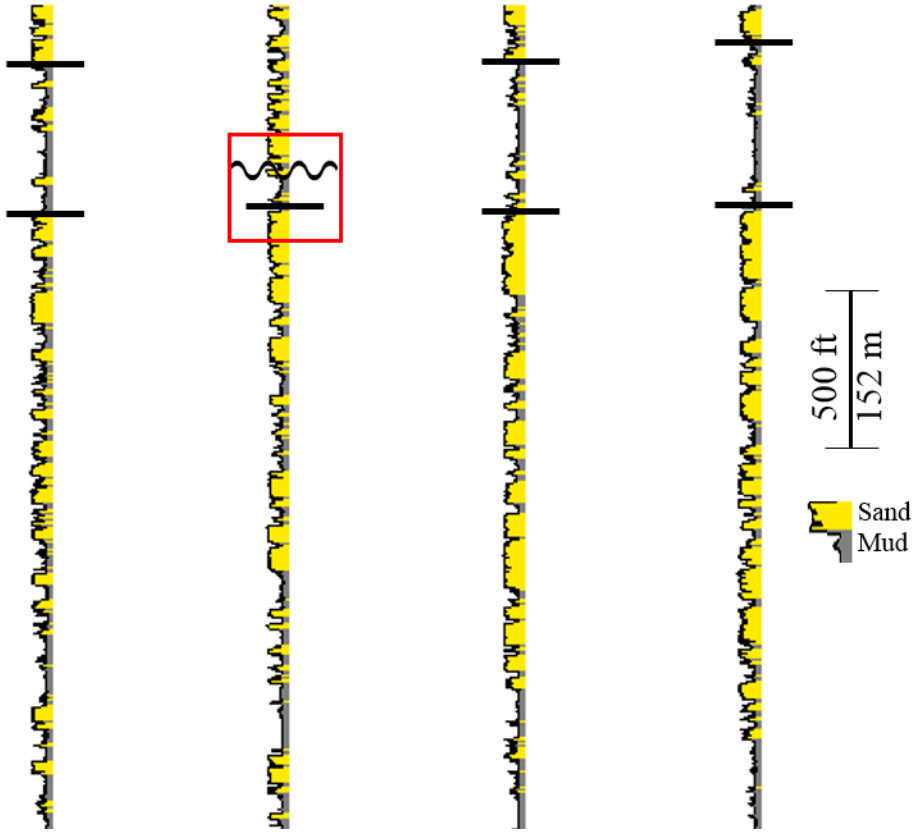

Figure 2.12: Well-log section showing missing section due to normal faulting. Cross section is flattened near the bottom of the *Amph B* Shale. Black lines represent top and bottom of *Amph B* Shale. Red polygon and wells are the same as in Figure 2.11. Wells are equally spaced.

2.4: SEISMIC HORIZON INTERPRETATION

In order to properly integrate well and seismic data, aside from the velocity model, a well-tie was accomplished by creating a synthetic seismogram using two specific log curves: bulk density (g/cm^3) and sonic (us/ft). The calculation of acoustic impedance (the product of density and velocity) and reflection coefficients can then be drawn. With these two properties generated, a synthetic seismogram can be created and correlated to the seismic (Figure 2.13). The main control point was the HC Sand because it can easily be picked on a well log and also on seismic. The well-tie had a correlation value of the synthetic to the actual seismic of about 54%. Possible missing sections, slight well deviations, length of log suite, and other factors can influence this value. Nevertheless, this general well-tie workflow provided a better understanding of what horizons to interpret, correlating to the surfaces interpreted on the well logs. The well that was used for this workflow is shown in Figure 2.4.

A total of nine different horizons were interpreted within the seismic volume. Characterizing the HI 24L Field on 3D seismic was clearer, guided by well-tie and previous interpretations of regional horizons. Each horizon was interpreted every 5 inlines and cross lines, 500 ft (152 m) and 600 ft (183 m), respectively, with also some arbitrary lines crosschecking every interpretation (Figure 2.14). The southwestern side of the AOI was defined by an isolated mini-basin, and interpretation was not as important here because much of the seismic reflectors were extensively continuous. Interpreting inside fault blocks was the most important part of this process, making sure each horizon matched and was offset consistently across faults. The gaps in Figure 2.14 represent the uninterpretable seismic near the faults. Any specific time shift was then applied to either of the mapped horizons to generate a new horizon, still obeying the geologic structure.

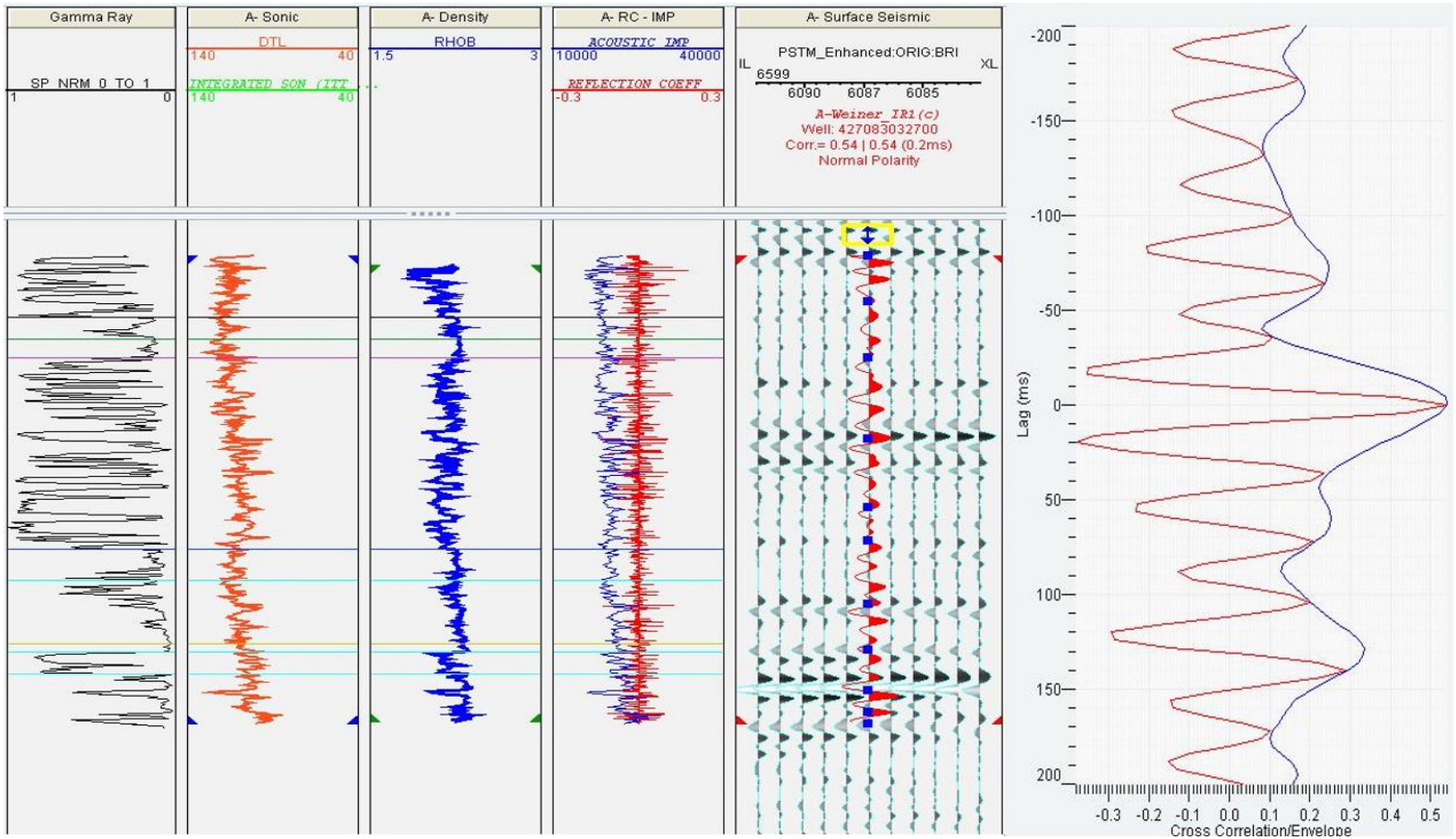

Figure 2.13: Well-tie synthetic for time/depth conversion. See Figure 2.4 for well location.

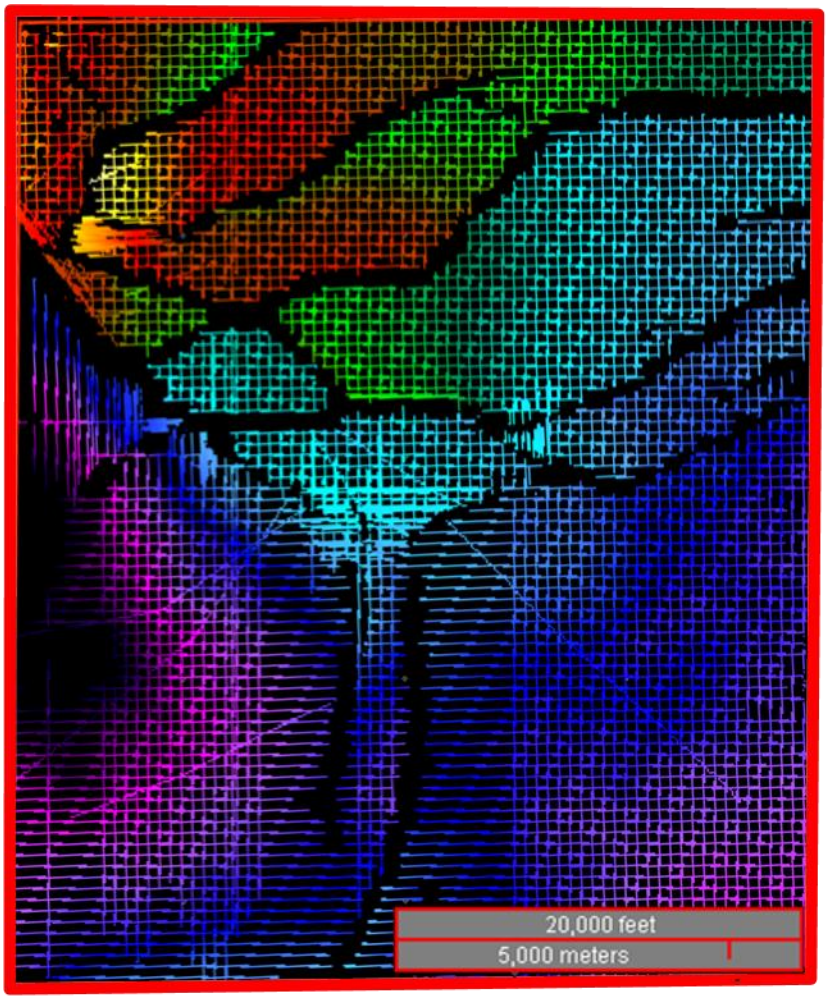

Figure 2.14: Horizon interpretation of the HC Sand in AOI (red rectangle).

The fully interpreted seismic cross sections (Figure 2.15 and 2.16) illustrate how many and which of the horizons were interpreted. The *Amph* B horizon was the first horizon interpreted for this project, starting with the assumption that the dim seismic interval (low amplitude) represented the *Amph* B Shale. This was picked before the well tie and then later realized to be inaccurate. After the well-tie, Top *Amph* B Shale and Bot *Amph* B horizons were interpreted, more accurately mapping the *Amph* B Shale. MFS09 and MFS10 represent the maximum flooding surfaces on the well logs, and the other horizons in between the SIOI (Mid Aggrad and Mid-Bot Aggrad) were the results of time shifting horizons. The bottom of the SIOI is defined by the Bot SIOI horizon. The HC Sand was interpreted by recognizing a strong amplitude reflector due to a strong impedance contrast, inferring a hydrocarbon-charged reservoir. The bright seismic reflector can be seen in between the third and fourth fault from the left in Figure 2.16.

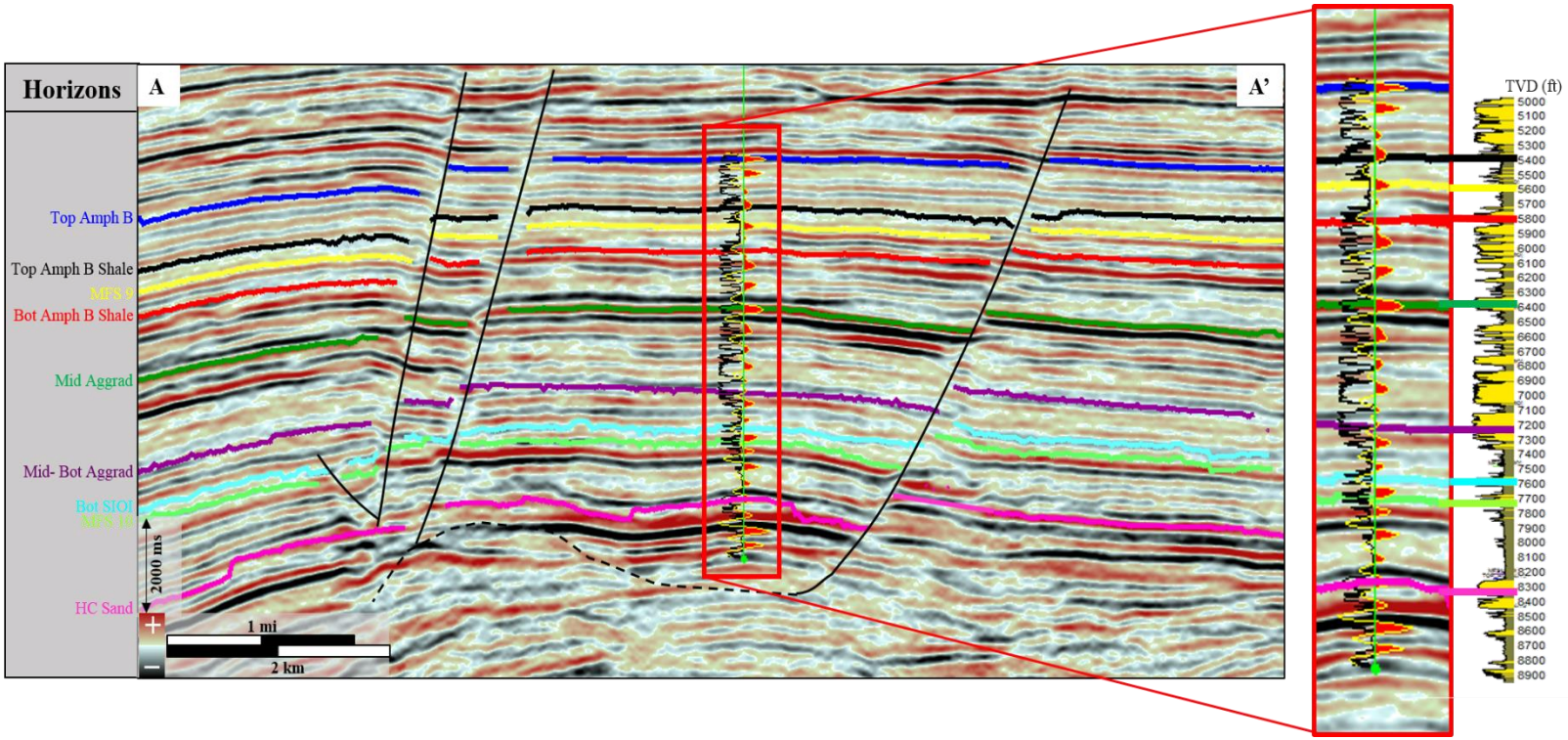

Figure 2.15: Seismic strike cross section with detailed well tie and labeled interpreted horizons. Section line from Figure 2.4.

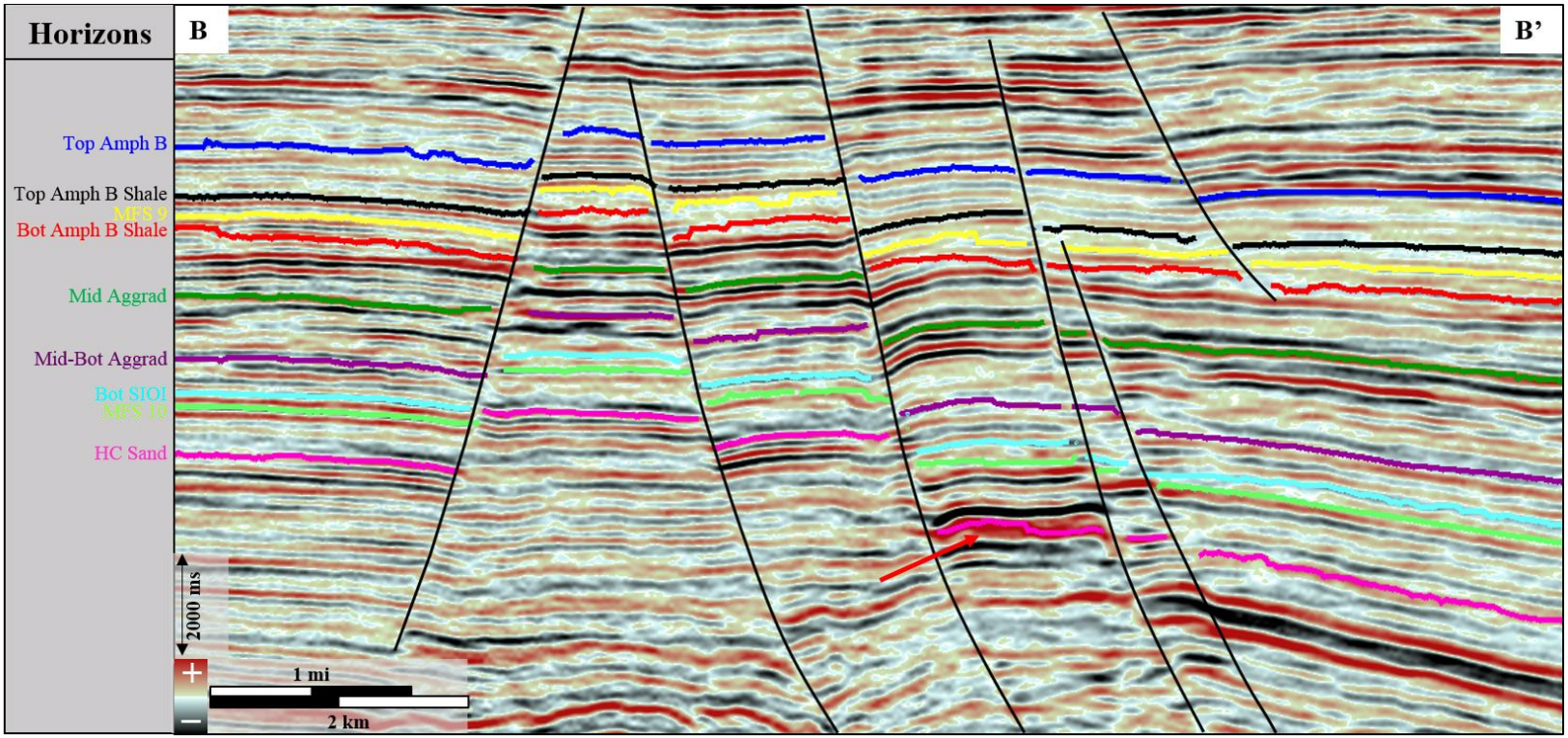

Figure 2.16: Dip seismic cross section with labeled interpreted horizons. Section line from Figure 2.4. Note the strong reflector of the HC Sand pointed out by the red arrow.

2.5: STRATIGRAPHIC FRAMEWORK

The characterization of the HI 24L Field involved interpreting faults, correlating surfaces in well logs and tracing them on 3D seismic. These data were used to build the stratigraphic framework of the field. The interpretation of the horizons divided the packages that were important for this study. Fault interpretations defined the structure of the field, mainly to offset the horizons. Everything else that had to be adjusted to accurately have the stratigraphic framework represent the field was secondary. However, a key part in the framework building workflow was appropriately connecting different faults together to resemble a branch-like fault structure.

Fault networking was the most important data aspect for finalizing the framework. Fault networking means connecting the faults, with only one representing the parent or dominant fault to better characterize the surfaces as the seismic was difficult to interpret near the faults. Many of the faults branch out and at times the DecisionSpace software does not automatically recognize it. Without networking the appropriate faults, the structure of the field will look unrealistic, mainly dealing with how the software interprets the data. Having previous literature to compare (Fowler et al., 1987; Brown, 2011), there was a significant difference in how networking faults affected the software's interpreted structure of the field (Figure 2.17). Some faults do not intersect each other and therefore affect the overall continuity of the horizons interpreted close to the faults (notice the small spaced contour lines depicted by blue arrows). As a result, if the faults were not networked, there would be gaps within the fault structure where fluids would potentially migrate up through (red circle on Figure 2.17a). The 3D seismic does not show this.

The overall framework that was used to estimate CO_2 storage capacity for the SIOI included 29 faults, 37 wells, and 4 seismic surfaces: Top *Amph* B Shale, Bot *Amph* B Shale,

Bot SIOI and MFS10 (Figure 2.18). The HC Sand framework was similar but used other surfaces to characterize the package and top seal: MFS 10, Top HC Sand, and Bot HC Sand. In total, six different horizons were utilized for this study.

The workflow of interpreting the correct horizons and faults for the AOI to then building the stratigraphic framework to where the software accurately interprets the stratigraphy and structure was a significant part of this study. Characterization first began by picking key surfaces on the well logs to then performing a well-tie to correlate them to specific 3D seismic horizons. Along with this, fault interpretation was crucial because the field was shown to be dominated by growth faults. The surfaces represented the stratigraphy and the faults the structure of the HI 24L Field. With such a stratigraphic framework defined and interpreted, the 3D geocellular grids were created.

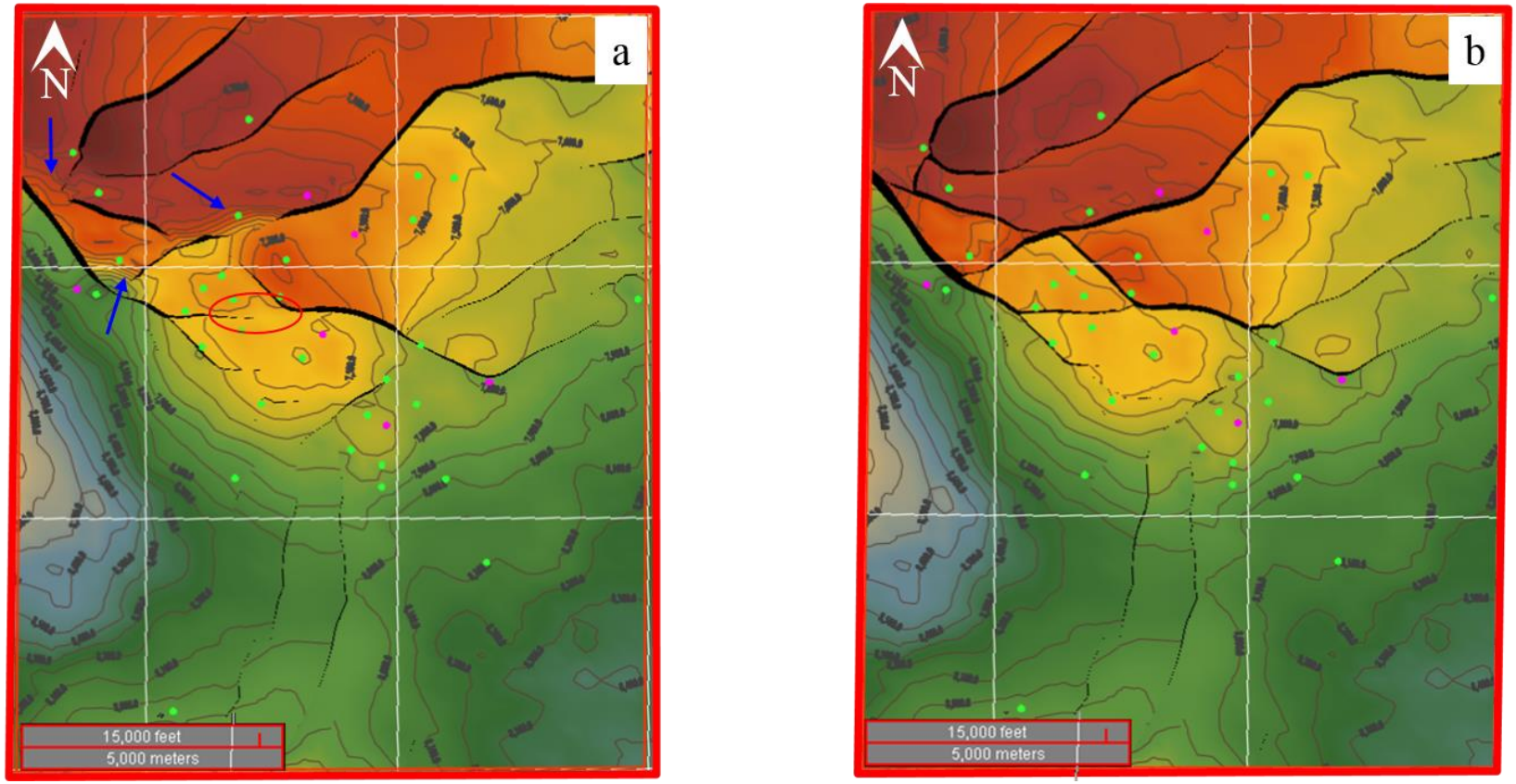

Figure 2.17: Fault networking structure maps. (a) Structure map without fault networking as the blue arrows point to the areas where the geologic structure looks unrealistic. The red circle shows a gap between faults when in reality they should intersect. (b) Structure map with fault networking. Contour interval is 100 ft (~30 m).

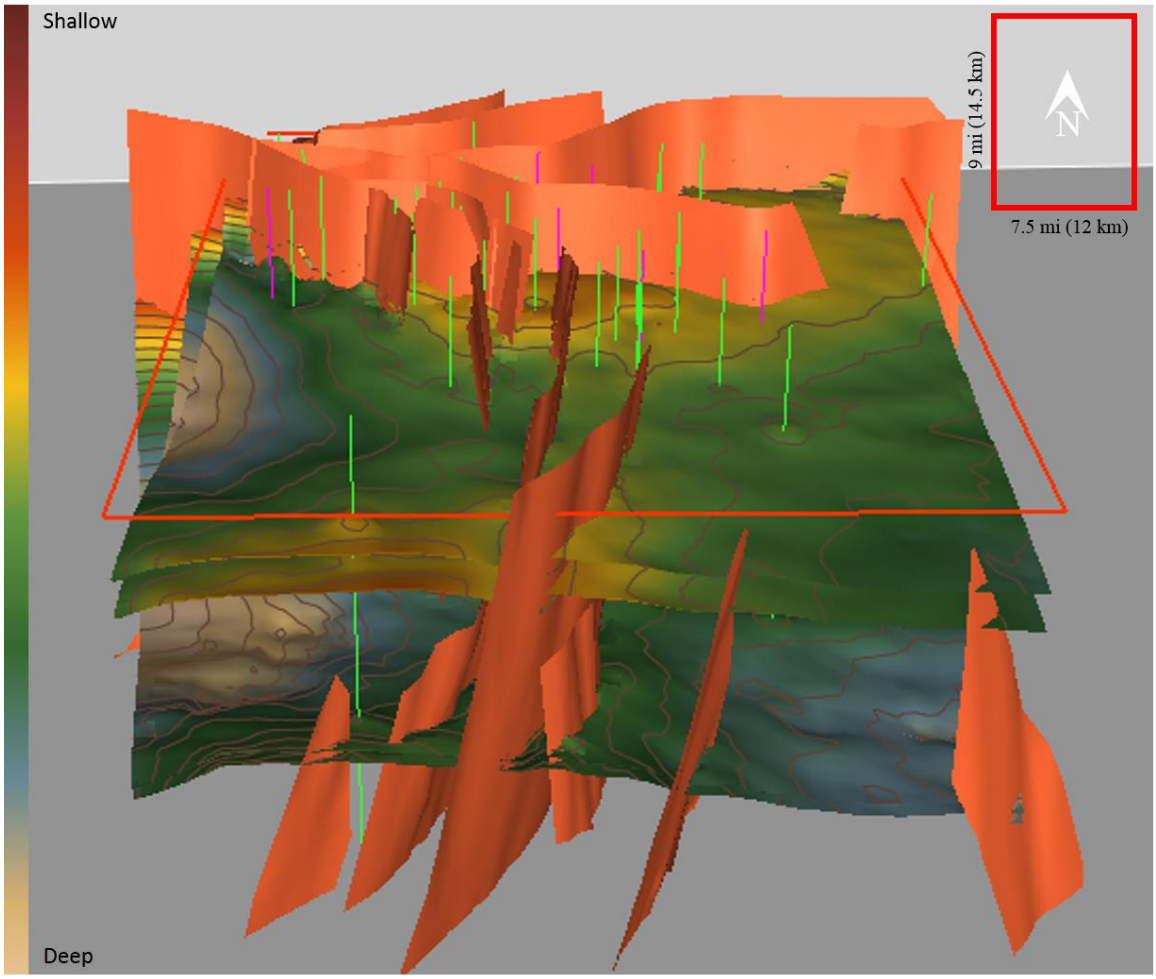

Figure 2.18: Stratigraphic framework data for the SIOI within the AOI (red outline, map view in upper right with dimensions). Four stratigraphic surfaces (Top *Amph* B Shale, Bot *Amph* B Shale, Bot SIOI, and MFS 10) are shown with faults in orange and wells in green/magenta.

Chapter 3: 3D Geocellular Modelling for the SIOI

3.1: INTRODUCTION

From interpreting surfaces on well logs to horizons and faults on 3D seismic, this defined stratigraphic framework (Chapter 2) accurately resembled the HI 24L Field. The next step was to properly create the geocellular grids for this project. A 3D geocellular grid is a three-dimensional volume that is divided into grid cells. The grid cells can hold any property value such as facies, porosity, permeability, and many others. A 30-million or a 500,000-cell 3D grid can be created using the same stratigraphic framework because it all depends on how fine or coarse the grid needs to be to mimic the field's geology, also being practical based on computing power and time. This chapter discusses how lithofacies and effective porosity were calculated in order to distribute the properties throughout the 3D geocellular grid and then to create the 3D property models. The workflow shown here is for the entire AOI, modeling the SIOI.

3.2 PETROPHYSICAL CALCULATIONS

To accurately model facies ("facies" is the nomenclature for the model, "lithofacies" refers to the property) and effective porosity for the HI 24L Field, petrophysical calculations had to be performed using well log data. Three log curves (only six wells had all three log curves) were utilized to accurately calculate lithofacies and effective porosity: SP (N=37), neutron porosity (N=6), and density porosity (N=6). Some wells only had a bulk density curve and thus had to be converted to density porosity using the appropriate formula (from Hartmann, 1999):

$$\phi_D = \frac{\rho_b - \rho_m}{\rho_f - \rho_m} \qquad (1)$$

where,

ρ_b = Bulk density (gram/cm^3)

ρ_m = Matrix density (quartz = 2.65 g/cc)

ρ_f = Fluid density (water = 1.0 g/cc)

The SP and two porosity curves were the most critical data points for this project to properly model facies and effective porosity.

Unlike in the previous chapter, three cutoff values were distinguished to differentiate three lithofacies (shale, shaly sand, and clean sand). The three lithofacies were chosen solely based on interpretation, using the author's understanding of clastic depositional environments similar to those interpreted in the study area. These cutoff values were 0.5 and 0.33, meaning that anything greater than or equal to 0.5 was considered a clean sand, between 0.5 and 0.33 was shaly sand, and less than or equal to 0.33 was shale. Figure 3.1 shows the workflow for generating a lithofacies curve, which is the primary curve for the facies model building process. A normalized SP curve (step 1) was used to pick the cutoff values for the three different lithofacies (step 2). Then the last step was to convert the log curve to a lithofacies curve (step 3). The lithofacies curve assigns a certain lithology one discrete value and in this case, 1 is clean sand, 2 is shaly sand, and 3 is shale. This curve looks blockier because of the three discrete values that were assigned to the three lithofacies, unlike the normalized SP curve with a continuous scale. As a result, a net to gross sand ratio of about 62% for the SIOI and the HC sand was calculated utilizing the lithofacies curve.

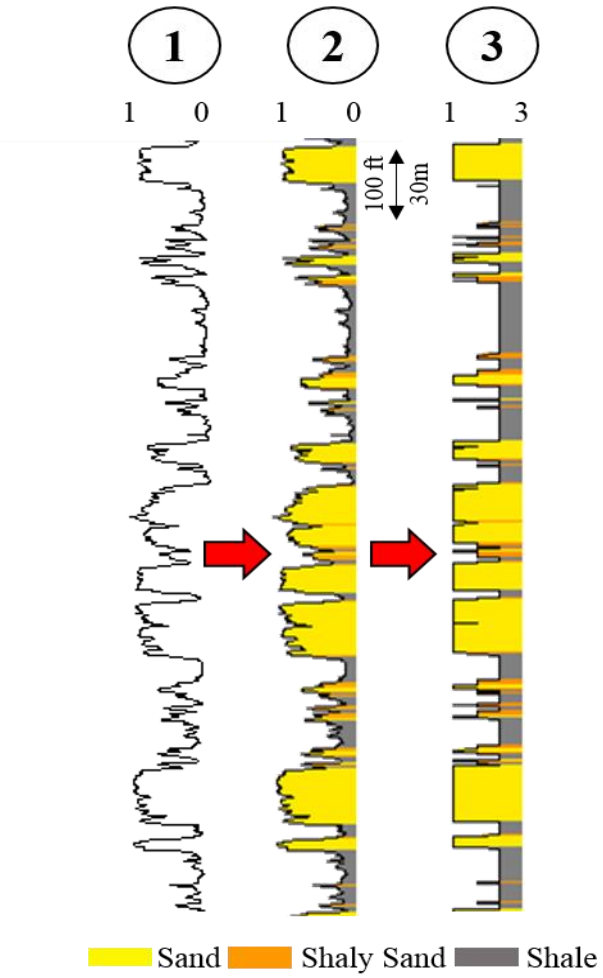

Figure 3.1: Method for converting SP log curve to lithology curve. First step normalizes SP curve. This is needed because different wells have different scales. Second step shows the three different lithofacies after picking two SP cutoff values. Third step is the discrete lithofacies assignment (curve) used as input for the 3D model.

For calculating effective porosity (EPHI), the volumetric percentage of shale had to be estimated to properly calculate the porosity for the sands in the formation as the porosity logs accounts for all the lithofacies present. For this study, the goal was to estimate the effective porosity of only sands in which CO_2 is assumed to be sequestered. The equation for EPHI (Marsan and Pratama, 2015) is:

$$\phi_E=\phi_T\ (1-V_{sh}) \qquad (2)$$

where,

ϕ_E = Effective porosity (EPHI)

ϕ_T = Total porosity (TPHI)

V_{sh} = Volumetric concentration of shale using normalized SP curve

Total porosity was then calculated using the following equation to remove any hydrocarbon effect (from Hartmann, 1999):

$$\phi_T=\sqrt{\frac{\phi_D{}^2+\phi_N{}^2}{2}} \qquad (3)$$

where,

ϕ_D = Density porosity

ϕ_N = Neutron porosity

All of the wells that were used to generate the facies model had an SP curve. To be consistent throughout this workflow, SP was the primary curve to differentiate lithology. Equations 4 and 5 were modified to reflect the SP curve even if they normally correspond to a Gamma Ray (GR) curve (Asquith et al., 2004). After normalizing the SP curves for all 37 wells, average values that represented the clean sand (0.85) and shale (0.2) baselines help calculate the SP shale index ratio by using the equation:

$$I_{sh}=\frac{SP-\ SP_{sand}}{SP_{shale}-SP_{sand}} \qquad (4)$$

where,

I_{sh} = Shale index ratio using normalized SP curve (unitless)

SP = Log value from normalized SP curve

SP_{sand} = Average normalized log value in clean sand (0.85)

SP_{shale} = Average normalized log value in shale (0.2)

A Tertiary non-linear correction was then applied to estimate the volumetric concentration of shale using the following equation (modified from Larionov, 1969):

$$V_{sh}=0.083\left(2^{3.71I_{sh}}-1\right) \qquad (5)$$

The average EPHI for the SIOI in a clean sand was calculated to be 33%, 17% in shaly sand, and 4% in shale. Similarly, the average EPHI for a clean sand in the HC Sand was 29% which aligns with Fowler et al.'s (1987) estimate. These values are important when modeling effective porosity throughout the 3D geocellular grid.

3.3: 3D GEOCELLULAR MODEL BUILDING

In order to create a 3D cellular grid, the framework that was constructed (see Chapter 2) was utilized to define the different intervals and grid boundaries. The following sections provide additional detail about how the SIOI 3D grid and property models were generated. The surfaces from top to bottom in the 3D grid were the Top *Amph* B Shale, Bot *Amph* B Shale, Bot SIOI, and MFS 10. With these four surfaces, the three intervals that were defined from top to bottom were the *Amph* B Shale, SIOI, and Underlying Shale.

3D Grid Construction

First, a regional grid for the AOI was created using cell sizes of 150 ft (46 m) x 150 ft (46 m), generating an approximately 30 million cell grid. The i-direction (similar to

seismic inline) had 265 cells, j-direction (similar to seismic crossline) 320 cells, and k-direction (similar to seismic time slice) 360 cells. The 360 cells in the k-direction represented the total number of layers in the vertical direction for the grid. Since all the surfaces from the framework were conformable to one another (not erosional), each cell layer was assigned a thickness to be proportional to the local interval thickness (Figure 3.2). The *Amph* B Shale interval is represented by 8 layers/cells, the SIOI by 350 layers, and 2 layers in the Underlying Shale. The reason 350 layers defined the SIOI was because the average thickness was about 1720 ft (525 m) and the smallest shale layer thickness that aimed to be resolved between the sands in the SIOI was 10 ft (3 m). To fully capture these interlayered shales at this scale, an average layer thickness of half of the smallest resolvable shale was determined (5 ft; ~2 m). Rounding up the quotient of 1720 (525 m) by 5 ft (~2 m), 350 layers of the 360 layers in the grid represented the SIOI (Table 3.1).

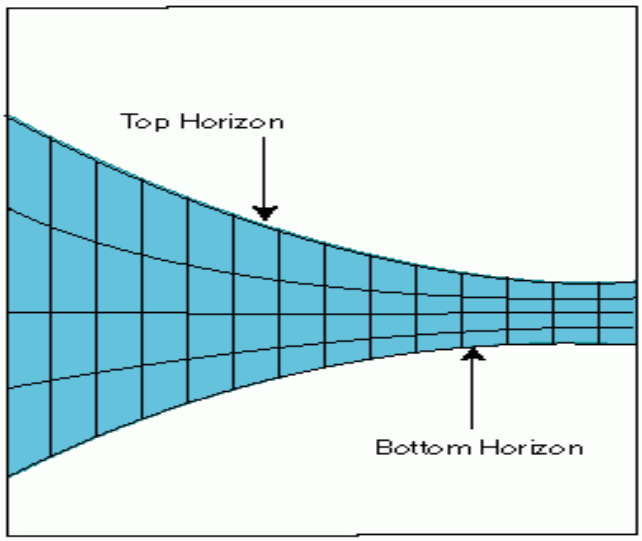

Figure 3.2: Definition of proportional layering (from Halliburton).

Interval #	Interval Name	Top Surface	Bottom Surface	# of Layers	Layer Thickness (ft,m)
1	*Amph B* Shale	Top *Amph* B Shale	Bot *Amph* B Shale	8	51 (~16)
2	SIOI	Bot *Amph* B Shale	Bot SIOI	350	5 (~2)
3	Underlying Shale	Bot SIOI	MFS 10	2	70 (~21)

Table 3.1: SIOI 3D grid parameters and properties. Three intervals define the grid, with 360 total proportional layers.

Property Upscaling (well logs and 3D volumes)

All properties needed to create the 3D facies and effective porosity models had to be upscaled based on where the property intersected the 3D grid. Upscaling here means that the values from a log curve (lithofacies or EPHI) or 3D volume were attached or scaled up to the 3D cellular grid, giving the grid cells that the property intersected those appropriate values. Two 3D volumes and two well log curves (lithofacies and EPHI) were upscaled to the 3D grid. One of the 3D volumes was a nonlinear neural network volume that was created by Dr. Ye Feng (post-doc at BEG) by using multi-attribute analysis that calculated the best fit between porosity logs and a combination of seismic attributes at these well locations. A probabilistic neural network (PNN) was then applied to investigate the nonlinear transform that predicted a higher resolution porosity volume with finer details. These methods are described in detail by Feng in a separate manuscript (in preparation). The second 3D volume was a root mean squared (RMS) extraction volume of the original seismic amplitude 3D volume. The RMS 3D volume enhanced the strong amplitude zones to interpret the lithofacies present.

All data except the lithofacies curve were upscaled using an averaging method meaning that all the values that occupied one particular grid cell were averaged to then assign the grid cell that value. The method for the lithofacies curve assigned the grid cell the dominant lithofacies value because the property had discrete values. The result of upscaling the log curves also clipped them to the dimensions of the grid. On the other hand, the RMS amplitude volume resembled a 3D volume respective to the dimensions of the 3D grid when upscaled using the averaging method. (Figure 3.3). Upscaling the lithofacies and EPHI curves enabled the properties to be distributed and modeled throughout the 3D grid whereas the RMS amplitude and the nonlinear, neural network porosity volume were

utilized to have better control and calibration with the facies and effective porosity model, respectively.

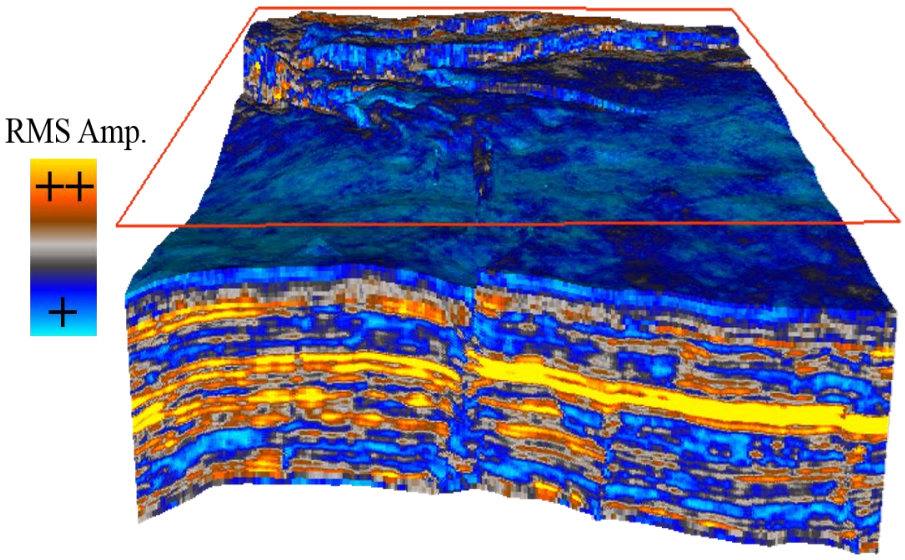

Figure 3.3: Upscaled RMS amplitude volume to the 3D grid. The upscaled RMS amplitude resembles a small volume based on the dimensions of the grid.

3.4: PROPERTY MODELING

Introduction

To create a model with continuous properties, the properties that were upscaled to the 3D grid at the well log locations had to be distributed horizontally and vertically throughout the remaining unpopulated grid volume. Geostatistical techniques were utilized to distribute the properties. Vertical and omni-directional variograms were generated based on the property of interest (lithofacies or EPHI) to then be used to interpolate through the model volume. A variogram model is a common tool to measure spatial correlation for properties such as facies, porosity, and permeability to define how similar two adjacent points are to each other. Continuity in the horizontal direction is usually more than in the vertical direction for geologic bodies, which is why variograms are rarely isotropic (Pyrcz and Deutsch, 2014).

Different terms define and characterize a variogram. Since the bulk of this study is not about geostatistics, the main points to know are how a variogram model can be interpreted and what the sill, range, nugget, horizontal distance, and vertical distance represent (Figure 3.4). The sill is defined as when the empirical variogram appears to level off as points above it indicate negative spatial correlation while points below indicate positive correlation. The range is the distance at which the variogram reaches the sill and any points that are farther apart only have a random relationship. The nugget (nugget effect) relates to the discontinuity at the origin of the variogram. (Bohling, 2005). Here the nugget is zero for all cases because sedimentary environments are locally continuous (Pyrcz and Deutsch, 2014). The horizontal and vertical distance represents the range according to their corresponding variogram, thus anything larger is no longer correlated. Some variogram

models can also experience cyclicity in the vertical direction because different patterns over small distances are recognized, as seen in the SIOI.

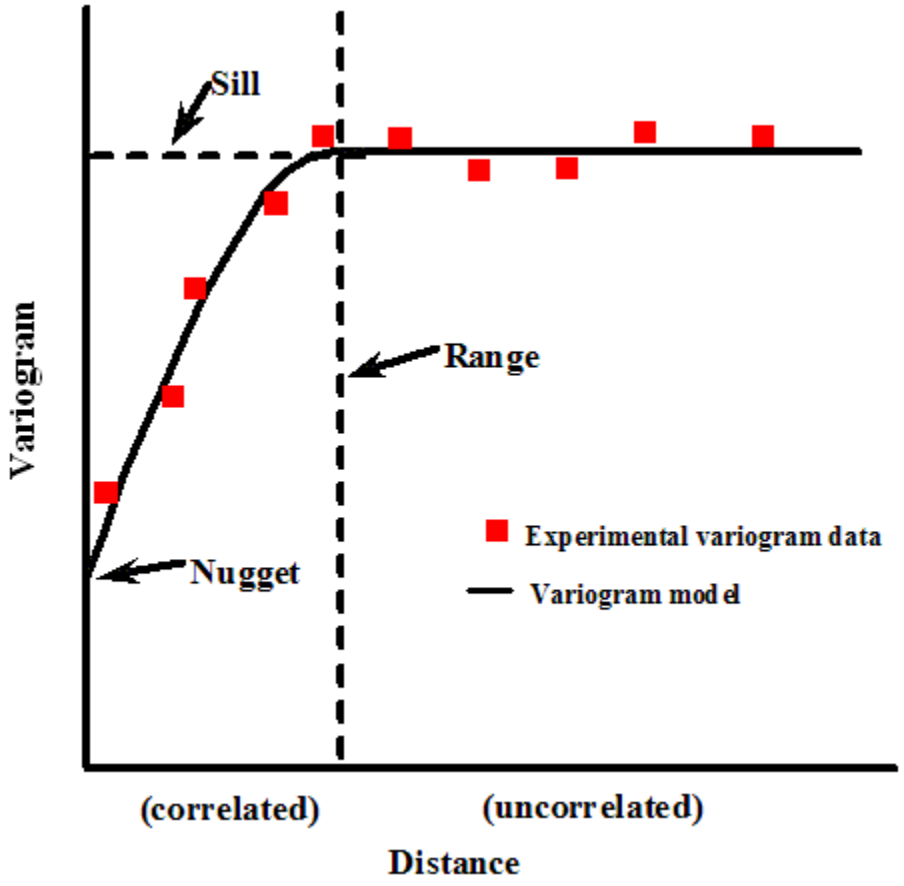

Figure 3.4: Variogram model that identifies the key components: sill, range, and nugget. The y-axis is the variance, showing the degree of difference between pairs of points. The x-axis is separation distance between the points. (From website: https://vsp.pnnl.gov/help/vsample/Kriging_Variogram_Model.htm)

Facies Modeling

The facies models that were generated for both the SIOI and HC Sand grid used a stochastic cell-based facies modeling algorithm widely known as Sequential Indicator Simulation (SIS; Pyrcz and Deutsch, 2014). It generates multiple equally probable realizations of a property by building up a discrete cumulative density function (CDF) for the individual categories in each ease. SIS works well when geometries of reservoirs are unknown, unlike the case with channels or delta lobes, to generate a preliminary facies model (Halliburton). The required inputs for the simulation are: an upscaled lithofacies curve (1=shale, 2=shaly sand, 3=sand), a defined variogram, and a background trend that can be honored.

The background trend was crucial for the facies model because it added a second element that utilizes a probability of occurrence methodology of each lithofacies at each grid cell in the 3D grid. The higher the probability of the lithofacies corresponding to the background trend yields a higher likelihood of giving that specific grid cell the lithofacies value. Since 3D seismic data were available, a calibration with the facies to the upscaled RMS amplitude volume (Figure 3.3) acted as the background trend. Strong amplitude reflectors were interpreted as high-porosity zones, which is more characteristic of sands than shales. This is why generally, high-amplitude zones represent sandy units (Brown, 2011). Then for each interval in the model (*Amph* B Shale, SIOI, Underlying Shale), a variogram model was created based on the dominant lithofacies present in each interval using the upscaled lithofacies curve (e.g., sand for the SIOI). For the SIOI, the range for both the vertical and omni-directional variogram was about 45 ft (14 m) and 3400 ft (1040 m), respectively (Figure 3.5). The omni-directional variogram accounts for all azimuths in the XY (horizontal) plane. These range values agree with Pyrcz and Deutsch (2014) with the horizontal plane having ~75 times longer continuity of geologic bodies than in the

vertical direction. The vertical direction variogram also experiences cyclicity because of the sand/shale pattern (as seen in well logs) in the SIOI.

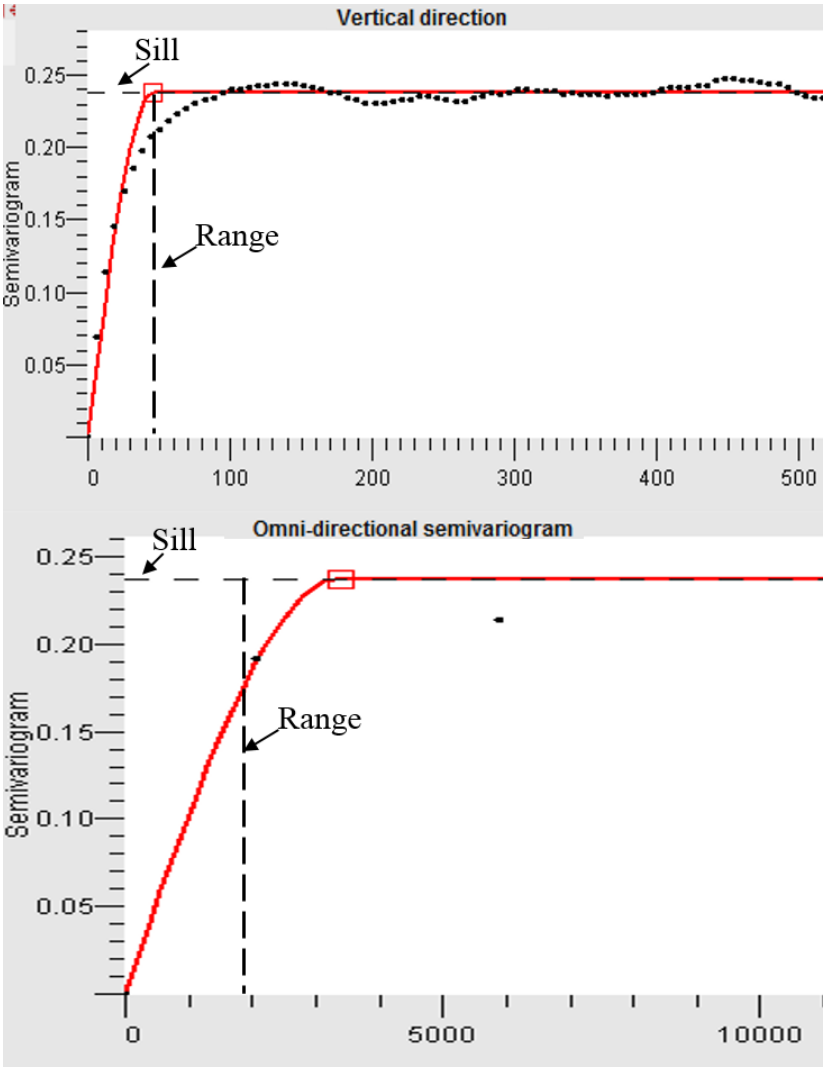

Figure 3.5: Variogram model corresponding to the sandstones in the SIOI. Note the cyclicity in the vertical variogram, due to the shale/sand stacking pattern as seen in well logs. The range and sill are delineated in both the vertical and omni-directional variograms.

The SIS workflow was then executed after calculating an experimental variogram for each interval and calibrating the lithofacies in the SIOI to the upscaled RMS amplitude property. Since this simulation stochastically generates equiprobable models, 10 realizations were created. Multiple realizations can help evaluate uncertainty, but in this case it was primarily used to generate a suite of models for calculating the CO_2 storage capacity. Figure 3.6 shows an i,j, and k plane of one of the 10 facies model iterations. The k plane shows a surface/layer that is near the bottom of the SIOI, and gaps on the section represent faults. In all 10 realizations, the *Amph* B Shale and the SIOI can be distinguished. The overall objective was to make sure all realizations represented the geology accurately because all realizations were subsequently used to calculate CO_2 storage capacity. The main goal was to make sure the SIOI was represented as primarily sand with semi-continuous interlayered shale and that the *Amph* B Shale was represented as dominantly shale. Sands and shaly sands were present in the *Amph* B Shale because the entire package was not interpreted to be all shale, as the well logs show (see Chapter 2). The methodology utilized to generate the facies models interprets these sands and shaly sands. However, these higher porosity lithofacies within the top seal are small (~10 ft, 3 m thick) as they are assumed to have no effect on CO_2 storage for this study. A proper analysis of how the sands and shaly sands correlate within the *Amph* B Shale is recommended.

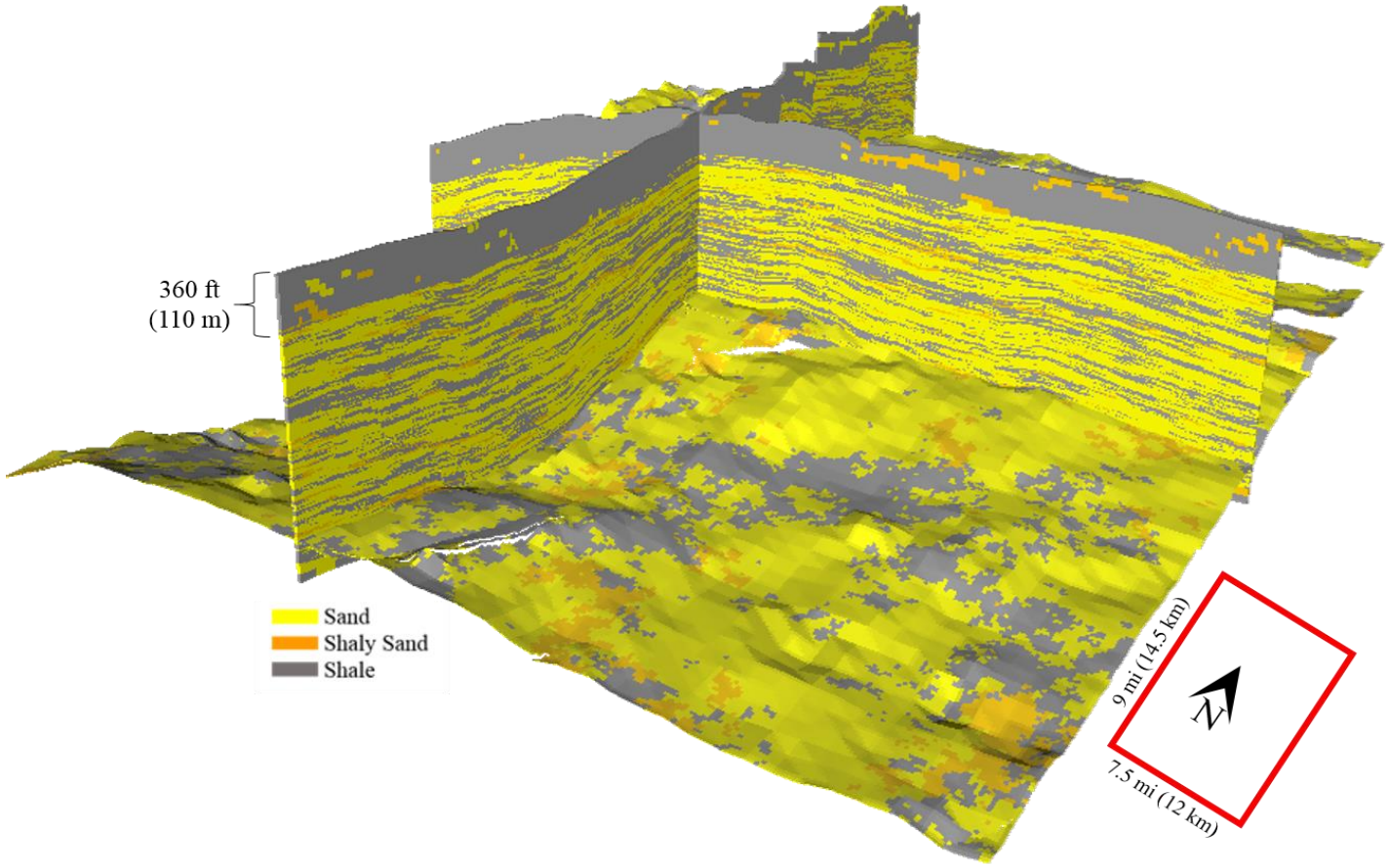

Figure 3.6: I, j, and k plane of the 3D facies model. The k plane is layer number 320 (top to bottom). The property is discrete, meaning each grid cell has only 1 of 3 values.

Effective Porosity Modeling

The effective porosity model was generated with a 3D simulation algorithm called Turning Bands. This algorithm is appropriate for continuous properties such as porosity and permeability that is performed by kriging and creating unconditional simulations. The simulation is done in one dimension along lines (bands) intersecting the 3D grid (Halliburton). Turning Bands differs from the SIS workflow because SIS utilized discrete properties. Generally, the variogram model set as the input should be consistent or similar to the facies model, but in this case it was not because the effective porosity variogram was calculated based on the non-linear porosity volume. The nonlinear neural network porosity volume was calculated based on the sample rate of the 3D seismic (4 ms), which equates to about 75 ft (23 m), not fine enough to model the SIOI vertically, unlike the EPHI log curve. Therefore, the upscaled nonlinear neural network porosity model was utilized to compute the omni-directional horizontal variogram whereas the EPHI curve was used for the vertical. The strength in the seismically derived porosity volume was the continuity in the XY direction. The vertical and omni-directional distances that represented the range were about 20 ft (6 m) and 27,000 ft (8230 m), respectively. The long horizontal distance was justified by correlating the sand bodies within the SIOI to another field (HI 10L) which can be seen in Ramirez Garcia's thesis (2019).

After calculating the variograms, the effective porosity model was constrained by the facies model with all 10 realizations generated. The variogram was only used for the *Amph* B Shale and SIOI because not enough data points for sand or shaly shale were present in the Underlying Shale interval. Constant average values of 0.33 and 0.17 were used, respectively. Five realizations were then produced for each facies model, resulting in a total of 50 effective porosity realizations (Figure 3.7). Figure 3.8 shows one porosity realization of the facies model seen in Figure 3.6. When comparing the effective porosity model to the

facies model, the general pattern or geometry of the stratigraphy was similar because effective porosity was modeled based on the lithofacies. A clean sand in this study should have higher porosity than a shaly sand or shale, as shown by the workflow and output of both these models.

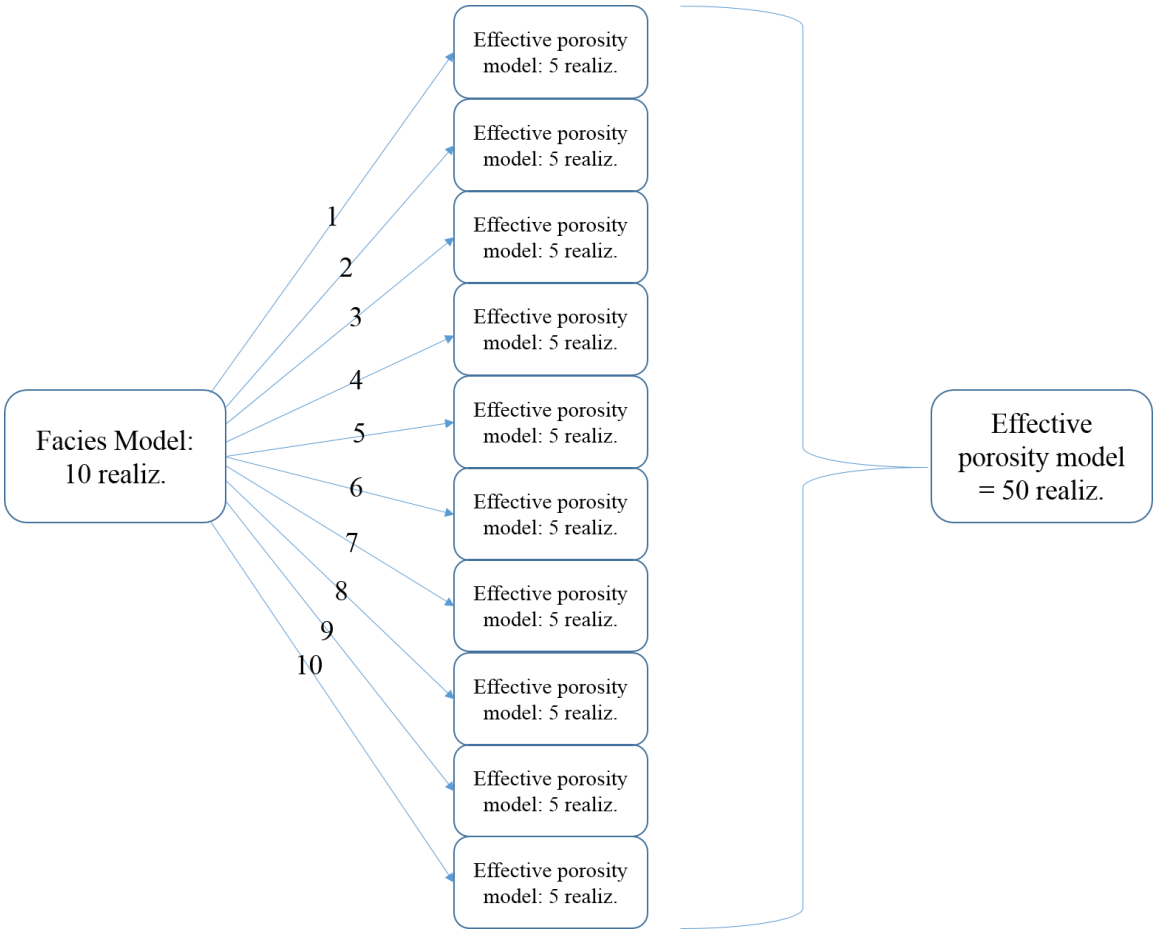

Figure 3.7: Workflow to generate 50 effective porosity realizations.

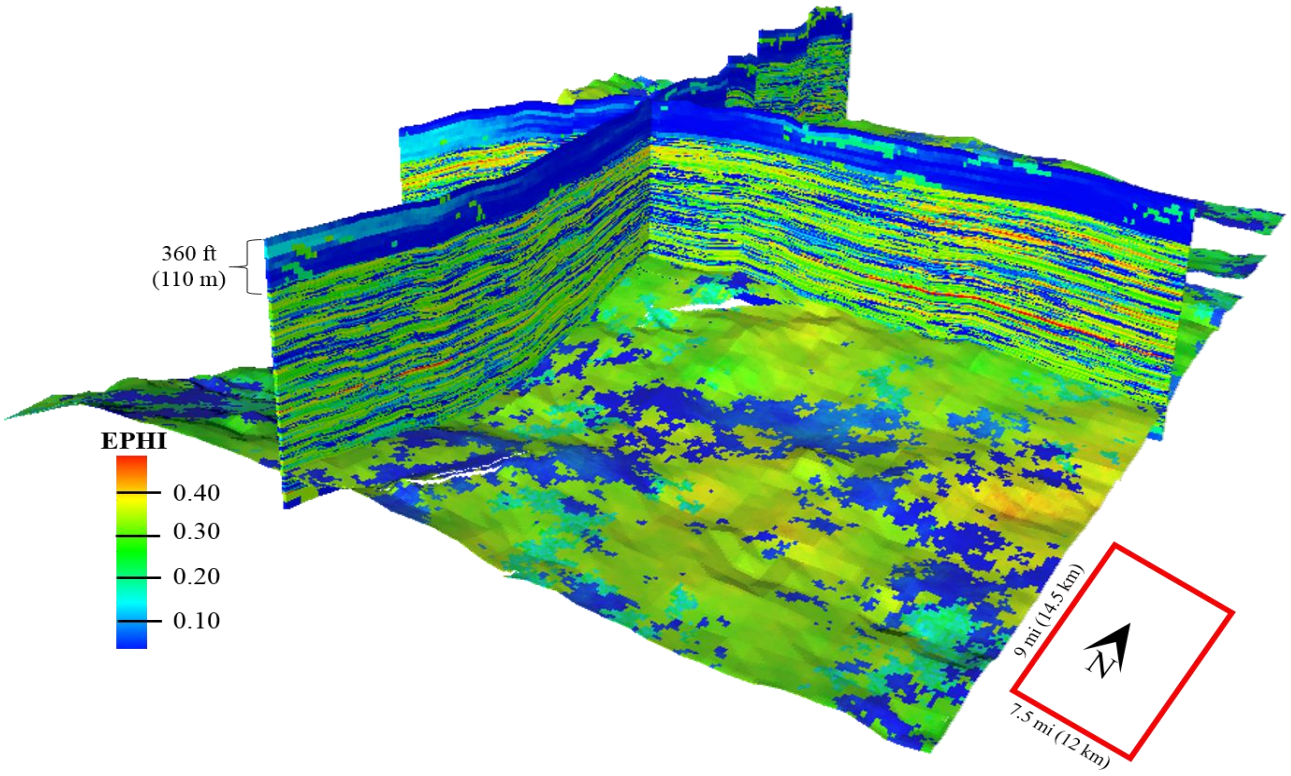

Figure 3.8: I, j, and k plane of the 3D effective porosity model. The model was created using the upscaled nonlinear neural network porosity volume as a secondary reference property. Unlike the facies model, the effective porosity represents continuous values. The k plane is layer number 320 (top to bottom).

Chapter 4: CO_2 Storage Capacity Analysis

4.1: INTRODUCTION

CO_2 storage capacity assessments have been conducted regionally for the entire TexLa 3D survey (Wallace et al., 2014). This chapter calculates the storage potential of the HI 24L Field at a more CCS project scale within two different packages after building the stratigraphic framework. The interpretation of the hydrocarbon footprint for the HC Sand allowed interpretation of the structural closure footprint for the SIOI, a main factor in estimating the storage capacity for both packages correctly. Four methodologies were then utilized to estimate the CO_2 storage capacity in both the SIOI and HC Sand. Each calculation was dependent on the efficiency factor. Despite a lack of productive hydrocarbons in the SIOI, the goal was to determine the key factors that influenced each method to then evaluate its accuracy. The main motivation was related to the known trapped hydrocarbon volumes that can then be associated with the estimated CO_2 storage capacity. To compare the storage capacity estimates, a simplified storage system composed of a single sand body was assumed, specifically for the SIOI.

4.2: HYDROCARBON/STRUCTURAL FOOTPRINTS

Two previous studies characterized the HI 24L Field using 2-D (Fowler et al., 1987) and 3D seismic data (Brown, 2004) and both included structure maps of the HC Sand, the most productive hydrocarbon reservoir in the field. Brown (2004) delineates gas-water contacts within his structure map (Figure 4.1) of the HC Sand, which correlates well with the RMS amplitude map extracted from the interpreted HC Sand horizon in this study (Figure 4.2). RMS amplitude maps help locate strong acoustic impedance contrasts, potentially identifying the type of lithology present (sand vs shale) and usually areas where the reservoir was charged with hydrocarbons (Brown, 2011). Figure 4.1 and 4.2

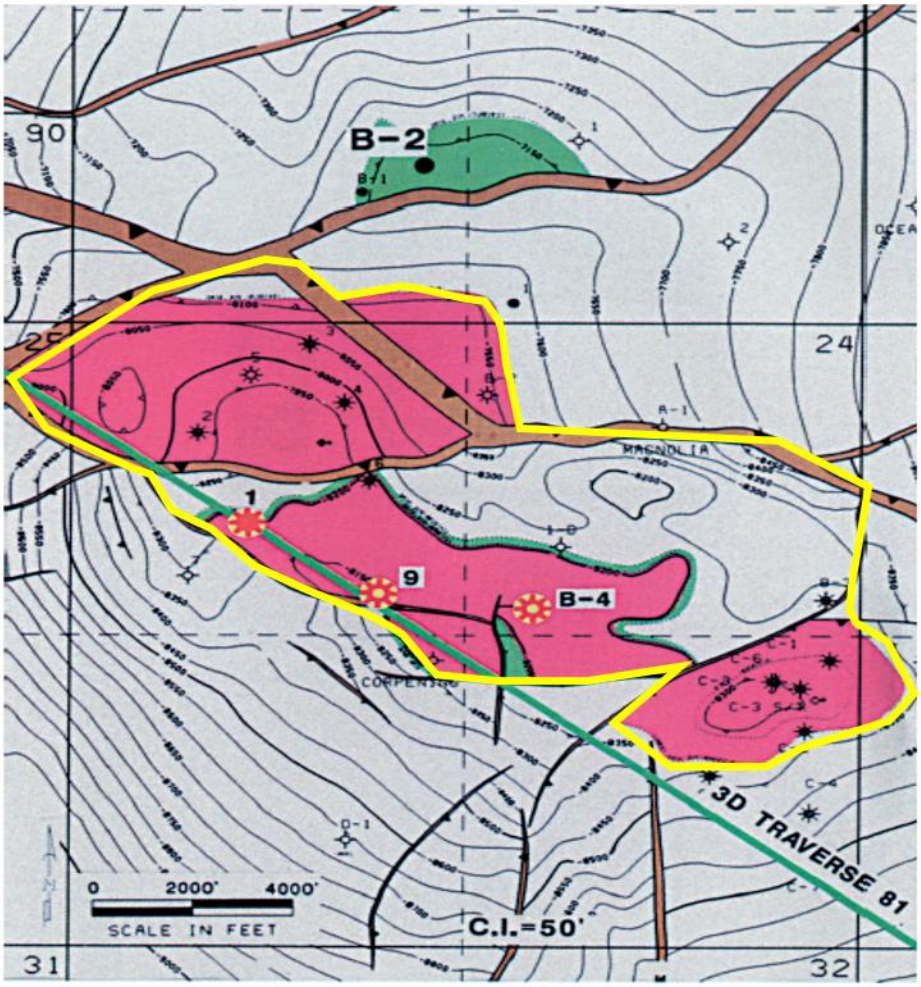

Figure 4.1: Structure map of HC Sand from Brown (2004). Brown's interpretation of gas (pink) and oil (green) distribution is compared to the hydrocarbon footprint interpreted in this study using 3D seismic amplitude information (yellow polygon).

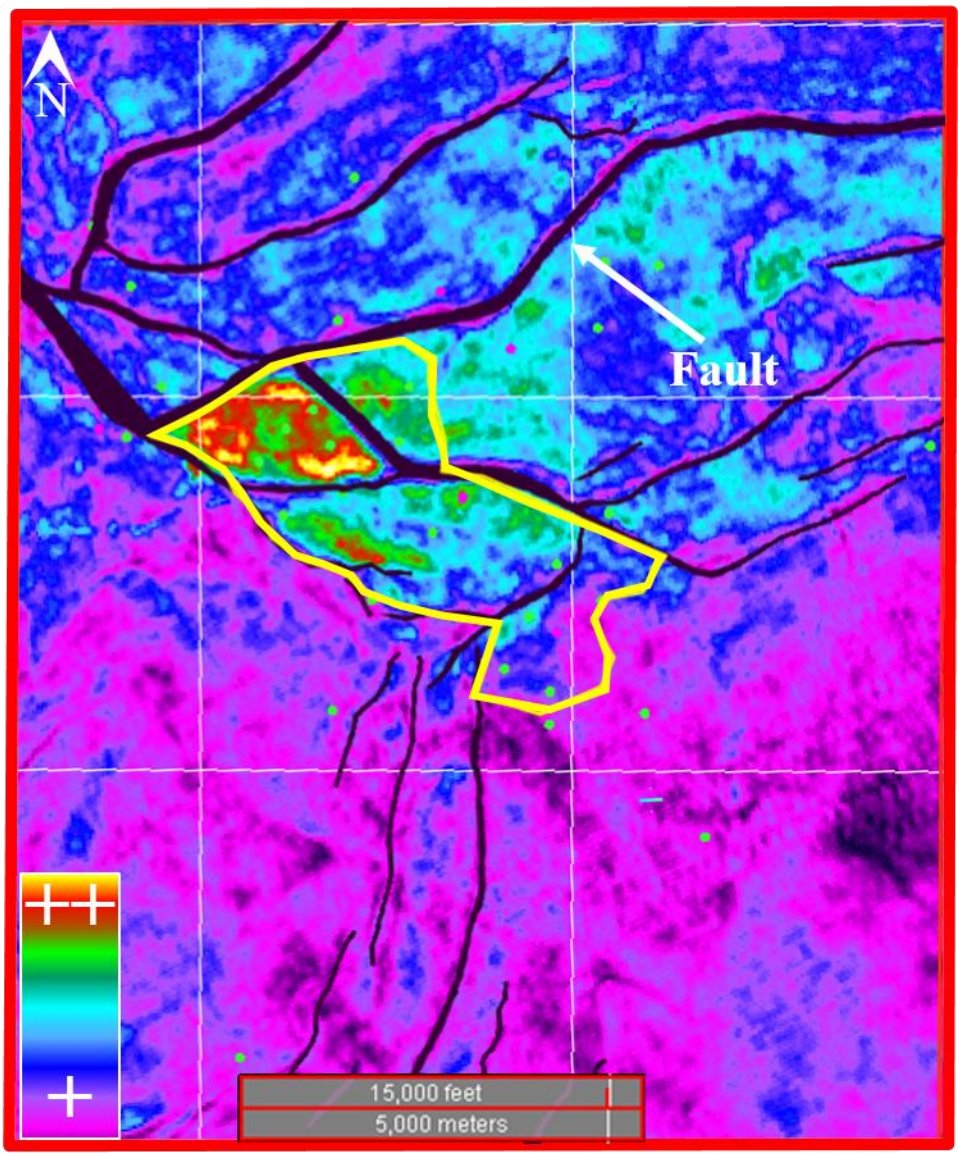

Figure 4.2: RMS amplitude map of HC Sand showing the interpreted hydrocarbon footprint (map distribution) within the yellow polygon, similar to Figure 4.1. Bright colors represent high amplitude values, cool colors are low values. Black polygons represent faults.

have the interpreted hydrocarbon footprint outlined (in yellow) for the HC Sand. The oil area around well B-2 (Figure 4.1) was not accounted for because only natural gas production was considered. Interpretation of the hydrocarbon footprint for the HC Sand was optimistic because it covered more area than the gas-water contacts. Depending on *Amph* B Shale properties (not currently sampled), the expected CO_2 column height within the SIOI, and therefore the CO_2 capacity footprint, in this structural setting is unknown. Therefore, the footprint is assumed to be similar to the charged area of the HC Sand (Figure 4.3). For the SIOI, a conservative CO_2 structural footprint was determined using the Bot SIOI structure map (Figure 4.3b). The SIOI footprint area is essentially identical in map extent to the charged area of the HC Sand (3,275 acres; 13 sq. km.). The general assumption behind the CO_2 storage capacity estimate was that the net sand for the thick package can be utilized in this structural footprint area for CO_2 sequestration because of confidence in the ability to trap fluids in a reservoir below the SIOI (HC Sand). This was an important assumption for constraining CO_2 capacity estimates of both the HC Sand and the SIOI.

Having both HC Sand and SIOI footprints interpreted, a second 3D grid was created following the same workflow outlined in Chapter 3, now for a much smaller area. Figure 4.4 shows a 2D schematic and Figure 4.5 the 3D grid of the structural footprint for the SIOI related to the AOI to depict how the grid parameters for the footprint area compared to the AOI. In both cases, 350 proportional layers still characterized the SIOI, even though the numbers of cells were significantly different. This 3D grid for the footprint area was utilized to estimate the storage capacity for the SIOI, following the same workflow that was used with the HC Sand.

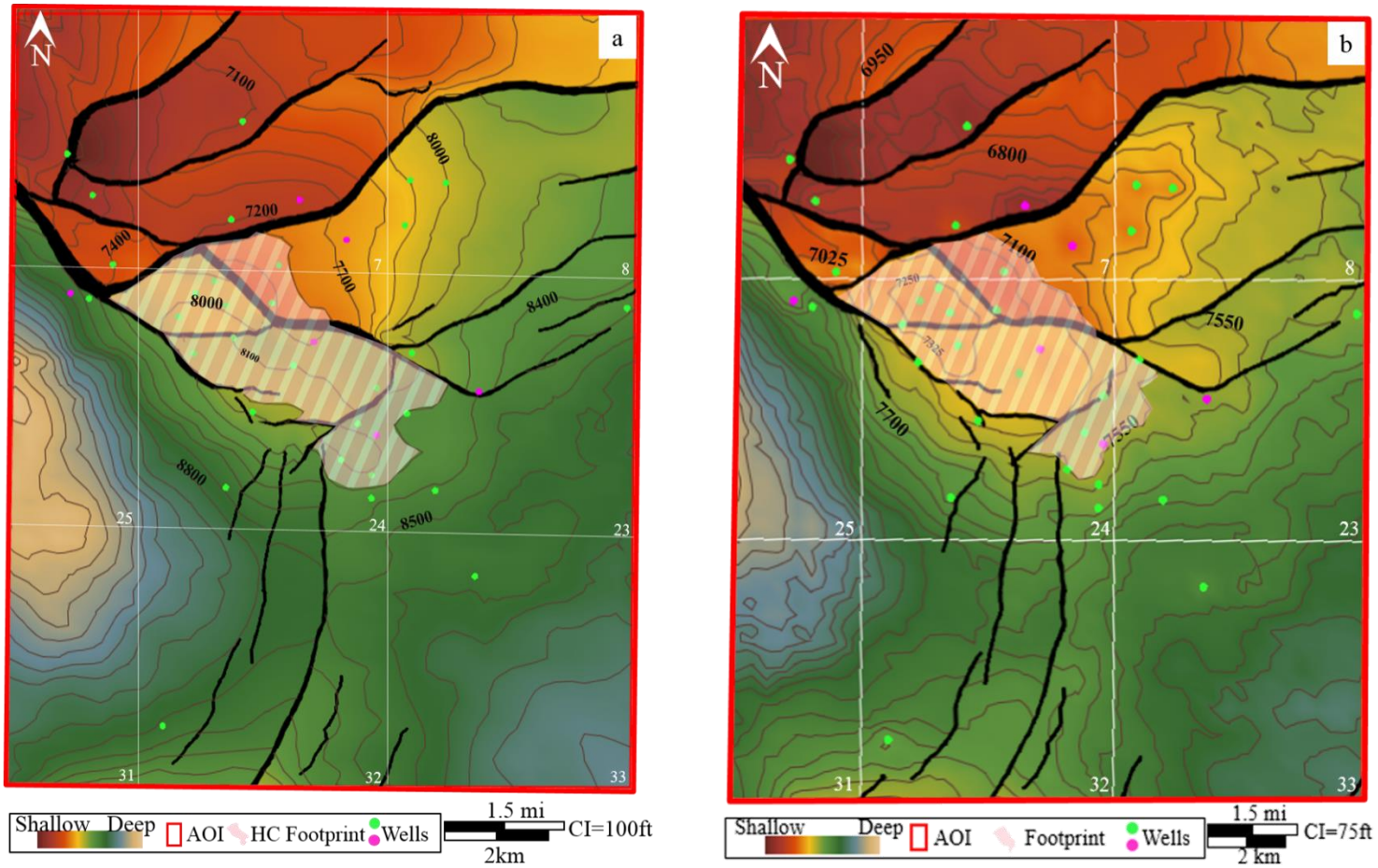

Figure 4.3: Structure map of the top of (a) HC Sand reservoir and (b) Bot SIOI horizon. See Fig. 2.3 for stratigraphic column. Footprint of the seismically interpreted (RMS) hydrocarbon footprint for the HC Sand and the assumed structural footprint for the SIOI is shown in white striped polygon. Lease block numbers are labeled.

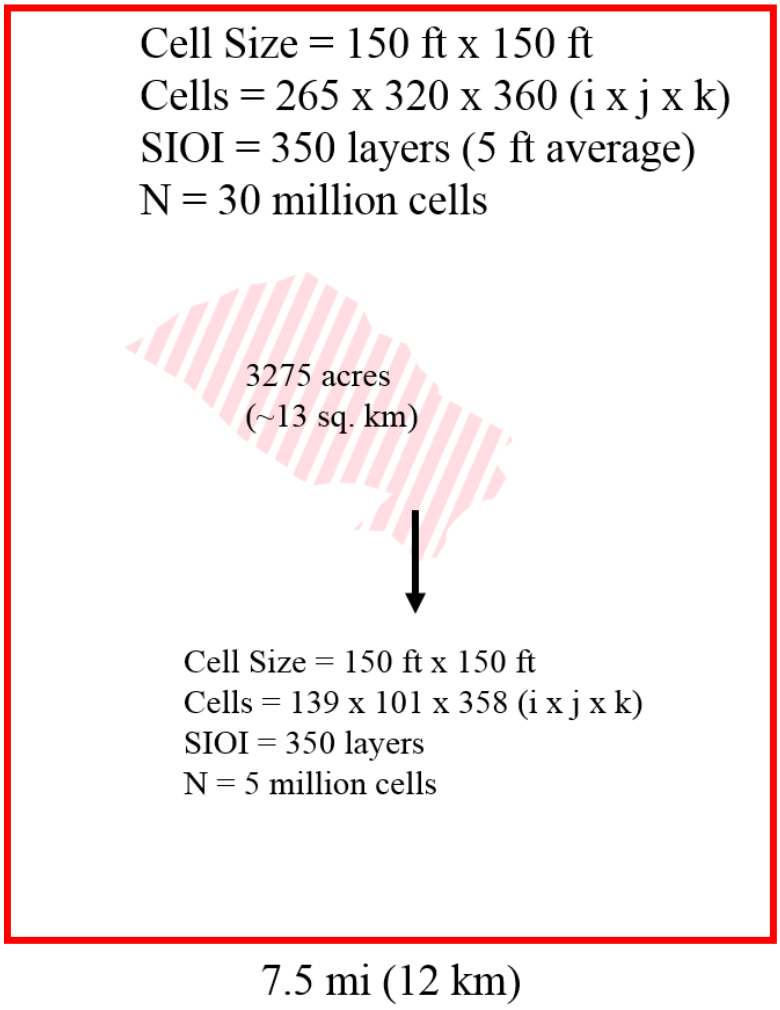

Figure 4.4: 3D grid size of the SIOI structural closure footprint relative to the AOI. In each grid, the SIOI is characterized by 350 proportional layers. The grid generated for the footprint area was utilized to estimate storage capacity.

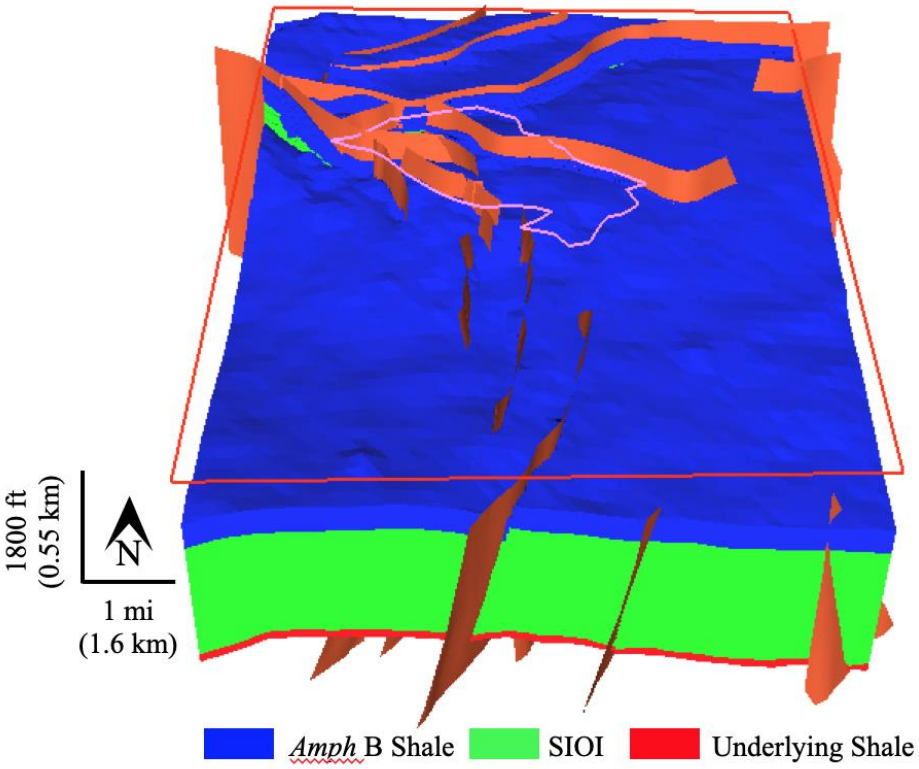

Figure 4.5: SIOI 3D grid of the AOI showing the three different intervals. Faults are in orange, AOI is outlined in red, and the SIOI structural closure footprint is in pink.

4.3: HC Sand CO_2 Storage Capacity

The HC Sand (200 ft thick; 60 m) was more confidently analyzed than the SIOI because of historic production data and previous literature. Therefore, this chapter describes the results for the HC Sand first. The stratigraphic chart and type log are shown again in Figure 4.6. Two intervals were modeled to calculate the storage capacity for the HC Sand: the top seal (MFS10 to Top HC Sand surface) and the HC Sand (Top HC Sand to Bot HC Sand surface). The storage capacity was calculated for the HC Sand within a subset of the AOI of approximately 3300 acres (13 sq. km), restricted to the interpreted hydrocarbon footprint area for the HC Sand.

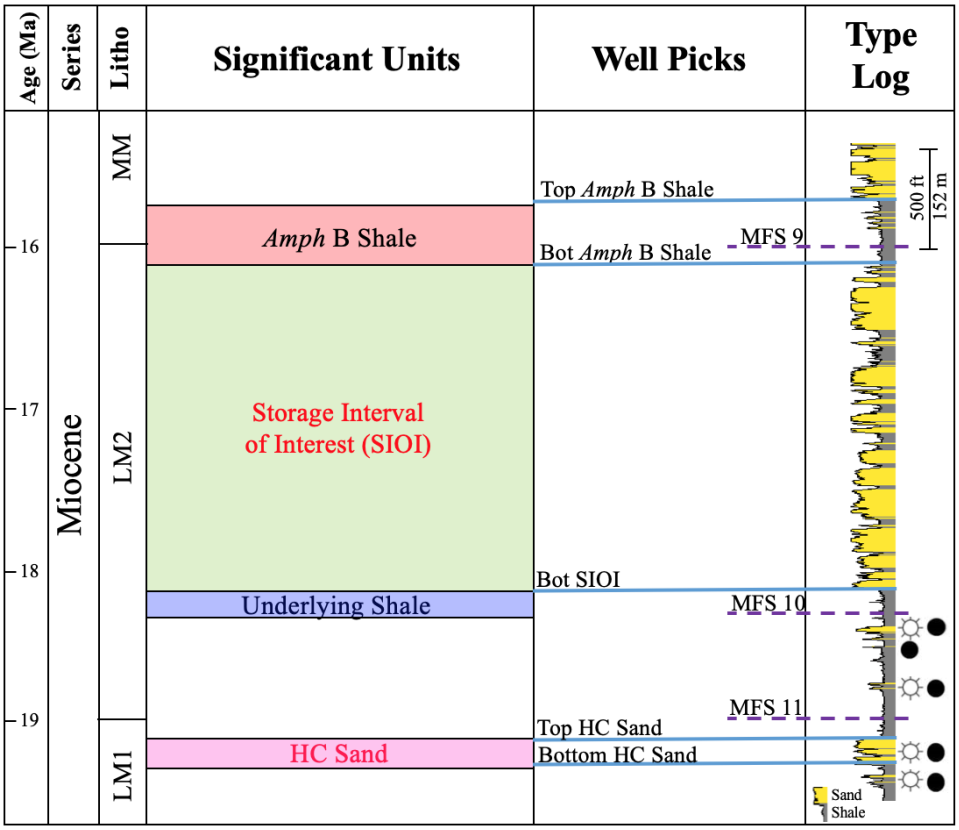

Figure 4.6: Stratigraphic chart and type log of High Island 24L.

The 13 square mile 3D grid that was created for the HC Sand's hydrocarbon footprint was less than 300,000 cells (146x107x18), with horizontal grid dimensions of 150x150 ft (46x46 m). The top seal was defined by 8 proportional layers (75 ft; 23 m each) and the HC Sand with 10 proportional layers (20 ft; 6 m; Table 4.1). Similar to the SIOI facies model workflow, a variogram model using the lithofacies curve as the input data was calculated. The model was then calibrated to the upscaled RMS seismic volume to generate 10 realizations of the facies model. The vertical distance for the range of the variogram was calculated to be 220 ft (67 m) and 25,000 ft (7600 m) for the horizontal omni-direction. The effective porosity model was generated differently because the nonlinear, neural network porosity volume did not include the HC Sand. Instead, each facies was assigned a constant EPHI value for all 10 realizations: 0.035 for shale, 0.15 for shaly sand, and 0.29 for clean sand. These averaged values were derived from the 6 EPHI curves after upscaling. Both the facies and effective porosity models can be seen in Figure 4.7. A sense of how significant the fault offset is can be visualized in Figure 4.1, where offsets are as much as 550 ft (168 m), juxtaposing the HC Sand against shale. The juxtaposition of material across faults becomes important for the lateral trapping of fluids, a topic that is discussed further at the end of this chapter.

Interval #	Interval Name	Top Surface	Bottom Surface	# of Layers	Layer Thickness
1	Top Seal	MFS 10	Top HC Sand	8	75 ft (23 m)
2	HC Sand	Top HC Sand	Bot HC Sand	10	20 ft (6 m)

Table 4.1: HC Sand 3D grid parameters and properties. Two intervals define the grid, with 18 total proportional layers.

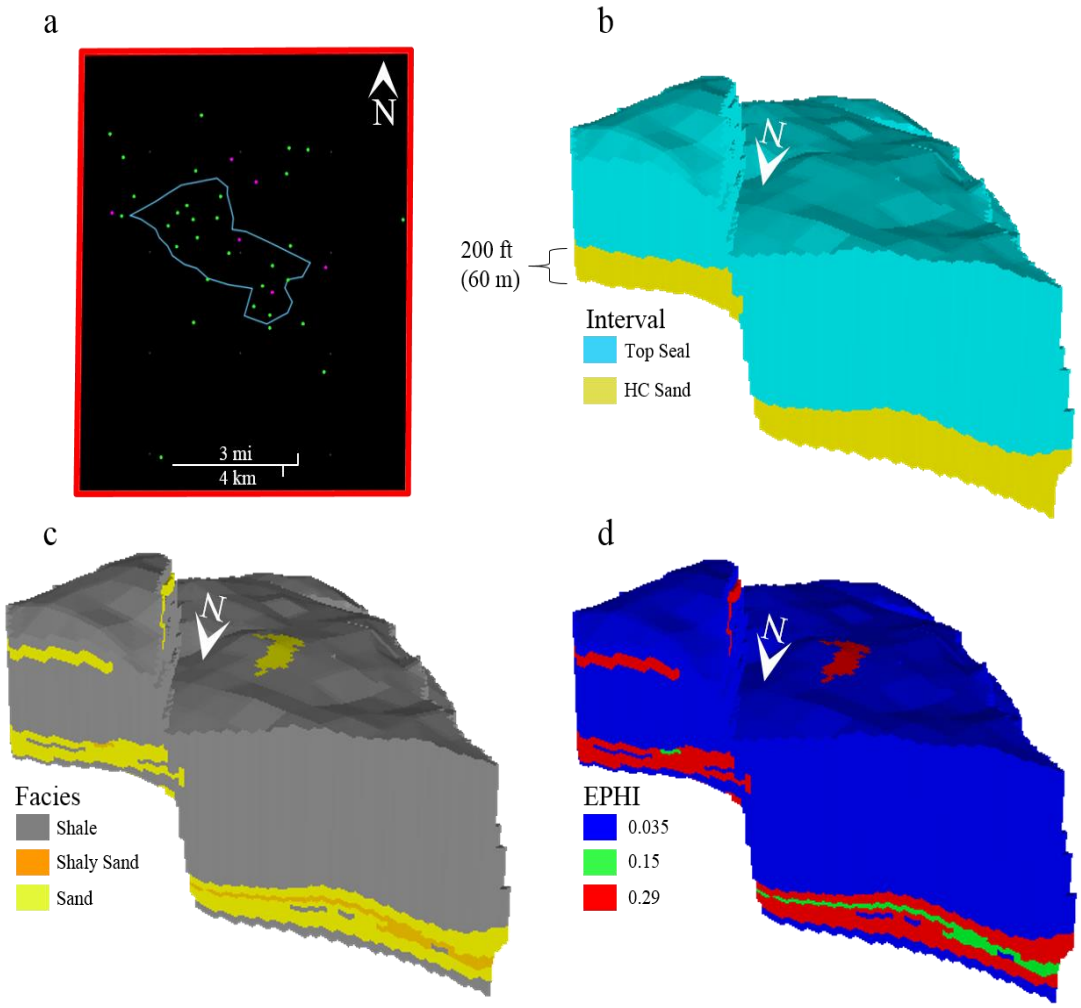

Figure 4.7: HC Sand 3D models. (a) Map view of the hydrocarbon footprint (light blue) and the AOI (red) with wells (color scheme as before). Parts (b), (c), and (d) illustrate the interval, facies, and effective porosity models from the grid, respectively.

3D Geocellular Models Methodology

The first methodology to statically estimate CO_2 storage capacity was utilizing the 3D geocellular models. For the HC Sand, all 10 realizations of the facies and effective porosity models were used to calculate 10 unique net pore volumes (NPV) within the HC Sand reservoir. The gas-water contact is assumed to be the CO_2-water contact at the intersection of the bottom HC Sand structure of the hydrocarbon footprint defined previously. The assigned net-to-gross sand proportion (NTG) values assigned to the three facies were: 0 for shale, 0.15 for shaly sand, and 1 for sand (Table 4.2). These assignments mean that no shales and only 15% of the shaly sands are accounted for when calculating the net pore volume after including all clean sands. The calculated static NPV for all 10 realizations were used to calculate the associated stored CO_2 mass. The following sections present the equations and assumptions made in the CO_2 storage capacity calculations.

Facies	NTG
Shale	0
Shaly Sand	0.15
Sand	1

Table 4.2: Net-to-gross sand (NTG) values set for the three lithofacies.

The Goodman et al. (2011) methodology was developed for regional (thousand sq. mi/sq. km) capacity assessment, but is still applicable for a field-scale (10 sq. mi/sq. km) assessment (such as the HI 24L Field) that utilizes more detailed, site-specific geologic interpretations. The equation used in this methodology corresponds to a saline aquifer, assuming that hydrocarbons were never present in the HC Sand. This is the main assumption made throughout the study because further work has to be done to properly consider the immovable hydrocarbons and the vertical leakage pathways via the wells drilled if CO_2 were to be injected. The storage capacity equation corresponding to the 3D geocellular models is:

$$G_{CO2} = A_n \, h_{ntg} \, \Phi_{eff} \, \rho \, E_{saline} \qquad (6)$$

Units are kg, where 1 metric ton (tonne) = 1000 kg, and 1 Mt = 10^6 metric tons.

where,

A_n = Net area (m^2; assumed to be the historic HC Sand hydrocarbon footprint area)

h_{ntg} = HC Sand net sand thickness (m, similar sense to Wallace et al., 2014)

Φ_{eff} = Effective porosity (unitless, fraction of total porosity assumed to be capable of transmitting fluids; interconnected pores)

ρ = CO_2 density (kg/m^3)

E_{saline} = Saline efficiency factor (unitless)

However, NPV accounts for three of the variables in Eq. 6 and therefore modified to:

$$G_{CO2} = NPV \, \rho \, E_{saline} \qquad (7)$$

where,

NPV = Net Pore Volume = $A_n \, h_{ntg} \, \Phi_{eff}$ (m^3)

The individual cell net sand thickness (h_{ntg}) and effective porosity (Φ_{eff}) of the HC Sand were derived from the 3D geocellular geologic model with populated reservoir properties

(lithofacies and effective porosity; Figure 4.1). CO_2 density (ρ) was based on Nicholson (2012) and Wallace (2013) with a value of 0.65 ton/m^3 (650 kg/m^3), corresponding to 177 °F (80 °C) and 3625 psi (25 MPa). The capacity calculation assumes that there is no uncertainty in the HC Sand's hydrocarbon footprint area, net sand thickness, and effective porosity.

The saline efficiency factor (Van der Meer, 1995 and Bachu, 2015), E_{saline}, represents the anticipated portion of the effective pore volume accessible for storage.

$$E_{saline} = E_{An/At}\, E_{hn/hg}\, E_{\Phi tot}\, E_v\, E_d \qquad (8)$$

where, $E_{An/At}$ = net-to-total area

$E_{hn/hg}$ = net-to-gross thickness

$E_{\Phi tot}$ = effective-to-total porosity

E_v = volumetric displacement efficiency

E_d = microscopic displacement efficiency.

However, since the net-to-total area (hydrocarbon footprint), net-to-gross sand thickness (3D facies model), and effective-to-total porosity (3D effective porosity model) are derived directly from the geocellular grid, the equation condenses to:

$$E_{saline} = E_v\, E_d \qquad (9)$$

The total efficiency factor for clastic reservoirs (Table 4.3) was taken directly from Goodman et al. (2011) to estimate the P10 (E_{saline} = 7.4%), P50 (E_{saline} = 14%), and P90 (E_{saline} = 24%) CO_2 storage capacity estimates for the HC Sand utilizing all 10 realizations of the effective porosity model. Estimates of the storage capacity in the HC Sand ranged from 6 to 19 Mt of CO_2, with a P50 value of 11 Mt. The primary reason that a 13 Mt range was calculated was because of the different efficiency factors applied to the NPV estimates. It was important to recognize how impactful the E_{saline} values were on the storage capacity estimates because the difference between 11 Mt and 19 Mt can be significant. A 19 Mt

estimate is a more reasonable estimate to consider a CO_2 storage project, but the results show there is only a 10% chance of the HC Sand actually having that storage capacity utilizing the 3D geocellular models methodology.

	P10	P50	P90
$E_{saline} = E_v E_d$	7.4%	14%	24%
HC Sand: 3D Constant Avg. Eff. Porosity Model (Mt)	6	11	19

Table 4.3: HC Sand CO_2 storage capacity estimate using 10 realizations of a 3D effective porosity model.

CO_2 SCREEN Methodology

CO_2-SCREEN (CO_2 Storage Prospective Resource Estimation Excel Analysis) is an Excel™ based tool and workflow that was developed by the US-DOE-NETL to screen geological formations for CO_2 storage. It comprises of two files: an Excel™ spreadsheet that is used for the inputs and outputs and a GoldSim Player for the Monte Carlo simulations. The CO_2-SCREEN manual (Sanguinito et al., 2017) and other published literature describe how to utilize this tool (Goodman et al., 2016; Sanguinito et al., 2018).

Unlike the previous DOE methodology employed above, CO_2-SCREEN solves analytic expressions in a horizontal 2D (XY) space. A 2D grid was created that had the same XY parameters as the AOI but with 225 total grid cells (15x15), each grid cell having an area of about 200 acres (0.8 sq. km). This model is much coarser than the prior model by necessity of the CO_2-SCREEN methods. Similar to upscaling properties to the 3D grid, NTG thickness and/or average porosity had to be upscaled to the 2D grid in every grid cell, deriving the properties from the 3D geocellular models. Using only one realization for the 3D facies model, a sandstone thickness map of the HC Sand was generated using an average interpolation algorithm (Figure 4.8). Only 16 of 225 grid cells captured the HC Sand's hydrocarbon footprint. An average porosity map of the reservoir was not needed because a constant value of 0.29 was previously assigned to all the clean sands.

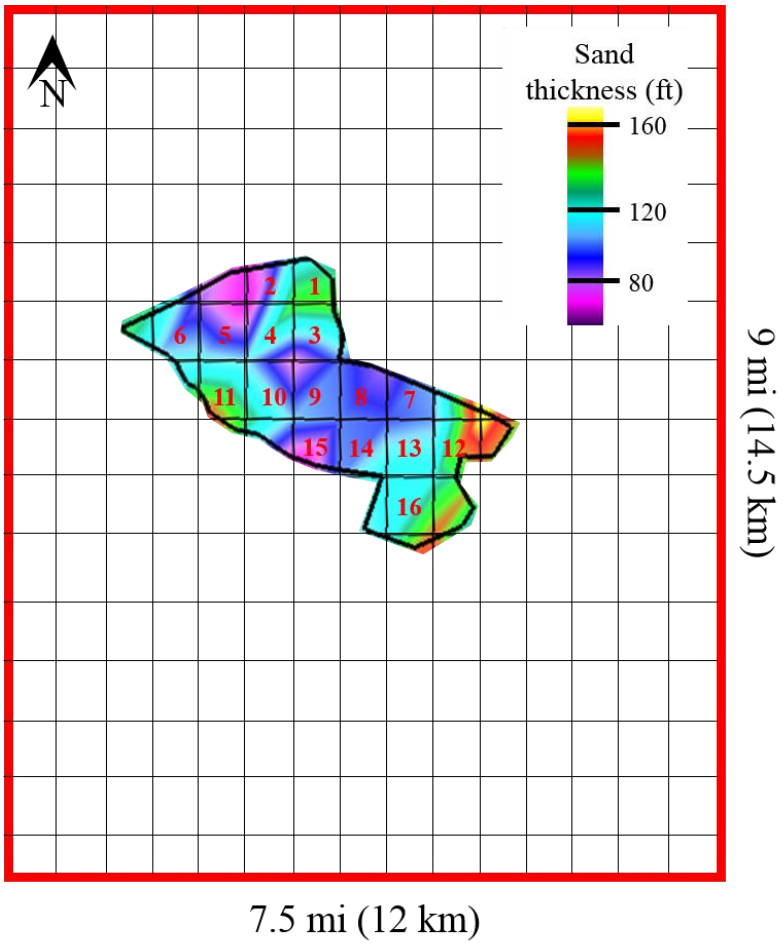

Figure 4.8: Sand thickness map of the HC Sand inside its hydrocarbon footprint (black). AOI is outlined in red.

Using the Excel™ spreadsheet of CO_2 SCREEN (Figure 4.9), the first step is to specify the depositional environment/lithology and the saline efficiency factor. This methodology again assumes that no hydrocarbons accumulated in the HC Sand. A deltaic depositional environment was selected to represent the HC Sand. With the same assumption of no uncertainty in the area, porosity, and thickness, in step two, a value of 1 was given to its respective saline efficiency variable (Figure 4.10). For step 3 in the spreadsheet, the area, NTG sand thickness, and effective porosity were all input parameters with a constant pressure (3625 psi; 25 MPa) and temperature (177 °F; 80 °C) that defined a 0.65 ton/m^3 CO_2 density. After the Monte Carlo simulation, the P10, P50, P90 storage capacity estimates were based on the software's calculated 10%, 21%, and 39% efficiency factor, respectively. The calculated storage capacity estimates were then 8 to 32 Mt, with a P50 value of 18 Mt (Table 4.4). These estimates differ from those in the previous methodology because CO_2-SCREEN allowed assigning a depositional environment to characterize the HC Sand. By defining a deltaic depositional environment, a 7% increase in the efficiency factor increased the storage capacity by 7 Mt.

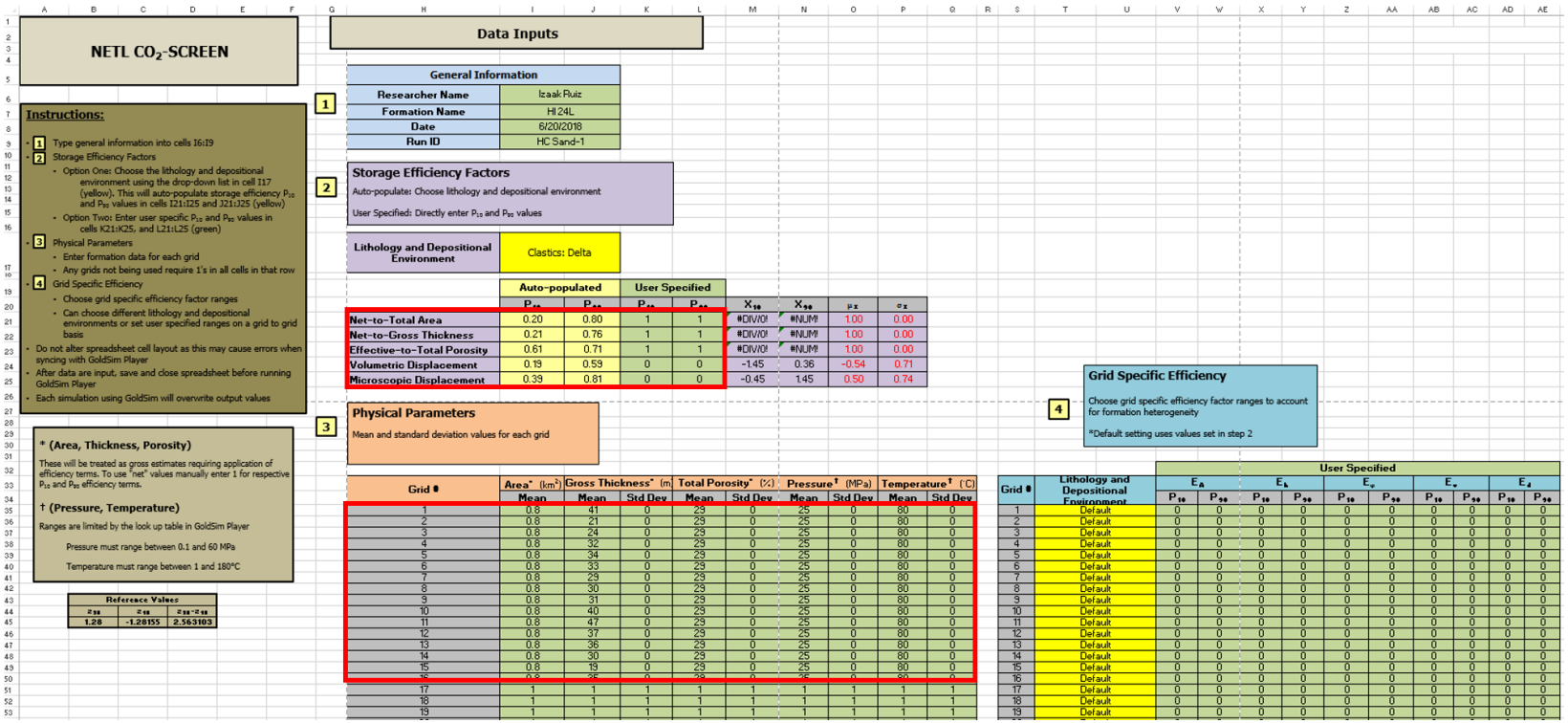

Figure 4.9: CO_2 SCREEN Excel™ spreadsheet layout. The important parameters that need to be defined are outlined in red: saline efficiency factor and physical parameters (area, thickness, porosity, pressure, and temperature).

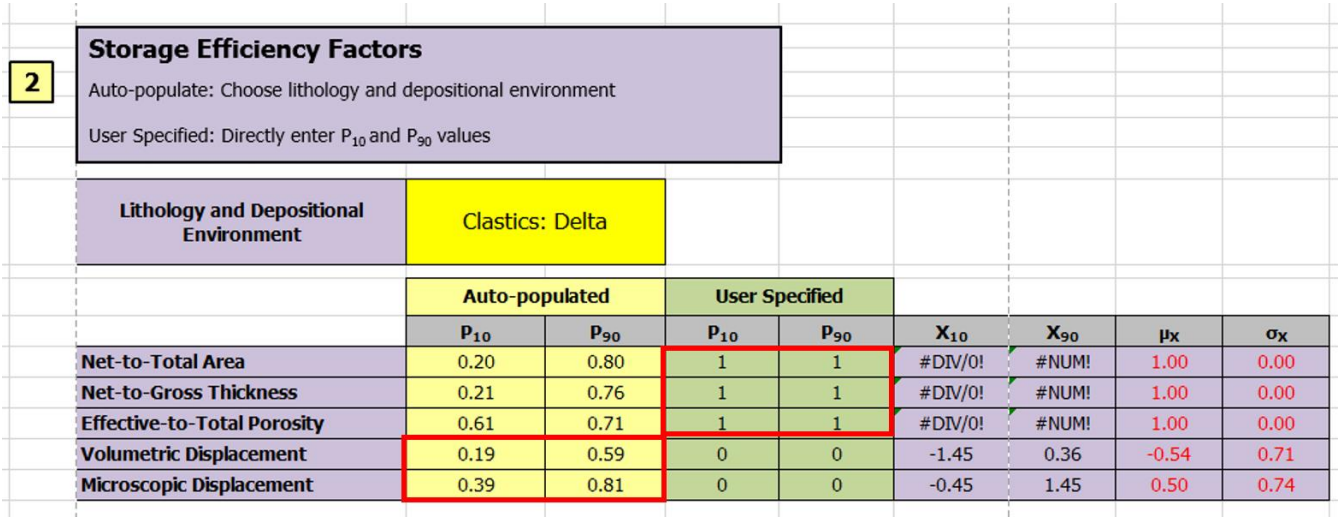

2

Storage Efficiency Factors

Auto-populate: Choose lithology and depositional environment

User Specified: Directly enter P_{10} and P_{90} values

Lithology and Depositional Environment	Clastics: Delta

	Auto-populated		User Specified					
	P_{10}	P_{90}	P_{10}	P_{90}	X_{10}	X_{90}	μ_X	σ_X
Net-to-Total Area	0.20	0.80	1	1	#DIV/0!	#NUM!	1.00	0.00
Net-to-Gross Thickness	0.21	0.76	1	1	#DIV/0!	#NUM!	1.00	0.00
Effective-to-Total Porosity	0.61	0.71	1	1	#DIV/0!	#NUM!	1.00	0.00
Volumetric Displacement	0.19	0.59	0	0	-1.45	0.36	-0.54	0.71
Microscopic Displacement	0.39	0.81	0	0	-0.45	1.45	0.50	0.74

Figure 4.10: Saline efficiency values in CO_2 SCREEN. A value of "1" is given to the first three variables because net area, sand thickness, and effective porosity values are used to characterize the HC Sand, as no uncertainty in them was assumed. The volumetric and microscopic displacement variables are left as is.

	P10	P50	P90
$E_{saline} = E_v E_d$	10%	21%	39%
HC Sand: CO_2 SCREEN (Mt)	8	18	32

Table 4.4: HC Sand CO_2 storage capacity estimate using CO_2 SCREEN. The P10, P50, and P90 values are calculated by applying the appropriate efficiency factor.

Direct Hydrocarbon Production to CO_2 Mass Methodology

An independent way to evaluate these calculated capacity numbers is by comparing them to the known hydrocarbon history at the field. Having historic production data (from the Railroad Commission of Texas) for the offshore TSW fields was essential for this methodology. Different from the two previous methodologies, this method acknowledges the physical presence of the natural gas produced from the HC Sand. About 206 Bcf has been produced from the HC Sand, and the goal was to calculate how much CO_2 this translates to, assuming that CO_2 was the gas that was produced from the HC Sand.

To estimate the CO_2 mass that would be equivalent to the original hydrocarbon volume, first the total gas produced had to be converted to Original Gas in Place (OGIP) using a recovery factor (RF). Next, OGIP was converted to hydrocarbon pore volume (HCPV) using a volumetric gas factor (B_g). Lastly, HCPV was converted to CO_2 mass using an appropriate CO_2 density and efficiency factor value (Figure 4.11).

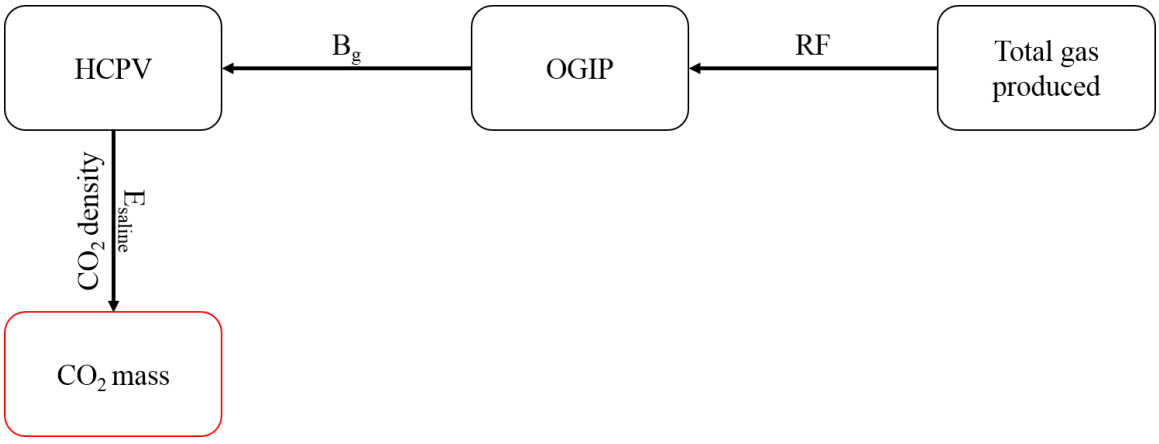

Figure 4.11: Workflow for converting total gas produced to CO_2 mass.

To convert the total gas produced to OGIP, the following equation was used:

$$\text{Recoverable/Produced gas} = \text{OGIP} \times \text{RF} \qquad (10)$$

where,

OGIP = Original Gas in Place (ft^3)

RF = Recovery factor = 95%; (Fowler et al., 1987)

After calculating OGIP, a volumetric factor was calculated using the following equation:

$$\text{OGIP} = \frac{43560\ A\ h\ \Phi\ (1-S_w)}{B_g} \qquad (11)$$

where,

43560 = conversion factor from acre-ft to ft^3

A = area (acre)

h = thickness (ft)

Φ = porosity (unitless)

S_w = water saturation (unitless)

B_g = formation volume factor for gas (ft^3/Standard cubic feet; CF/SCF)

B_g was estimated using the area (1935 acres), thickness (225 ft), porosity (0.3), and water saturation (12%), values from Fowler et al. (1987). The result was 0.027 CF/SCF. OGIP was then converted to HCPV using Eq. 11, but it was modified to exclude the pore volume occupied by formation water. The following equation shows this:

$$\text{OGIP} = \frac{\text{HCPV}}{B_g} \qquad (12)$$

Eq. 7 was then used to convert HCPV (replacing NPV) to CO_2 mass, and the result was 108 Mt before applying any sort of efficiency factor. However, in order to compare across

the two previous methodologies, the six previous efficiency factors were utilized to calculate a range of 8 to 42 Mt. The efficiency factors were applied to the 108 Mt estimate of directly converting natural gas production to CO_2 mass to calculate the P10, P50, and P90 storage capacity estimates (Table 4.5). This methodology yielded higher estimates than both the previous methodologies with respect to the appropriate efficiency factors.

	P10	P50	P90
$E_{saline} = E_v E_d$ (3D Model)	7.4%	14%	24%
HC Sand: Gas Production (Mt)	8	15	26
$E_{saline} = E_v E_d$ (CO_2 SCREEN)	10%	21%	39%
HC Sand: Gas Production (Mt)	11	23	42

Table 4.5: HC Sand CO_2 storage capacity estimate using total gas produced value as a constraint. The first set of efficiency factors was applied to the 3D geocellular models methodology. The second set of efficiency factors was applied to the CO_2 SCREEN methodology.

Summary of HC Sand Static Results

Three static methodologies were utilized to estimate the CO_2 storage capacity of the HC Sand: (1) 3D geocellular models, (2) CO_2-SCREEN, and (3) directly converting natural gas production to CO_2 mass. All the results are summarized in Table 4.6. The first methodology was estimated from the 3D effective porosity models, which was very similar to the second methodology because many of the input parameters were derived from the 3D models. The only difference in these two was the applied efficiency factor as the first methodology used values from Goodman et al. (2011) and the second methodology from the CO_2 SCREEN tool by defining a deltaic depositional environment. The third methodology was confidently utilized by data from the RRC, but the flaw lay with the efficiency factor. This was why the third methodology applied the efficiency factors from the other two methodologies: there was no certainty about an appropriate E_{saline} value. It was noteworthy, however, that if geologic time scales were given for CO_2 to occupy the pore space in the HC Sand, about 108 Mt would have accumulated. For a CCS project, the lifetime is in the tens of years range, not in the millions. Therefore, a key part of the results was recommending that a proper efficiency factor analysis should be researched to predict the HC Sand's storage potential better. For now, the most representative storage capacity estimate is between 15 and 23 Mt because the third methodology has more reliability in the workflow as the two other methodologies were utilized to estimate a reasonable efficiency factor.

	P10	P50	P90
(1) $E_{saline} = E_v E_d$	7.4%	14%	24%
(1) HC Sand: 3D Constant Avg. Eff. Porosity Model (Mt)	6	11	19
(3) HC Sand: Gas Production (Mt)	8	15	26
(2) $E_{saline} = E_v E_d$	10%	21%	39%
(2) HC Sand: CO_2 SCREEN (Mt)	8	18	32
(3) HC Sand: Gas Production (Mt)	11	23	42

Table 4.6: Summarized results of all the CO_2 storage capacity estimates for the HC Sand utilizing the three static methodologies: (1) 3D geocellular models, (2) CO_2 SCREEN, and (3) direct conversion of natural gas production to CO_2 mass.

4.4: SIOI CAPACITY ANALYSIS

Given that the HI 24L Field has much more storage potential than the HC Sand, it is valuable to consider other opportunities for developing a commercial CCS project at the site. Considering that the calculated CO_2 storage capacity of the HC Sand is around 15 to 23 Mt, a similar process can be undertaken to consider the capacity of the overlying 1720 ft (525 m) sand-prone strata in the SIOI. One distinction is that no hydrocarbons were produced from the SIOI, and the implications of this for CCS are discussed further at the end of this chapter. Therefore, the direct hydrocarbon production to CO_2 mass conversion methodology was not performed for the SIOI.

3D Geocellular Models Methodology

The same workflow that applied to the HC Sand was repeated for the SIOI and its respective structural closure footprint (Figure 4.3). However, the upscaled non-linear porosity volume derived from 3D seismic data (performed by other GCCC researchers and available to the project) was used as secondary data to calculate the variogram for effective porosity instead of assigning a constant EPHI value to each lithofacies. Chapter 3 illustrates this 3D modeling workflow for the model portion cropped to the structural footprint.

Equations 7 and 9 were the basis for this static storage capacity calculation after going through the entire workflow of creating a 3D grid, facies model, and effective porosity model, seen in Figure 4.12. A fault offset similar to that seen in the HC Sand model can be seen in the lower part of the 3D model, and the offset decreases to about 150 ft (45 m) near the top of the model. Thick sands, inter-layered shales, and good porosity characterize the SIOI. Overall, the 3D grid resembles a much thicker (> 1500 ft; 457 m) section than the HC Sand 3D grid. Using parameters similar to those used with the HC Sand, 50 realizations of the effective porosity model were created to calculate and average

storage capacity for the SIOI. The P50 result (using 14% efficiency factor) was 108 Mt, approximately 10 times more than the HC Sand using the 3D geocellular models methodology (Table 4.7). This seems reasonable because the SIOI is about 10 times thicker than the HC Sand, which should yield a storage capacity result of at least 10 times larger, assuming a single sand for the SIOI.

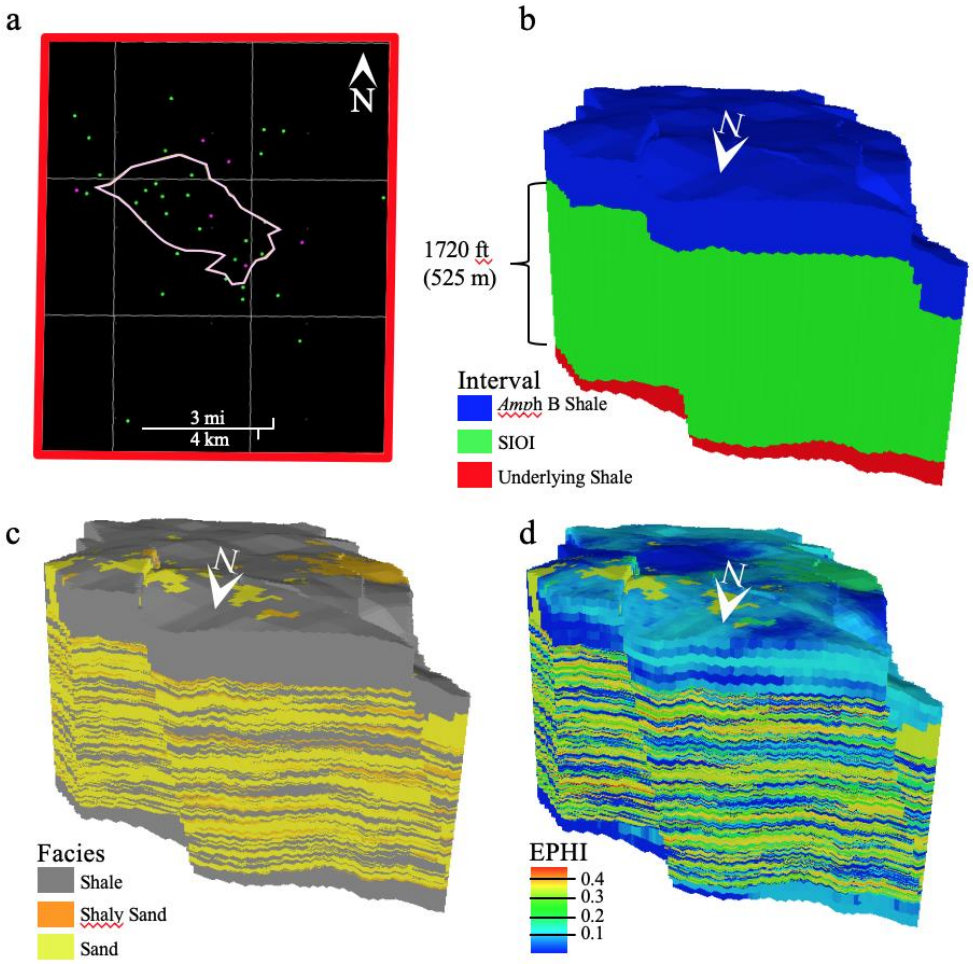

Figure 4.12: SIOI 3D models. (a) Map view of the structural closure footprint (pink) and the AOI (red) with wells (color scheme the same). Parts (b), (c), and (d) illustrate the interval, facies, and effective porosity models from the grid, respectively.

	P10	P50	P90
$E_{saline} = E_v E_d$	7.4%	14%	24%
SIOI: 3-D Eff. Porosity Model (Mt)	57	108	186

Table 4.7: SIOI CO_2 storage capacity estimate using 3D effective porosity model.

CO_2 SCREEN Methodology

The SIOI was also evaluated using the CO_2-SCREEN methodology. This calculation used the same 2D grid footprint as for the HC Sand because the AOI stays the same. A total of 16 grid cells characterized the outline of the structural closure footprint. Since the effective porosities were not kept constant as in the HC Sand's effective porosity model, an average porosity map of all the clean sands in the SIOI was created (Figure 4.13). The sand thickness was 10 times larger than the HC Sand, and the EPHI values from the effective porosity models were slightly higher.

A P50 value of 109 Mt was calculated for the SIOI using CO_2 SCREEN (Table 4.8). However, unlike the HC Sand, four depositional environments (Table 4.9) can all characterize the SIOI and yield different storage capacity results. The interpretation of the SIOI in this study relates more to a shelfal environment. Therefore, the P50 value for a shelf environment (E_{saline} = 23%) was about 179 Mt, 70 Mt larger when using a 14% saline efficiency factor. In both cases for the HC Sand and the SIOI, it is now shown that the depositional environment significantly increases the storage capacity estimate.

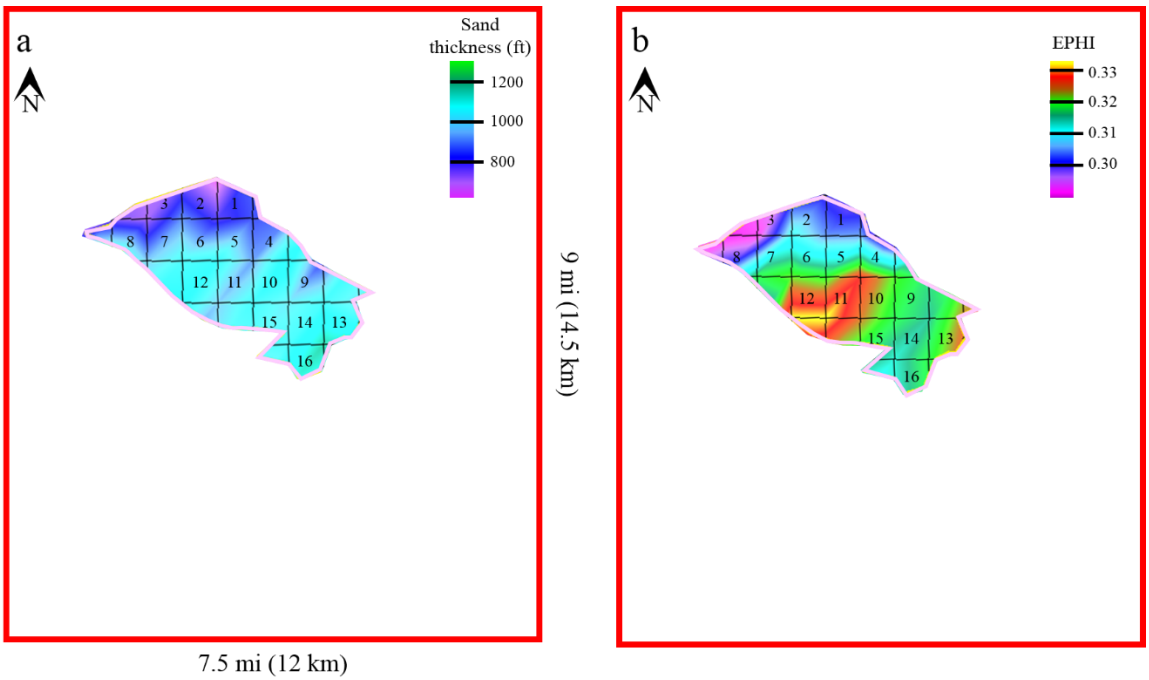

Figure 4.13: (a) Sand thickness and (b) average porosity map of the SIOI inside its structural closure footprint (pink). AOI is outlined in red. The 15 x 15 grid can be seen in Figure 4.8.

	P10	P50	P90
$E_{saline} = E_v E_d$	7.4%	14%	24%
SIOI: CO_2 SCREEN (Mt)	57	109	187

Table 4.8: SIOI CO_2 storage capacity estimate using CO_2 SCREEN.

CO_2 SCREEN Depositional Environment	$E_{saline} = E_v E_d$			CO_2 Mass (Mt)		
	P10	P50	P90	P10	P50	P90
Clastics	7%	14%	24%	57	109	187
Delta	10%	21%	39%	77	167	302
Shelf	**11%**	**23%**	**41%**	**85**	**179**	**317**
Shallow Shelf	10%	22%	42%	74	173	325

Table 4.9: SIOI CO_2 SCEEN saline efficiency factors and storage capacity estimates based on different depositional environments. The red bolded row was the preferred interpretation

Summary of SIOI Static Results

Only two of three methodologies utilized for the HC Sand were applied to the SIOI because no hydrocarbons were produced in the SIOI. The geologic properties seem to be similar to, if not better than those of the HC Sand, but why there was no hydrocarbon production in the SIOI is mainly related to the faults. The SIOI is very sandy and too much sand-on-sand contact might increase the risk for a poor lateral seal. Nonetheless, the results from the two methodologies are summarized in Table 4.10. The differences between both methodologies are the same as in the previous section in regard to the HC Sand. A defined depositional environment considerably increased the storage potential for the SIOI. If the SIOI were one single reservoir, which was an assumption made throughout this study, then 179 Mt would be the most reasonable storage capacity estimate.

	P10	P50	P90
(1) $E_{saline} = E_v E_d$	7.4%	14%	24%
(1) SIOI: 3D Eff. Porosity Model (Mt)	57	108	186
(2) $E_{saline} = E_v E_d$	11%	23%	41%
(2) SIOI: CO_2 SCREEN (Mt)	85	179	317

Table 4.10: Summarized results of the CO_2 storage capacity estimates for the SIOI utilizing two static methodologies: (1) 3D geocellular models and (2) CO_2 SCREEN.

4.5: DYNAMIC EASITOOL METHODOLOGY

For perspective, the Sleipner project in the North Sea injects about 2,800 tons of CO_2/day (tCO_2/day), or about 1 Mt per year, into the Utsira Sand that is about 650-820 ft thick (200-250 m) and has 25-30% porosity. About 20-25 Mt was determined to be injected throughout the 25-year project life (Folger, 2013; Chadwick et al., 2000). The SIOI compares reasonably to the Utsira Sand in terms of thickness and porosity.

Another method for calculating the CO_2 storage capacity uses dynamic approaches that solve analytical equations incorporating injection rates and reservoir pressures. An Enhanced Analytical Simulation Tool (EASiTool; Ganjdanesh and Hosseini, 2017)) uses analytical models to predict the impact of CO_2 injection pressures and estimate storage capacity of saline aquifers. This methodology assumes homogeneous reservoir properties, constant rate injection, no specific geologic structure, brine and CO_2 two-phase flow, and fluid properties that are pressure dependent. The goal of this study was to not inform the reader of how each input variable was calculated within EASiTool, as more can be read in Ganjdanesh and Hosseini (2017) and Hosseini et al. (2018), but rather to provide some initial CO_2 storage estimates considering dynamic methods, as opposed to the purely static volumetric methods employed above. The main advantage of utilizing EASiTool is to better understand how dynamic conditions may further constrain a more realistic storage capacity estimate for the SIOI and HC Sand.

The user manual for the EASiTool software provides default average values for the different parameters to run the simulation. (Hosseini, n.d.). Table 4.11 lists all the variables that were used within EASiTool. Only the parameters highlighted in light blue were updated to represent the HI 24L Field as a 25-year CCS project to create a sensitivity analysis. Reservoir pressure, temperature, thickness, porosity, and permeability were defined an average value and also a range of values based on the prior characterization and

modeling results. The lithostatic pressure was assumed to be 1 psi/ft. For the nominal fracture pressure (point at which rocks break; undesirable), it was assumed to be 80% of the lithostatic pressure, translating to 0.8 psi/ft (Stuart, 1970; Du Rochet, 1981). Therefore, the nominal frac pressure was 5200 psi (36 MPa) for the SIOI and 6800 psi (47 MPa) for the HC Sand, representing the maximum injection pressure.

1. Reservoir Parameters	**SIOI**	**HC Sand**
Pressure (MPa)	17-22 (20)	24-26 (25)
Temperature (°C)	60-71 (65)	77-83 (80)
Thickness (m)	311-337 (320)	45-75 (60)
Salinity (mol/Kg)	1-3 (2)	1-3 (2)
Porosity (.)	0.25-0.36 (0.32)	0.25-0.32 (0.29)
Permeability (mD)	100-1000 (483)	100-1000 (483)
Rock Compressibility (1/Pa)	4e-10-6e-10 (5e-10)	4e-10-6e-10 (5e-10)
Max Injection Pressure (MPa)	21-36 (30)	30-47 (40)
Reservoir Area (km^2)	13	13
Basin Area (km^2)	175	175
Boundary Condition	Closed	Closed
2. Relative Permeability (Brooks-Corey)		
Residual Water Saturation	0.4-0.6 (0.5)	0.4-0.6 (0.5)
Residual Gas Saturation	0.08-0.12 (0.1)	0.08-0.12 (0.1)
m	2-4 (3)	2-4 (3)
n	2-4 (3)	2-4 (3)
Kra0	0.95-1 (1)	0.95-1 (1)
Krg0	0.25-0.35 (0.3)	0.25-0.35 (0.3)
3. Simulation Parameters		
Simulation Time (year)	25	25
Injection Well Radius (m)	0.1	0.1
Max Number of Injectors	1-64	1-64

Table 4.11: EASiTool parameters. The highlighted cells in light blue represent the input values from the prior characterization of the HI 24L Field and various assumptions. The numbers in parentheses are the averaged values.

Figure 4.14 shows the four tornado charts derived from performing a sensitivity analysis for two scenarios for the SIOI and the HC Sand. The first scenario assumed that the faults in the footprint area completely sealed fluid migration because the pressure buildup would only occur within the footprint area. If so, about 9 Mt and 2 Mt were the storage capacity estimates with a range of 0-14 Mt and 0-3.5 Mt for the SIOI and the HC Sand, respectively (Figure 4.14a and 4.14c). For the second scenario, the assumption was that the faults were not completely sealing, and as a result pressures across the faults would essentially communicate and dissipate to a larger, defined area (AOI). About 116 Mt and 30 Mt were the estimated storage capacities with a range of 0-200 Mt and 10-45 Mt for the SIOI and HC Sand, respectively (Figure 4.14b and 4.14d). The results from both packages show that the injection pressure was the dominant factor on storage capacity. This study recommends a proper fault seal analysis to better understand the pressure constraints within the HI 24L Field because this dynamic methodology demonstrates a significant increase (13-15 times) in storage capacity if the faults are not completely sealing. Nevertheless, the storage capacity results from the static methodologies fall within the range of the second scenario.

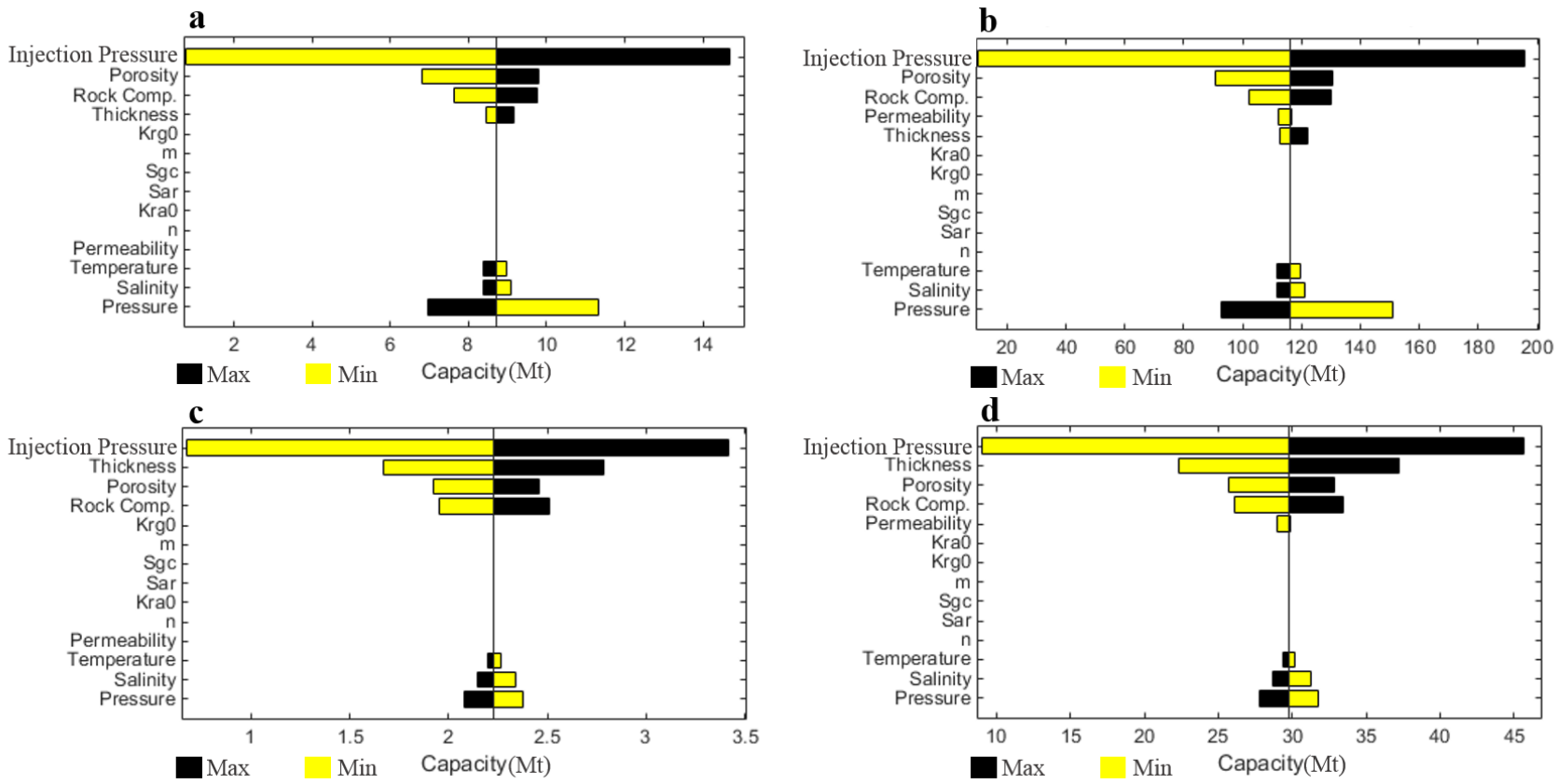

Figure 4.14: Tornado charts showing the sensitivity analysis and CO_2 storage capacity results from the EASiTool methodology. (a) and (c) Faults are assumed to be sealing for the SIOI and HC Sand, respectively. (b) and (d) Direct pressure communication across faults was assumed for the SIOI and HC Sand, respectively. There is a significant capacity difference between both scenarios; injection pressure seems to be the most critical factor.

4.6: DISCUSSION

The 3D static grid and CO_2 SCREEN storage capacity methodologies utilize both seismic and well logs to set the parameters for producing a storage capacity estimate. Although the CO_2 SCREEN workflow might be a coarser evaluation and does not consider 15% of the shaly sands (only clean sands), the results derived from the 3D grid yielded significantly higher storage capacity estimates compared to the 3D models methodology because a depositional environment was identified. An approximately 70 Mt increase was seen within the SIOI; 179 Mt statically represented the storage capacity within the SIOI for the HI 24L Field. The HC Sand also showed an increase in capacity (7 Mt), just not as substantial because the reservoir was less thick. Both the 3D models and CO_2 SCREEN were utilized to understand the efficiency factor because the static estimates did not consider any time and pressure constraints. Therefore, a better methodology to estimate the storage capacity for the HC Sand was incorporating production data.

The first and main assumption made throughout this project was that even though the HI 24L Field was known for its hydrocarbon production, the field was treated as if no hydrocarbons were present, representing a saline aquifer similar to many other nonproductive settings. However, one advantage of evaluating a productive field is that the hydrocarbon produced could be used as a constraint for the CO_2 that could potentially be injected. The assumed lack of hydrocarbons was critical when calculating the storage capacity for the HC Sand, but less so for the SIOI. However, Goodman et al. (2011) defined two ways to estimate the storage capacity for an oil and gas field, differently from for a saline aquifer. The first method is a volumetric-based CO_2 storage resource estimate based on the following equation:

$$G_{CO2}=A\ h_n\ \Phi_{eff}\ (1-S_{wi})\ B\ \rho\ E_{oil/gas} \qquad (13)$$

where;

A = Area (m^2)

h_n = Net oil and gas column height (m)

Φ_{eff} = Average effective porosity (unitless)

S_{wi} = Average initial water saturation (unitless)

B = Fluid formation volume factor (unitless)

ρ = CO_2 density (kg/m^3)

$E_{oil/gas}$ = CO_2 storage efficiency factor; the volume of CO_2 stored in a hydrocarbon reservoir per unit volume of OGIP

Many of these variables are similar to Eq. 6 (for saline formations), but they incorporate elements representative of an oil and gas reservoir like the HC Sand. The second method from Goodman et al. (2011) included the production values because production reflects the reservoir characteristics. However, the formation volume factor (B) still had to be applied, aligning with Eq. 12.

A 1:1 volumetric comparison yielded approximately 108 Mt before applying any efficiency factor. This meant that if millions of years were given for CO_2 to accumulate in the HC Sand at the HI 24L Field and that saturations equivalent to the natural methane accumulation were achieved, 108 Mt of CO_2 could be stored in the reservoir. The direct conversion of produced gas to CO_2 mass overall illustrated the minimum amount of CO_2 that can be injected because it only considers the HCPV and the trap/structural closure footprint has potential to be larger than the hydrocarbon footprint. By applying the efficiency factors from the 3D models and CO_2 SCREEN methodologies, a range of 15 to 23 Mt was estimated for the HC Sand. This range of values statically represented the storage capacity within the HC Sand in the HI 24L Field.

The only dynamic methodology to compare with the static estimates was the EASiTool workflow. Four sensitivity analyses were conducted, and the results demonstrated that injection pressure is the main determining factor for properly estimating CO_2 storage capacity. Two scenarios were built that related to the structure of the HI 24 Field; more specifically, the sealing capacity of the faults. A significant difference in both scenarios was noted. The capacity estimations that were interpreted to represent both the SIOI and HC Sand more accurately using this dynamic workflow were based a scenario in which the faults are assumed to not be sealing completely. About a 200 Mt and 35 Mt range was calculated for the SIOI and HC Sand based on the minimum and maximum injection pressures, with the static storage capacity estimates falling

in between. Therefore, this methodology showed how important it is that the pressure constraints be understood for estimating storage capacity properly.

Based on the four methodologies mentioned above to estimate the CO_2 storage capacity for the SIOI and HC Sand, the results are summarized in Figure 4.15. Researching a smaller reservoir generated more similar results than for a thicker zone. Uncertainty within the SIOI is first attributed to the geologic characterization of the interval. The collection of sands in the SIOI is assumed to be one single reservoir, and the structural footprint is similar to the HC Sand's hydrocarbon footprint. Therefore, this study recommends that the SIOI should be researched in more depth to better constrain the total storage capacity of the HI 24L Field. On the other hand, the HC Sand was confidently characterized and modeled to estimate storage capacity. Results show more potential for CO_2 storage than the prior hydrocarbon pore volume because the fill-t0-spill point may not have been met. Although these results were applied an efficiency factor, a direct conversion from natural gas production to CO_2 mass yielded a 108 Mt estimate, a significant value. It may not be achieved through a CCS project, but if 1 Mt were to be injected each year for 15 years, this project will attain the minimum 14% efficiency factor value of 15 Mt.

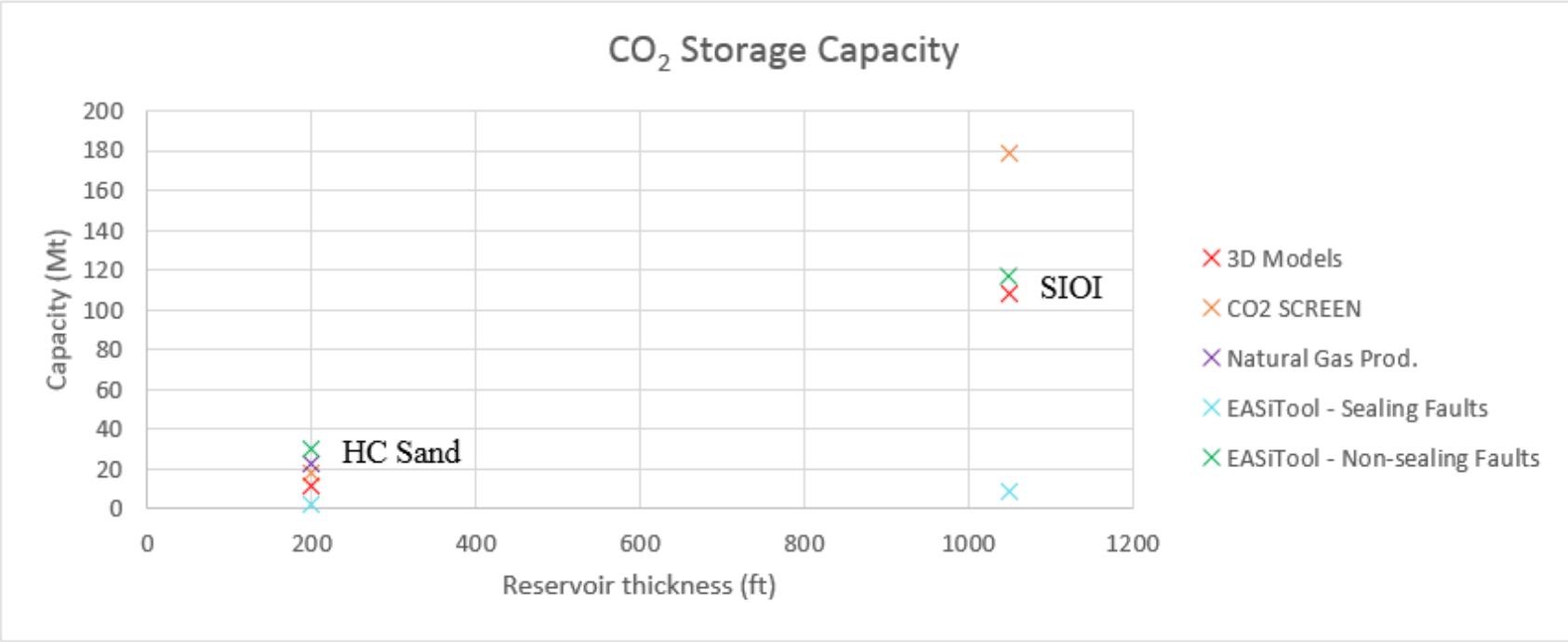

Figure 4.15: Summary of the CO_2 storage capacity results based on the four different methodologies. The 200 ft reservoir represents the HC Sand; ~1050 ft the SIOI. There is more uncertainty within the SIOI than the HC Sand.

Chapter 5: Conclusions and Future Work

5.1: Conclusions

The prior hydrocarbon accumulation at the HI 24L field is considered attractive for demonstrating retention. The HC Sand is one of the most natural gas producing reservoirs in the offshore Texas State Waters, which means that it has good geologic properties for fluids to accumulate over millions of years. Additionally, the field has an overlying section, the SIOI, which is about 10 times thicker than the HC Sand. It shows favorable porosity and sand thickness, but the fact that it does not have any productive hydrocarbons raises a concern regarding seal performance. The geologic and structural characterization of the HI 24L Field (Chapter 2) was important for recognizing the geologic properties that indicate whether the field could be a good storage site. Maximum flooding surfaces that were mapped regionally became the main stratigraphic framework for the geologic analysis, an important step for understanding CCS opportunities in a sequence stratigraphic context (Wang et al., 2019). The purpose of characterizing the HI 24L Field was to demonstrate different methodologies for estimating CO_2 storage capacity for the thick SIOI and the thinner underlying HC Sand.

The workflow first began with characterizing a hydrocarbon field using seismic data and well logs. With such interpretation, the stratigraphic framework was generated and became the foundation for the 3D geocellular grids. Facies and effective porosity were distributed across the 3D grid to create the 3D property models. These models can be utilized to analyze the HI 24L Field further, such as a geomechanic or multi-phase compositional fluid flow simulation, typically considered the most comprehensive way to evaluate dynamic storage capacity. Being able to take these models further for other areas of research was one of the most advantageous parts of this project to try to de-risk any areas

of concern. The next step was to estimate CO_2 storage capacity utilizing different methodologies. This entire workflow was defined in this study in great detail for future field assessments in the offshore Texas State Waters. Future field studies could constrain some of the uncertainties, such as the efficiency factor, injection pressures, and finer geologic characterization.

Characterization of two different stratigraphic intervals showed that Lower Miocene sandstones have very favorable geologic properties for CO_2 storage in the HI 24L Field. The HC Sand was confidently characterized with the help of previous literature and hydrocarbon production data. The hydrocarbon footprint was interpreted for the HC Sand, which represented the assumed area that could only potentially store CO_2. This hydrocarbon footprint was then utilized to interpret the structural footprint for the SIOI. These footprint areas defined an overall area within the AOI that accurately represented the geologic properties (porosity, thickness, top seal, and extent) that were suitable for CO_2 storage.

A CO_2 capacity estimate of 108 Mt was determined by directly converting the recoverable gas in the HC Sand to potentially stored CO_2 mass. A more accurate efficiency factor still needs to be applied to resemble a CCS project; this study only utilized the efficiency factors from the 3D models and CO_2 SCREEN methodologies. The final static capacity estimate for the HC Sand was 15 to 23 Mt. In the SIOI, static results were not as confident as for the HC Sand. By identifying a shelfal depositional environment within CO_2 SCREEN, a 179 Mt estimate was calculated for the SIOI. For both the SIOI and HC Sand, EASiTool showed that the most critical factor in dynamically estimating storage capacity was injection pressure. Also, EASiTool demonstrated how a better analysis of the sealing potential of the faults (boundary condition) can have a significant impact on the

capacity. The average capacity, however, was 116 Mt and 30 Mt for the SIOI and HC Sand, respectively, within a large range.

The goals of the study were reached, but this was just a preliminary step in considering the HI 24L Field as a potential CCS prospect. A 15 to 23 Mt capacity estimate was calculated for the HC Sand using the four defined methodologies as it was confidently characterized and studied. For the SIOI, a wider range of capacity was calculated (108–179 Mt) using only 3 of the 4 methodologies because it had no productive hydrocarbons. Both of these estimates disregard the EASiTool capacity estimate that assumed that the faults were completely sealing because the values are less than 10 Mt and the geologic properties do not represent such low storage potential. However, it shows a proper fault seal analysis can have a substantial impact on the capacity estimates. In the end, both the SIOI and HC Sand show great CO_2 storage potential, as this study illustrates.

5.2: FUTURE WORK

A proper study that estimates a more accurate efficiency factor is necessary. Many of these values were derived solely from Goodman et al. (2011) and the CO_2 SCREEN tool. No fluid flow simulations were performed here to calculate the efficiency factor for the HI 24L Field accurately. This study assumed that this field had no produced hydrocarbons; the next step is to assess and quantify the uncertainties with characterizing this field as an oil and gas field. The efficiency factor that needs to be applied should represent how much CO_2 can be injected based on decadal time scales, pressure constraints, reservoir heterogeneity, number of injection wells (proxy for costs), well spacing, immovable hydrocarbons, vertical leakage (associated with the wells), and other technical challenges. With more confidence in applying an efficiency factor to a nearly depleted hydrocarbon field such as HI 24L, a conversion of gas produced to CO_2 mass can be

accomplished across the hydrocarbon fields in the offshore TSW (similar to Figure 5.1; e.g., 208 Bcf of natural gas converts to 108 Mt before any efficiency factor is applied). In this case, an appropriate efficiency factor has to be applied in order to bring the 108 Mt down to a more realistic value that accounts for operational inefficiencies in accessing the total pore volume. A storage capacity estimate that is derived statically can move on to the next appropriate steps (such as utilizing dynamic methodologies and model simulations) to decide if the field can be used in a CCS project.

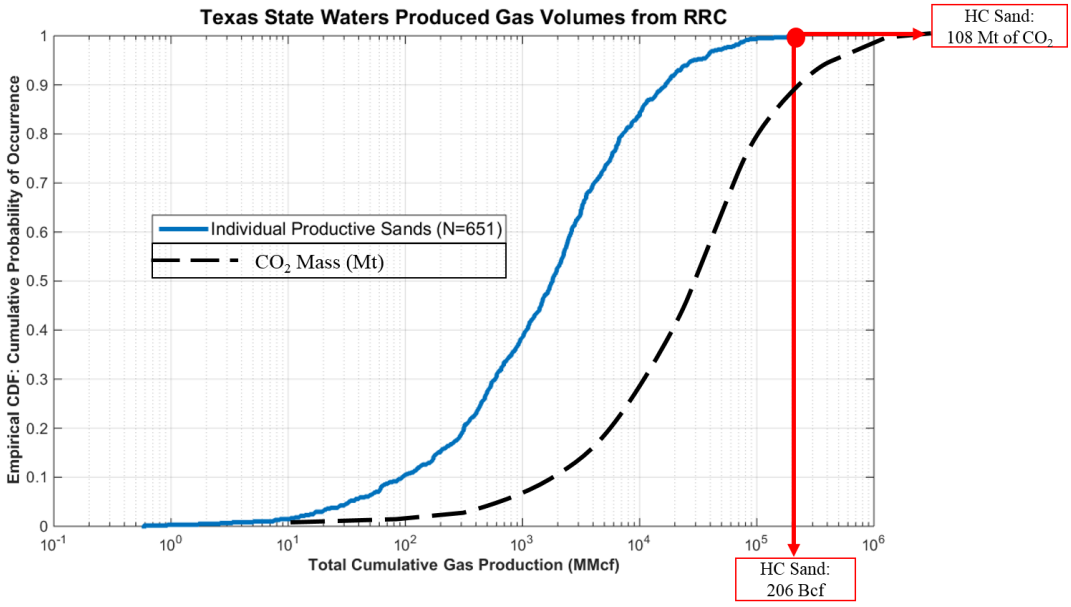

Figure 5.1: Future work: Converting natural gas production for all productive sands in the offshore TSW to CO_2 mass.

This study utilized only spontaneous potential curves to differentiate lithology because only SP log curves existed when the field was discovered in the late 1960's. As oil and gas companies re-drill and reassess the HI 24L Field, gamma ray tests have been conducted to test the radioactivity of the formations. Gamma ray (GR) curves are more accurate in determining the shale volume because shale is composed of radioactive elements such as uranium, potassium, and thorium. Using GR curves to identify the different lithofacies within the HI 24L Field is one suggestion for future work. This can also enable a better understanding of the depositional environment because different stacking patterns can be seen more clearly with GR log curves, leading to another recommendation of performing a more concise geomorphologic analysis (similar to Galloway et al., 2000) for the TexLa 3D survey. Seismic attributes and other software packages can help with this because the goal is to determine in which depositional setting the sands were deposited, mainly for the SIOI. The main advantage of defining the depositional system geometries is to understand the fluid connectivity in the formation, allowing displacement and higher capacity as seen with the CO_2 SCREEN results. More limitations also have to be set to resolve a more accurate value of CO_2 storage capacity of the SIOI because every clean sand in the structural footprint area was assumed to be capable of storing CO_2. A more detailed geologic interpretation of continuous sands with their respective structural spill point in the SIOI can benefit this analysis.

The main area of concern for the SIOI was mainly about the lateral seal. A fault juxtaposition analysis is recommended to determine if the SIOI is actually capable of storing fluids. It is more than performing an analysis of the shale gouge ratio within the fault. A regional analysis of sand/shale juxtaposition vs. fault offset or total hydrocarbon originally trapped in place can help better explain why the SIOI may not have accumulated any fluids because lateral seals are an important component for storage reservoirs. The

SIOI was non-productive and the main reason this might have occurred was because too much sand-on-sand was juxtaposed across faults (Alexander and Handschy, 1998). Unlike the HC Sand, the SIOI is a thick 1720-ft (525-m) section with fault offsets of less than 500 ft (152 m). Therefore, it was highly unlikely for fluids to accumulate with no presence of a lateral seal. On the other hand, the HC Sand does show evidence of a good lateral seal as the reservoir is juxtaposed against shale across faults. Nevertheless, this hypothesis could be tested further; a motivation for doing so is the preliminary storage capacity estimates from this study.

References

Alexander, L. L., & Handschy, J. W. (1998). Fluid flow in a faulted reservoir system: fault trap analysis for the Block 330 field in Eugene Island, south addition, offshore Louisiana. AAPG Bulletin, 82 (3), 387-411.

Asquith, G. B., Krygowski, D., & Gibson, C. R. (2004).Basic Well Log Analysis (Vol. 16). Tulsa: American Association of Petroleum Geologists.

Bachu, S. (2000). Sequestration of CO_2 in geological media: criteria and approach for site selection in response to climate change. Energy Conversion and Management, 41(9), 953-970.

Bachu, S. (2003). Screening and ranking of sedimentary basins for sequestration of CO_2 in geological media in response to climate change. Environmental Geology, 44(3), 277-289.

Bachu, S. (2015). Review of CO2 storage efficiency in deep saline aquifers. International Journal of Greenhouse Gas Control, 40, 188-202.

Bahorich, M. S., & Farmer, S. L. (1995). 3-D seismic coherency for faults and stratigraphic features. The Leading Edge, 1053t, 1058.

Beckham, E. C. (2018). CO_2 storage in deltaic environments of deposition: integration of 3-dimensional modeling, outcrop analysis, and subsurface application: The University of Texas at Austin, Master's thesis.

Benson, S. M., & Cole, D. R. (2008). CO_2 sequestration in deep sedimentary formations. Elements, 4(5), 325-331.

Bohling, G. (2005). Introduction to geostatistics and variogram analysis. Kansas Geological Survey, 1, 1-20.

Brown, A. R. (2004). Interpretation of Three-Dimensional Seismic Data. Society of Exploration Geophysicists and American Association of Petroleum Geologists.

Bulling, T. P., & Olsen, R. S. (1990). Extending field life in offshore Gulf of Mexico using 3-D seismic survey. American Association of Petroleum Geologists, 380-390.

Carr, D. L., Wallace, K. J., Yang, C., & Nicholson, A. J. (2016). CO_2 Sequestration Capacity Sectors in Miocene Strata of the Offshore Texas State Waters. Gulf Coast Association of Geological Societies.

Chadwick, R. A., Holloway, S., Kirby, G. A., Gregersen, U., & Johannessen, P. N. (2000). The Utsira Sand, Central North Sea–an assessment of its potential for regional CO_2 disposal. In Proceedings of the 5th International Conference on Greenhouse Gas Control Technologies (GHGT-5), Cairns, Australia (pp. 349-354).

CO_2CRC. What is CCS? (http://www.co2crc.com.au/whats-ccs-2/)

CCS Facilities Database (https://www.globalccsinstitute.com/resources/ccs-database-public/).

DeAngelo, M. V., Fifariz, R., Meckel, T., & Treviño, R. H. (2019). A seismic-based CO_2-sequestration regional assessment of the Miocene section, northern Gulf of Mexico, Texas and Louisiana. International Journal of Greenhouse Gas Control, 81, 29-37.

Deussen, A., & Owen, K. D. (1939). Correlation of surface and subsurface formations in two typical sections of the Gulf Coast of Texas. AAPG Bulletin, 23(11), 1603-1634.

Du Rouchet, J. (1981). Stress fields, a key to oil migration. AAPG Bulletin, 65(1), 74-85.

Fisher, W. L. (1964). Sedimentary patterns in Eocene cyclic deposits, northern Gulf Coast region. Kansas Geological Survey Bulletin, 169, 151-170.

Folger, P. (2013). Carbon capture and sequestration (CCS): a primer. Congressional Research Service.

Fowler, J., Houston, J., Mitchell, D., & Slater, J. A. (1987). High Island Block 24-L field, Jefferson County. Typical oil and gas fields of Southeast Texas V, Part II: Houston Geological Society, 291-294.

Galloway, W. E. (1989). Depositional framework and hydrocarbon resources of the early Miocene (Fleming) episode, northwest Gulf Coast Basin. Marine Geology, 90(1-2), 19-29.

Galloway, W. E. (1989a). Genetic stratigraphic sequences in basin analysis I: architecture and genesis of flooding-surface bounded depositional units. AAPG Bulletin, 73(2), 125-142.

Galloway, W. E. (1989b). Genetic stratigraphic sequences in basin analysis II: application to northwest Gulf of Mexico Cenozoic basin. AAPG Bulletin, 73(2), 143-154.

Galloway, W. E., Ganey-Curry, P. E., Li, X., & Buffler, R. T. (2000). Cenozoic depositional history of the Gulf of Mexico basin. AAPG Bulletin, 84(11), 1743-1774.

Galloway, W. E. (2008). Depositional evolution of the Gulf of Mexico sedimentary basin. Sedimentary Basins of the World, 5, 505-549.

Galloway, W. E., Whiteaker, T. L., & Ganey-Curry, P. (2011). History of Cenozoic North American drainage basin evolution, sediment yield, and accumulation in the Gulf of Mexico basin. Geosphere, 7(4), 938-973.

Ganjdanesh, R., & Hosseini, S. A. (2017). Geologic Carbon Storage Capacity Estimation Using Enhanced Analytical Simulation Tool (EASiTool). Energy Procedia, 114, 4690-4696.

Global CCS Institute (2018).The Global Status of CCS

Goodman, A., Hakala, A., Bromhal, G., Deel, D., Rodosta, T., Frailey, S., Small, M., Allen, D., Romanov, V., Fazio, J., Huerta, N., McIntyre, D., Kutchko, B. & Guthrie, G. (2011). US DOE methodology for the development of geologic storage potential

for carbon dioxide at the national and regional scale. International Journal of Greenhouse Gas Control, 5(4), 952-965.

Goodman, A., Sanguinito, S., & Levine, J. S. (2016). Prospective CO_2 saline resource estimation methodology: Refinement of existing US-DOE-NETL methods based on data availability. International Journal of Greenhouse Gas Control, 54, 242-249.

Halliburton Landmark. DecisionSpace, DSG10ep.4.03

Hartmann, D. J. (1999). Predicting reservoir system quality and performance. Exploring for Oil and Gas Traps, 9, 1-154.

Hosseini, Seyyed A., Ganjdanesh, Reza, & Kim, Seunghee (2018). Enhanced Analytical Simulation Tool (EASiTool) for CO2 Storage Capacity Estimation and Uncertainty Quantification. United States.

Hosseini, Seyyed A. (n.d). EASiTool – User Manual – V4.0.

Hunt Jr, J. L., & Burgess, G. (1995). Depositional Styles from Miocene Through Pleistocene in the North-Central Gulf of Mexico: An Historical Reconstruction.

Kiatta, H. W. (1971). The stratigraphy and petroleum potential of the lower Miocene, offshore Galveston and Jefferson Counties. Texas: Gulf Coast Association of Geological Societies Transactions, 21, 257-270.

Larionov, V. V. (1969). Radiometry of boreholes. Nedra, Moscow, 127.

Lawless, P. N., Fillon, R. H., & Lytton III, R. G. (1997). Gulf of Mexico Cenozoic biostratigraphic, lithostratigraphic, and sequence stratigraphic event chronology: GCAGS Transactions, v. 47.

Lewicki, J. L., Birkholzer, J., & Tsang, C. F. (2007). Natural and industrial analogues for leakage of CO_2 from storage reservoirs: identification of features, events, and processes and lessons learned. Environmental Geology, 52(3), 457.

Li, Z., Dong, M., Li, S., & Huang, S. (2006). CO_2 sequestration in depleted oil and gas reservoirs—caprock characterization and storage capacity. Energy Conversion and Management, 47(11-12), 1372-1382.

Marsan, D., & Pratama, R. N. (2015) Well Log Data Interpretation and Petrophysical Analysis. Institut Teknologi Bandung, Halliburton On Job Training Program. Powerpoint slide deck.

Morton, R. A., & Galloway, W. E. (1991). Depositional, tectonic and eustatic controls on hydrocarbon distribution in divergent margin basins: Cenozoic Gulf of Mexico case history. Marine Geology, 102(1-4), 239-263.

Nicholson, A. J., (2012). Empirical analysis of fault seal capacity for CO_2 sequestration, lower Miocene, Texas Gulf Coast: The University of Texas at Austin, Master's thesis.

Olariu, M., DeAngelo, M., Dunlap, D., & Treviño, R.H. (in review). Early Miocene High Island delta system, offshore Texas and Louisiana.

Pyrcz, M. J., & Deutsch, C. V. (2014). Geostatistical Reservoir Modeling. Oxford University Press.

Railroad Commission of Texas (RRC) (2019). Offshore Production January 2019 Reports. (https://www.rrc.state.tx.us/oil-gas/research-and-statistics/production-data/offshore-production/)

Rainwater, E. H. (1964). Regional stratigraphy of the Gulf Coast Miocene.

Ramirez Garcia, O. (2019). Geologic characterization and modeling for quantifying CO_2 storage capacity of the High Island 10-L field in Texas state waters, offshore Gulf of Mexico. The University of Texas at Austin, Master's thesis.

Salvador, A. (1987). Late Triassic-Jurassic paleogeography and origin of Gulf of Mexico basin. AAPG Bulletin, 71(4), 419-451.

Sanguinito, S. M., Goodman, A., & Levine, J. (2017). NETL CO_2 Storage prospeCtive Resource Estimation Excel aNalysis (CO_2-SCREEN) User's Manual (No. NETL-PUB-20299). National Energy Technology Lab (NETL), Pittsburgh, PA, (United States).

Sanguinito, S., Goodman, A. L., & Sams, J. I. (2018). CO_2-SCREEN tool: Application to the Oriskany sandstone to estimate prospective CO_2 storage resource. International Journal of Greenhouse Gas Control, 75, 180-188.

Seismic Exchange Inc. (2018) TexLa Transition Merge Zone 3D.

Seni, S. J., Desselle, B. A., & Standen, A. (1994). Scope and construction of a gas and oil atlas series of the Gulf of Mexico: examples from Texas offshore lower Miocene plays: Gulf Coast Association of Geological Societies Transactions, v. 44.

Seni, S. J., Hentz, T.F., & Kaiser, W.R. (1997). Atlas of northern Gulf of Mexico gas and oil reservoirs. Vol. 1: Miocene and Older Reservoirs: The University of Texas at Austin, Bureau of Economic Geology, 199.

Stuart, C. A. (1970). Geopressures. Shell Oil Company, New Orleans, LA.

The Intergovernmental Panel on Climate Change (2018). Global Warming of 1.5°C.

Treviño, R.H., & Meckel, T.A. (2017). Geological CO_2 Sequestration Atlas of Miocene Strata, Offshore Texas State Waters. The University of Texas at Austin, Bureau of Economic Geology, Report of Investigations No. 283, 80.

Van der Meer, L. G. H. (1995). The CO_2 storage efficiency of aquifers. Energy Conversion and Management, 36(6-9), 513-518.

Wallace, K. J. (2013). Use of 3-dimensional dynamic modeling of CO_2 injection for comparison to regional static capacity assessments of Miocene sandstone reservoirs in the Texas State Waters, Gulf of Mexico: The University of Texas at Austin, Master's thesis.

Wallace, K. J., Meckel, T. A., Carr, D. L., Treviño, R. H., & Yang, C. (2014). Regional CO_2 sequestration capacity assessment for the coastal and offshore Texas Miocene interval. Greenhouse Gases: Science and Technology, 4(1), 53-65.

Wang, J., La Croix, A. D., Gonzalez, S., He, J., & Underschultz, J. (2019). Sequence stratigraphic analysis of the Lower Jurassic Precipice Sandstone and Evergreen Formation in the Surat Basin, Australia: Implications for the architecture of reservoirs and seals for CO_2 storage. Marine and Petroleum Geology, 102, 829-843.